

# Computer-Aided Detection and Diagnosis for prostate cancer based on mono and multiparametric MRI/MRSI: A review

Guillaume Lemaître<sup>a,c,\*</sup>, Robert Martí<sup>c</sup>, Jordi Freixenet<sup>c</sup>, Joan C. Vilanova<sup>d</sup>,  
Paul M. Walker<sup>b</sup>, Fabrice Meriaudeau<sup>a</sup>

<sup>a</sup>LE2I-UMR CNRS 6306, Université de Bourgogne, 12 rue de la Fonderie, 71200 Le Creusot, France

<sup>b</sup>LE2I-UMR CNRS 6306, Université de Bourgogne, Avenue Alain Savary, 21000 Dijon, France

<sup>c</sup>ViCOROB, Universitat de Girona, Campus Montilivi, Edifici P4, 17071 Girona, Spain

<sup>d</sup>Girona Magnetic Resonance Center, 26 Carrer Joan Maragall, 17002 Girona, Spain

---

## Abstract

Prostate cancer is reported to be the second most diagnosed cancer of men all over the world. In the last decades, new imaging techniques based on MRI have been developed improving the diagnosis task of radiologists. In practise, diagnosis can be affected by multiple factors reducing the chance to detect potential lesions. Computer-aided detection and computer-aided diagnosis have been designed to answer to these needs and provide help to radiologists in their daily duties. Research on computer-aided systems specifically focused for prostate cancer is a young technology and part of a dynamic field for the last ten years. This survey aimed to provide an overview of the researches carried out in this lapse of time and more precisely a comprehensive review of all the different stages composing the work-flow of computer-aided system. We also provide a comparison between these studies and potential avenues for future research are also discussed.

*Keywords:* computer-aided detection, computer-aided diagnosis, CAD, magnetic resonance imaging, magnetic resonance spectroscopy imaging, computer vision

---

## 1. Introduction

During the last century, physicists focused on constantly innovating in terms of imaging techniques assisting radiologists to overcome different tasks as cancer detection and diagnosis. However, human diagnosis still suffers from low repeatability,

---

\*Corresponding author.

Email addresses: `guillaume.lemaitre@udg.edu` (Guillaume Lemaître), `marly@eia.udg.edu` (Robert Martí), `jordif@eia.udg.edu` (Jordi Freixenet), `pwalker@u-bourgogne.fr` (Paul M. Walker), `fabrice.meriaudeau@u-bourgogne.fr` (Fabrice Meriaudeau)

5 synonymous with erroneous detection or interpretations of abnormalities throughout  
6 clinical decisions (Giger et al. (2008), Hambrock et al. (2013)). These errors are  
7 driven by two majors causes (Giger et al. (2008)). On the one hand, observer lim-  
8 itations (e.g., constrained human visual perception, fatigue or distraction) are the  
9 principal human issues. On the other hand, the second reason is linked to the clinical  
10 cases themselves, for instance due to unbalanced data (number of healthy cases more  
11 abundant than malignant cases) or overlapping structures resulting from limitations  
12 of imaging techniques.

13 Computer vision has given rise to many promising solutions, but, instead of  
14 focusing on fully automatic computerized systems, researchers have aimed at provid-  
15 ing computer image analysis techniques to aid radiologists in their clinical decisions  
16 (Giger et al. (2008)). In fact, these investigations brought about both concepts of  
17 computer-aided detection (CADe) and computer-aided diagnosis (CADx) grouped  
18 under the acronym CAD. Since those first steps, evidence has shown that CAD sys-  
19 tems enhance the diagnosis performance of radiologists. Chan et al. (1999) reported  
20 a significant 4 % improvement in breast cancer detection, in accordance with later  
21 studies (Dean and Ilvento (2006)). Similar conclusions were drawn in the case of lung  
22 nodule detection (Li et al. (2004)), colon cancer (Petrick et al. (2008)) and prostate  
23 cancer (CaP) as well (Hambrock et al. (2013)). Chan et al. (1999) also hypothesized  
24 that CAD systems will be even more efficient assisting inexperienced radiologists to  
25 senior radiologists. That hypothesis was tested by Hambrock et al. (2013) and was  
26 confirmed in case of CaP detection. In this particular study, inexperienced radiolo-  
27 gists obtained equivalent performance to senior radiologists, both with the help of a  
28 CAD system whereas the accuracy of their diagnosis was significantly poorer without  
29 this assistance.

30 In the late eighties, the first CAD systems were developed to detect anomalies on  
31 chest radiographies and mammograms (Chan et al. (1987), Doi et al. (1990), Giger  
32 et al. (1988)). In the past twenty years, extensive investigations were conducted in  
33 the advancement of CAD systems, migrating from intensive time consuming algo-  
34 rithms performed on reduced number of cases to “fast” processing on a large medical  
35 dataset. These works were focused on diverse organ cancer diagnosis making use of  
36 numerous imaging modalities: micro-calcification detection in breast mammography  
37 (Elter and Horsch (2009), Rangayyan et al. (2007)) and ultrasound (US) imaging  
38 (Cheng et al. (2010)), lung nodules detection based on computer tomography (CT)  
39 (Chan et al. (2008), Suzuki (2012)), colon tumours detection (Suzuki (2012)) and  
40 melanoma detection using dermoscopy imaging (Korotkov and Garcia (2012)). Not-  
41 ing the abundance of diverse CAD systems, these fields achieved a certain maturity  
42 which can be explained by the imaging techniques employed. Indeed, x-rays, US as

well as CT are medical imaging techniques developed all before the 1970s and were subject to intensive research.

In contradiction with the aforementioned statement, CaP detection using CAD is a young technology due to the fact that magnetic resonance imaging (MRI) is the keystone medical imaging technique (Hegde et al. (2013)). Four distinct MRI modalities are employed in CAD for CaP and were mainly developed after the mid-1990s: (i)  $T_2$  Weighted ( $T_2$ -W) MRI (Hricak et al. (1983)), (ii) dynamic contrast-enhanced (DCE) MRI (Huch Boni et al. (1995)), (iii) magnetic resonance spectroscopy imaging (MRSI) (Kurhanewicz et al. (1996)) and (iv) diffusion weighted (DW) MRI (Scheidler et al. (1999b)). It can be noted that these techniques came into existence relatively recently mainly due to technological progress. In addition, the increase of magnetic field strength and the development of endorectal coil, both improved image spatial resolution (Swanson et al. (2001)) needed to perform more accurate diagnosis. It is for this matter that development of CAD for CaP is lagging behind the other fields stated above.

The first study using MRI as inputs of CAD system was published ten years ago by Chan et al. (2003). Despite this, no less than fifty studies have been reviewed for this survey since that seminal work. To the best of our knowledge, there is no review in the literature regarding the advancement of CAD systems devoted specifically to CaP detection and diagnosis. Thus, our aim with this survey is threefold: (i) provide an overview of developed CAD systems for CaP detection and diagnosis based on MRI modalities (ii) assess the different work and (iii) pointing out avenues for future work.

As discussed further in Sect. 2.3.3, CAD systems share a common framework. Stages involved in CAD work-flow can be categorized into six distinctive processes: (i) pre-processing, (ii) segmentation, (iii) registration, (iv) feature detection, (v) feature selection and extraction and (vi) classification. The first three stages are used to enhance data as well as to extract regions of interest and, in the case of multi-modal sources, to merge information of those heterogeneous sources in a joint reference system. The last three categories deal with pattern recognition, machine learning and data mining notions and more precisely with the data classification problem. First, information is detected from the different data sources and a subset of relevant features is selected and/or extracted. Then, this meaningful data will then be classified in order to provide the probability of malignancy of the area of interest and will assist radiologists in their diagnosis decisions (see Fig. 2.3.2).

This paper is organized as follows: Sect. 2 deals with general information about human prostate and background about CaP. Methods regarding CaP screening and imaging techniques used are also presented as well as an introduction on the CAD

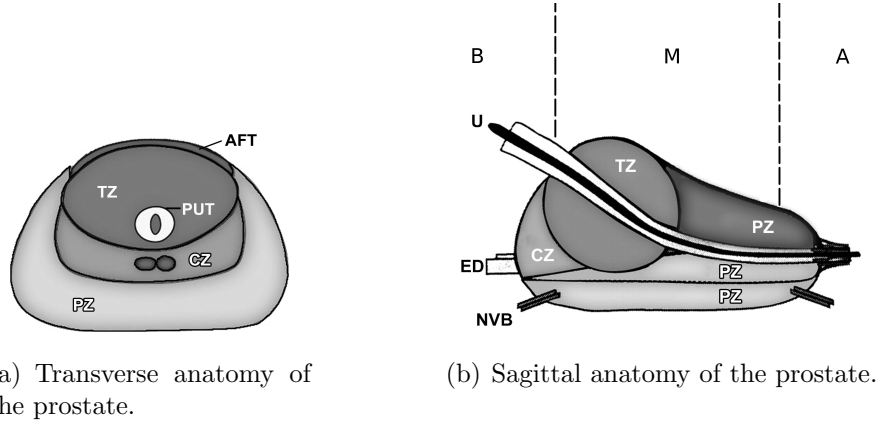


Figure 1: Prostate anatomy with division in different zones. *AFT*: anterior fibromuscular tissue, *CZ*: central zone, *ED*: ejaculatory duct, *NVB*: neurovascular bundle, *PUT*: tissue, *PZ*: peripheral zone, *U*: urethra, *TZ*: transitional zone, *B*: base, *M*: median, *A*: apex (copyright by Choi et al. (2007)).

framework. Sections 3 - 4 review techniques used in different steps involved in a CAD work-flow which will be our main contribution. Image regularization framework including pre-processing (Sect. 3.1), segmentation (Sect. 3.2) and registration (Sect. 3.3) will be covered as well as the image classification framework comprising of feature detection (Sect.4.2), feature selection and extraction (see Sect. 4.3) and feature classification (Sect. 4.4). Results and discussion are reported in Sect. 5 followed by a concluding section.

## 2. Background

This section provides an overview of CaP and its detection and diagnosis. We start with a summary of the prostate anatomy and a brief overview of different CaPs. Subsequently a discussion of the current screening strategy for CaP and its drawbacks is presented. MRI plays an important role in improving the current strategy and a more detailed description of MRI modalities is given. These different techniques are used as inputs to the CAD system which is finally discussed.

### 2.1. The human prostate

The prostate is an exocrine gland of the male reproductive system having an inverted pyramidal shape. It measures approximately three centimetres in height by two and half centimetres in depth and its weight is estimated to be between seven and sixteen grams for an adult (Leissner and Tisell (1979)). The prostate size

100 increases at two distinct stages during physical development: initially at puberty to  
101 reach its normal size, then again after sixty years of age leading to benign prostatic  
102 hyperplasia (BPH) (Parfait (2010)).

103 A zonal classification of the prostate, depicted in Fig. 1, was suggested by McNeal  
104 (McNeal (1981)). Subsequently, this categorization was widely accepted in the lit-  
105 erature (cf., Coakley and Hricak (2000), Hricak et al. (1987), Parfait (2010), Villers  
106 et al. (1991)) and is used in all medical examinations (e.g., biopsy, MRI screening).  
107 The classification is based on dividing the gland into three distinct regions: (i) central  
108 zone (CZ) accounting for 20-25% of the whole prostate gland, (ii) transitional zone  
109 (TZ) standing for 5% and (iii) peripheral zone (PZ) representing the 70%. In MRI  
110 images, tissues of CZ and TZ are difficult to distinguish and are usually merged into  
111 a common region, denominated central gland (CG). As part of this classification,  
112 the prostate can be divided in three longitudinal portions depicted in Fig. 1(b): (i)  
113 base, (ii) median gland and (iii) apex.

## 114 2.2. Prostate carcinoma

115 CaP has been reported on a worldwide scale to be the second most frequently  
116 diagnosed cancer of men accounting for 13.6% (Ferlay et al. (2010)). Statistically,  
117 in 2008, the number of new diagnosed cases was estimated to be 899,000 with no  
118 less than 258,100 deaths (Ferlay et al. (2010)). In United States, aside from skin  
119 cancer, CaP was declared to be the most commonly diagnosed cancer among men,  
120 implying that approximately one in six men will be diagnosed with CaP during their  
121 lifetime and one in thirty-six will die from this disease causing CaP to be the second  
122 most common cause of cancer death among men (Siegel et al. (2013), American  
123 Cancer Society (2013)).

124 Despite active research to determine the causes of prostate cancer, a fuzzy list of  
125 risk factors has arisen (American Cancer Society (2010)). The etiology was linked to  
126 the following factors (American Cancer Society (2010)): (i) family history (Giovannucci  
127 et al. (2007), Steinberg et al. (1990)), (ii) genetic factors (Agalliu et al. (2009),  
128 Amundadottir et al. (2006), Freedman et al. (2006)), (iii) race-ethnicity (Giovannucci  
129 et al. (2007), Hoffman et al. (2001)), (iv) diet (Alexander et al. (2010), Giovannucci  
130 et al. (2007), Ma and Chapman (2009)), (v) obesity (Giovannucci et al. (2007), Ro-  
131 driguez et al. (2007)). This list of risk factors alone cannot be used to diagnose CaP  
132 and in this way, screening enables early detection and treatment.

133 CaP growth is characterized by two main types of evolution (Strum and Pogliano  
134 (2005)): slow-growing tumours, accounting for up to 85 % of all CaPs (Lu-Yao  
135 et al. (2009)), progress slowly and usually stay confined to the prostate gland. For  
136 such cases, treatment can be substituted with active surveillance. In contrast, the

second variant of CaPs develops rapidly and metastasises from prostate gland to others organs, primarily the bones (Oster et al. (2013)). Bone metastases, being an incurable disease, significantly affects the morbidity and mortality rate (Ye et al. (2007)). Hence, the results of the surveillance have to be trustworthy in order to distinguish aggressive from slow-growing CaP.

CaP is more likely to come into being in specific regions of the prostate. In that respect, around 70-80 % of CaPs originate in PZ whereas 10-20 % in TZ (Carrol et al. (1987), McNeal et al. (1988), Stamey et al. (1998)). Only about 5 % of CaPs occur in CZ (Cohen et al. (2008), McNeal et al. (1988)). However, those cancers appear to be more aggressive and more likely to invade other organs due to their location (Cohen et al. (2008)).

### *2.3. CaP screening and imaging techniques*

#### *2.3.1. Current CaP screening*

Current CaP screening consists of three different stages. First, prostate-specific antigen (PSA) control is performed to distinguish between low and high risk CaP. Then, for confirmation, samples are taken during prostate biopsy and finally analysed to evaluate the prognosis and the stage of CaP. In this section, we present a detailed description of the current screening as well as its drawbacks.

Since its introduction in mid-1980s, PSA is widely used for CaP screening (Etzioni et al. (2002)). A higher-than-normal level of PSA can indicate an abnormality of the prostate either as a BPH or a cancer (Hoeks et al. (2011)). However, other factors can lead to an increased PSA level such as prostate infections, irritations, a recent ejaculation or a recent rectal examination (Parfait (2010)). PSA can be found in the bloodstream in two different forms: free PSA (about 10%), and linked to another protein (about 90%). A level of PSA higher than  $10 \text{ ng.mL}^{-1}$  is considered to be at risk (Parfait (2010)). If the PSA level is between  $10 \text{ ng.mL}^{-1}$  and  $4 \text{ ng.mL}^{-1}$ , the patient is considered as suspicious (Barentsz et al. (2012)). In that case, the ratio of free PSA to total PSA is computed; if the ratio is higher than 15%, the case is considered as pathological (Parfait (2010)).

A transrectal ultrasound (TRUS) biopsy is carried out for cases which are considered as pathological. At least six different samples are taken randomly from the right and left parts of three different zones: apex, median and base. These samples are further evaluated using the Gleason grading system (Gleason (1977)). The scoring scheme to characterize the biopsy sample is composed of five different patterns which correspond to grades ranging from 1 to 5. Higher grades are associated with poor prognosis (Epstein et al. (2005)). Then, in the Gleason system, two scores are assigned corresponding to (i) the grade of the most present tumour

174 pattern, and (ii) the grade of the second most present tumour pattern (Epstein et al.  
175 (2005)). A higher Gleason score (GS) indicates a more aggressive tumour (Epstein  
176 et al. (2005)). Also, it should be noted that biopsy is an invasive procedure which can  
177 result in serious infection or urine retention (Chou et al. (2011), Hara et al. (2005)).

178 Although PSA screening has been shown to improve early detection of CaP (Chou  
179 et al. (2011)), its lack of reliability motivates further investigations using MRI-CAD.  
180 Two reliable studies, carried out in the United States (Andriole et al. (2009)) and  
181 in Europe (Hugosson et al. (2010), Schröder et al. (2012)), have attempted to assess  
182 the impact of early detection of CaP, with diverging outcomes (Chou et al. (2011),  
183 Heidenreich et al. (2013)). The study carried out in Europe<sup>1</sup> concluded that PSA  
184 screening reduces CaP-related mortality by 21-44% (Hugosson et al. (2010), Schröder  
185 et al. (2012)), while the American<sup>2</sup> trial found no such effect (Andriole et al. (2009)).  
186 However, both studies agree that PSA screening suffers from low specificity, with an  
187 estimated rate of 36 % (Schroder et al. (2008)). Both studies also agree that over-  
188 treatment is an issue: decision making regarding treatment is further complicated by  
189 difficulties in evaluating the aggressiveness and progression of CaP (Delpierre et al.  
190 (2013)).

191 Hence, new screening methods should be developed with improved specificity of  
192 detection as well as more accurate risk assessment (aggressiveness and progression).  
193 Current research is focused on identifying new biological markers to replace PSA-  
194 based screening (Bourdounis et al. (2010), Brenner et al. (2013), Morgan et al.  
195 (2011)). Until such research comes to fruition, these needs can be met through  
196 active-surveillance strategy using multi-parametric MRI techniques (Hoeks et al.  
197 (2011), Moore et al. (2013)). An MRI-CAD system, which is an area of active  
198 research and forms the focus of this paper, can be incorporated into this screening  
199 strategy allowing a more systematic and rigorous follow-up.

200 Another weakness of the current screening strategy lies in the fact that TRUS  
201 biopsy does not provide trustworthy results. Due to its “blind” nature, there is  
202 a chance of missing aggressive tumours or detecting microfocal “cancers”, which  
203 influences the aggressiveness-assessment procedure (Noguchi et al. (2001)). As a  
204 consequence, over-diagnosis is estimated at up to 30 % (Haas et al. (2007)), while  
205 missing clinically significant CaP is estimated at up to 35 % (Taira et al. (2010)).  
206 In an effort to solve both issues, alternative biopsy approaches have been explored.

---

<sup>1</sup>The European Randomized Study of Screening for Prostate Cancer (ERSSPC) started in the 1990s in order to evaluate the effect of PSA screening on mortality rate.

<sup>2</sup>The Prostate Lung Colorectal and Ovarian (PLCO) cancer screening trial is carried out in the United States and intends to ascertain the effects of screening on mortality rate.

MRI/US-guided biopsy has been shown to outperform standard TRUS biopsy (De-longchamps et al. (2013)). There, multimodal MRI images are fused with US images in order to improve localization and aggressiveness assessment to carry out biopsies. Human interaction plays a major role in biopsy sampling which can lead to low repeatability; by reducing potential human errors at this stage, the CAD framework can be used to improve repeatability of examination.

CaP detection and diagnosis benefit from the use of CAD and MRI techniques. In the following sections, these techniques will be presented in addition to an overview of CAD for CaP.

### 2.3.2. Imaging techniques: MRI - MRSI

MRI provides promising imaging techniques to overcome the previous mentioned drawbacks. Unlike TRUS biopsy, MRI examination is a non-invasive protocol and has been shown to be the most acute and harmless technique available currently (Turkbey and Choyke (2012)). In this section, we review different MRI techniques developed for CaP detection and diagnosis. Features strengthening each modality, will receive particular attention together with their drawbacks. Commonly, these features form the basis for developing analytic tools and automatic algorithms. However, we refer the reader to Sect. 4.2 for more details on automatic feature detection methods since they are part and parcel of the CAD framework. Table 2.3.2 provides an overview of the following discussion.

- **$T_2$ -W MRI:**  $T_2$ -W MRI was the first MRI-modality used to perform CaP diagnosis using MRI (Hricak et al. (1983)). Nowadays, radiologists make use of it for CaP detection, localization and staging purposes. This imaging technique is well suited to render zonal anatomy of the prostate (Barentsz et al. (2012)).

This modality relies on a sequence based on setting a long repetition time (TR), reducing the  $T_1$  effect in nuclear magnetic resonance (NMR) signal measured, and fixing the echo time (TE) to sufficiently large values in order to enhance the  $T_2$  effect of tissues. Thus, PZ and CG tissues are well perceptible in these images. The former is characterized by an intermediate/high-SI while the latter is depicted by a low-SI (Hricak et al. (1987)). An example of a healthy prostate is shown in Fig. 3(a).

In PZ, round or ill-defined low-SI masses are synonymous with CaPs (Hricak et al. (1983)) as shown in Fig. 3(b). Detecting CaP in CG is more challenging. In fact both normal CG tissue and malignant tissue, have a low-SI in  $T_2$ -W MRI reinforcing difficulties to distinguish between them. However, CaPs in CG appear often as homogeneous mass possessing ill-defined edges with lenticular or “water-drop” shapes (Akin et al. (2006), Barentsz et al. (2012)) as depicted in Fig. 3(c).



Table 1: Overview of the features associated with each MRI-MRSI. Acronyms: prostate cancer (CaP) - signal intensity (SI) - Gleason score (GS).

Modality	Significant features	CaP	Healthy tissue	GS correlation
T <sub>2</sub> -W MRI	SI	low-SI	intermediate to high-SI	+
T <sub>2</sub> map	SI	low-SI	intermediate to high-SI	+
DCE MRI	Semi-quantitative features: – wash-in – wash-out – integral under the curve – maximum signal intensity – time-to-peak enhancement	faster faster higher higher faster	slower slower lower lower slower	0 0 0 0 0
	Quantitative features (Tofts' parameters): – $k_{ep}$ – $K^{trans}$	higher higher	lower lower	0 0
DW MRI	SI	higher-SI	lower-SI	+
ADC map	SI	low-SI	high-SI	+
MRSI	Metabolites: Citrate (2.64 ppm) Choline (3.21 ppm) Spermine (3.11 ppm)	lower concentration higher concentration lower concentration	higher concentration lower concentration higher concentration	+

Notes:

+ = significantly correlated.

0 = no correlation.

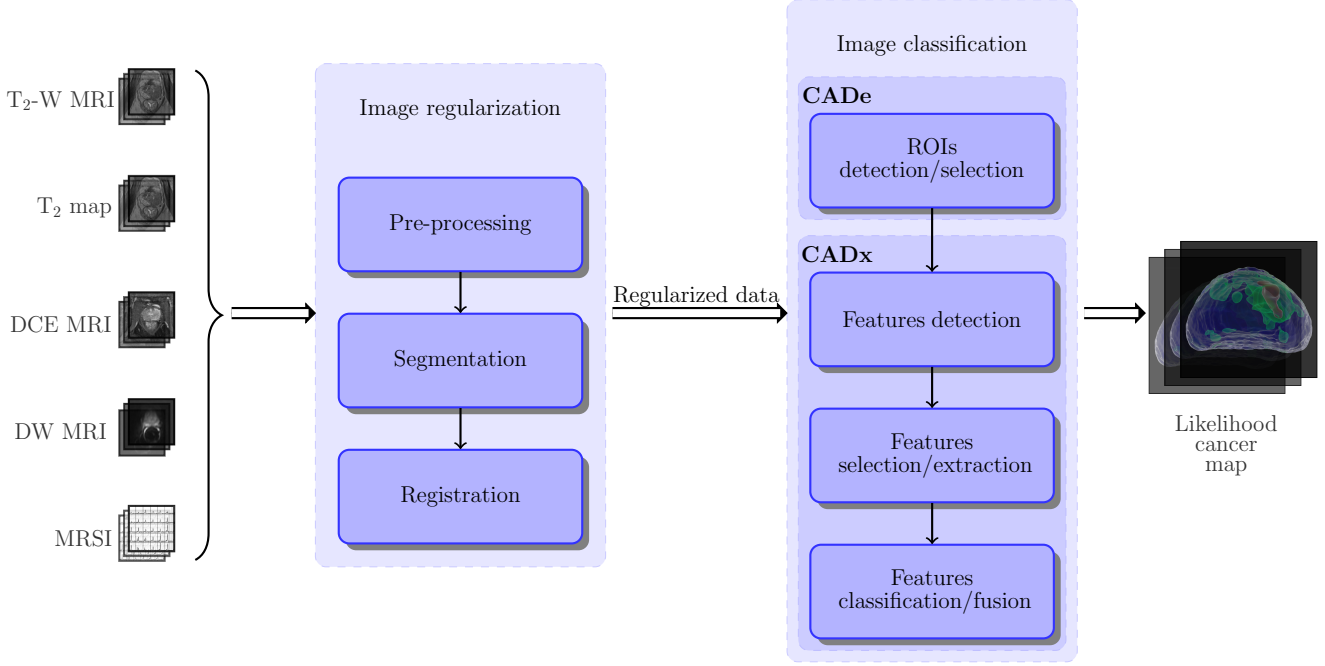
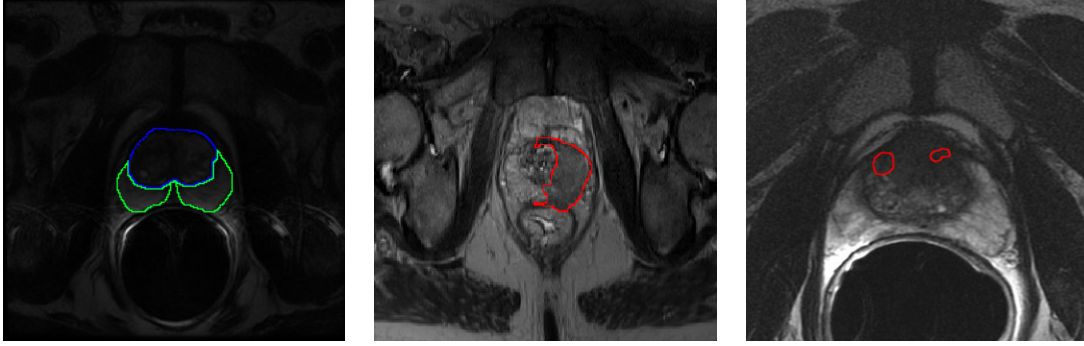


Figure 2: CAD framework using MRI images. Multiparametric MRI images are provided as inputs. These data arise from heterogeneous sources and need to be regularized. Some studies do not consider this stage as mandatory and do not implement or only partly those processes (see Tab. 2). A pre-processing stage is usually applied to standardize the intensity of images, reduce noise and artefacts. Then, in the image set, the prostate organ has to be segmented to focus the next processing stages only on that particular ROI. Moreover, prostate location can vary depending of the modality chosen. Therefore, the images are registered so that all segmented images will be in the same reference frame. Once the image regularisation performed, image classification can be carried out. First, a strategy defining ROIs to focus on is decided. Then, distinctive features are extracted before to be post-processed to select the most salient features. Finally, these salient features will feed a classifier previously trained which will provide a likelihood cancer map associated with either CaP detection or diagnosis.



(a) T<sub>2</sub>-W-MRI slice of a healthy prostate acquired with a 1.5 Tesla MRI. The blue contour represents the CG while the PZ corresponds to the green contour.

(b) T<sub>2</sub>-W-MRI slice of a prostate with a CaP highlighted in the PZ using a 3.0 Tesla MRI scanner.

(c) T<sub>2</sub>-W-MRI slice of a prostate with a CaP highlighted in the CG using a 3.0 Tesla MRI scanner.

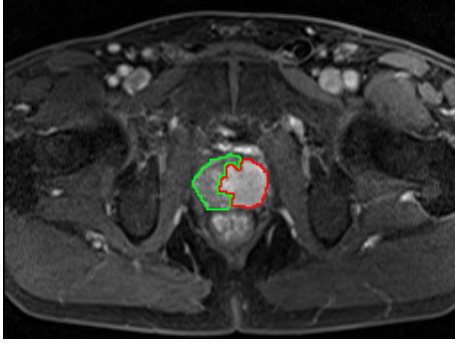
Figure 3: Rendering of T<sub>2</sub>-W-MRI prostate image with both 1.5 and 3.0 Tesla MRI scanner.

CaP aggressiveness was shown to be inversely correlated with SI. Indeed, CaPs assessed with a GS of 4-5 implied lower SI than the one with a GS of 2-3 (Wang et al. (2008)).

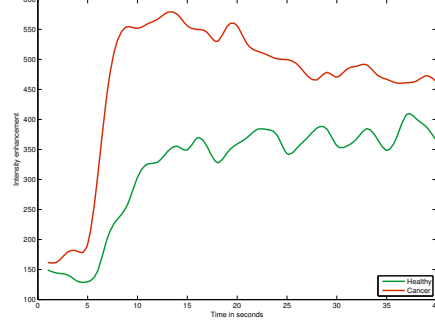
In spite of the availability of these useful and encouraging features, the T<sub>2</sub>-W modality lacks reliability (Hoeks et al. (2011), Kirkham et al. (2006)). Sensitivity is affected by the difficulties in detecting cancers in CG (Kirkham et al. (2006)) while specificity rate is highly affected by outliers (Barentsz et al. (2012)). In fact, various conditions emulate patterns of CaP such as BPH, post-biopsy haemorrhage, atrophy, scars and post-treatment (Barentsz et al. (2012), Cruz et al. (2002), Hricak et al. (1987), Quint et al. (1991), Scheidler et al. (1999b)). These issues can be partly addressed using more innovative and advanced modalities.

- **T<sub>2</sub> Map:** As previously mentioned, T<sub>2</sub>-W MRI modality shows low sensitivity. Moreover, T<sub>2</sub>-W MRI images are a composite of multiple effects (Hegde et al. (2013)). However, T<sub>2</sub> values alone have been shown to be more discriminative (Liu et al. (2011)) and highly correlated with citrate concentration, a biological marker in CaP (Liney et al. (1996b, 1997)).

T<sub>2</sub> values are computed using the characteristics of transverse relaxation.



(a) T<sub>1</sub>-W-MRI image where the cancer is delimited by the red contour. The green area was still not invaded by the CaP



(b) Enhancement curve computed during the DCE-MRI analysis. The red curve is typical from CaP cancer while the green curve is characteristic of healthy tissue.

Figure 4: Illustration of typical enhancement signal observed in DCE-MRI analysis collected with a 3.0 Tesla MRI scanner.

261 Transverse relaxation is formalized as:

$$M_{x,y}(t) = M_{x,y}(0) \exp\left(-\frac{t}{T_2}\right), \quad (1)$$

262 where  $M_{x,y}(0)$  is the initial value of  $M_{x,y}(t)$  and  $T_2$  is the relaxation time.

263 By rearranging Eq. 1,  $T_2$  map is computed performing a linear fitting on the  
264 model in Eq. 2 using several TE,  $t = \{TE_1, TE_2, \dots, TE_m\}$ .

$$\ln \left[ \frac{M_{x,y}(t)}{M_{x,y}(0)} \right] = -\frac{t}{T_2}. \quad (2)$$

265 The Fast Spin-Echo (FSE) sequence has been shown to be particularly well  
266 suited in order to build a  $T_2$  map and obtain accurate  $T_2$  values (Liney et al.  
267 (1996a)).

268 Similar to  $T_2$ -W MRI,  $T_2$  values associated with CaP are significantly lower  
269 than those of healthy tissues (Gibbs et al. (2001), Liney et al. (1996b)).

270 – **DCE MRI:** DCE MRI is an imaging technique which exploits the vascular-  
271 ity characteristic of tissues. Contrast media, usually gadolinium-based, is in-  
272 jected intravenously into the patient. The media extravasates from vessels to  
273 extravascular-extracellular space (EES) and is the released back into the vascu-  
274 lature before being eliminated by the kidneys (Gribbestad et al. (2005)). Further-

more, the diffusion speed of the contrast agent may vary due to several parameters: (i) the permeability of the micro-vessels, (ii) their surface area and (iii) the blood flow (Padhani (2002)).

Healthy PZ is mainly made up of glandular tissue, around 70 % (Choi et al. (2007)), which implies a reduced interstitial space restricting exchanges between vessels and EES (Buckley et al. (2004), van Niekerk et al. (2009)). Normal CG has a more disorganised structure, composed of mainly fibrous tissue (Choi et al. (2007), Hoeks et al. (2011)), which facilitates the arrival of the contrast agent in EES (van Niekerk et al. (2013)). To understand the difference between contrast media kinetic in malignant tumours and the two previous behaviours mentioned, one has to focus on the process known as angiogenesis (Carmeliet and Jain (2000)). In order to ensure growth, malignant tumours produce and release angiogenic promoter substances (Carmeliet and Jain (2000)). These molecules stimulate the creation of new vessels towards the tumour (Carmeliet and Jain (2000)). However, the new vessel networks in tumours differ from those present in healthy tissue (Gribbestad et al. (2005)). They are more porous due to the fact that their capillary walls have a large number of “openings” (Choi et al. (2007), Gribbestad et al. (2005)). In contrast to healthy cases, this increased vascular permeability results in increased contrast agent exchanges between vessels and EES (Verma et al. (2012)).

By making use of the previous aspects, DCE MRI is based on an acquisition of a set of  $T_1$ -W MRI images over time. the Gadolinium-based contrast agent shortens  $T_1$  relaxation time enhancing contrast in  $T_1$ -W MRI images. The aim is to post-analyse the pharmacokinetic behaviour of the contrast media concentration in prostate tissues (Verma et al. (2012)). The image analysis is carried out in two dimensions: (i) in the spatial domain on a pixel-by-pixel basis and (ii) in the time domain corresponding to the consecutive images acquired with the MRI. Thus, for each spatial location, a signal linked to contrast media concentration is measured as shown in Fig. 4(b) (Tofts (2010)).

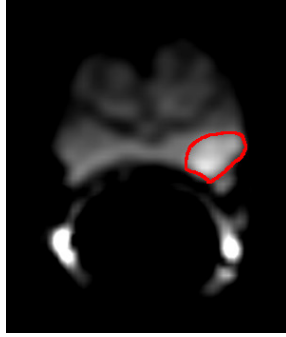
By taking the previous remarks regarding medical aspects and signal theory into account, CaPs are characterized by a signal having an earlier and faster enhancement and an earlier wash-out (cf., the rate of the contrast agent flowing out of the tissue) (see Fig. 4(b)) (Verma et al. (2012)). Three different approaches exist to analyse these signals with the aim of tagging them as corresponding to either normal or malignant tissues. Qualitative analysis is based on assessment of the signal shape (Hoeks et al. (2011)). Quantitative approaches consist of inferring pharmacokinetic parameter values (Tofts (2010)). Those parameters are part of mathematical-pharmacokinetic models which are directly based on physiological

exchanges between vessels and EES. Several pharmacokinetic models were proposed such as the Kety model (Kety (1951)), the Tofts model (Tofts (1997)) and mixed models (Larsson et al. (1996), St Lawrence and Lee (1998)). The last family of methods mixed both approaches and are grouped together under the heading of semi-quantitative methods. They rely on shape characterization using mathematical modelling to extract a set of parameters such as wash-in gradient, wash-out, integral under the curve, maximum signal intensity, time-to-peak enhancement and start of enhancement. These parameters will be discussed in a later section (see Fig. 17) (Hoeks et al. (2011), Verma et al. (2012)). It was shown that semi-quantitative and quantitative methods improve localization of CaP when compared with qualitative methods (Rosenkrantz et al. (2013)). Section 4.2.2 provides a full description of quantitative and semi-quantitative approaches.

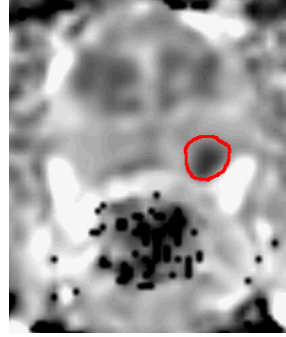
DCE MRI combined with T<sub>2</sub>-W MRI has shown to enhance sensitivity compared to T<sub>2</sub>-W MRI alone (Jager et al. (1997), Kim et al. (2005), Schlemmer et al. (2004), Zelhof et al. (2009)). Despite this fact, DCE MRI possesses some drawbacks. Due to its “dynamic” nature, patient motions during the image acquisition lead to spatial misregistration of the image set (Verma et al. (2012)). Furthermore, it has been suggested that malignant tumours are difficult to distinguish from prostatitis located in PZ and BPH located in CG (Hoeks et al. (2011), Verma et al. (2012)). These pairs of tissues tend to have similar appearances. Later studies have shown that CaPs in CG do not always manifest in homogeneous fashion. Indeed, tumours in this zone can present both hypo-vascularization and hyper-vascularization which illustrates the challenge of CaP detection in CG (van Niekerk et al. (2013)).

- **DW MRI:** As previously mentioned in the introduction, DW MRI is the most recent MRI imaging technique aiming at CaP detection and diagnosis (Scheidler et al. (1999b)). This modality exploits the variations in the motion of water molecules in different tissues (Koh and Collins (2007), Le Bihan et al. (1988)).

From a physiological point of view, the following facts can be claimed. On the one hand, PZ, as previously mentioned, is mainly glandular and tubular in structure allowing water molecules to move freely (Choi et al. (2007), Hoeks et al. (2011)). On the other hand, CG is made up of muscular or fibrous tissue causing the motion of the water molecules to be more constrained and heterogeneous than in PZ (Hoeks et al. (2011)). Then, CaP growth leads to the destruction of normal glandular structure and is associated with an increase in cellular density (Hoeks et al. (2011), Koh and Collins (2007), Somford et al. (2008)). Furthermore, these factors both have been shown to be inversely correlated with water diffusion



(a) DW-MRI image acquired with a 1.5 Tesla MRI scanner. The cancer corresponds to the high SI region highlighted in red.



(b) ADC map computer after acquisition of DW-MRI iages with a 1.5 Tesla MRI scanner. The cancer corresponds to the low SI region highlighted in red.

Figure 5: Illustration of of DW-MRI and ADC map. The signal intensity corresponding to cancer are inversely correlated on these two types of imaging techniques.

(Koh and Collins (2007), Somford et al. (2008)): higher cellular density implies a restricted water diffusion. Thus, water diffusion in CaP will be more restricted than both healthy PZ and CG (Hoeks et al. (2011), Koh and Collins (2007)).

From the NMR principle side, DW MRI sequence produces contrasted images due to variation of water molecules motion. The method is based on the fact that the signal in DW MRI images is inversely correlated to the degree of random motion of water molecules (Huisman (2003)). In fact, gradients are used in DW MRI modality to encode spatial location of nuclei temporarily. Simplifying the problem in only one direction, a gradient is applied in that direction, dephasing the spins of water nuclei. Hence, the spin phases vary along the gradient direction depending of the gradient intensity at those locations. Then, a second gradient is applied aiming at cancelling the spin dephasing. Thus, the immobile water molecules will be subject to the same gradient intensity as the initial one while moving water molecules will be subject to a different gradient intensity. Thus, spins of moving water molecules will stay dephased whereas spins of immobile water molecules will come back in phase. As a consequence, a higher degree of random motion results in a more significant signal loss whereas a lower degree of random motion is synonymous with lower signal loss (Huisman (2003)). Under

368 these conditions, the MRI signal is measured as:

$$M_{x,y}(t, b) = M_{x,y}(0) \exp\left(-\frac{t}{T_2}\right) S_{\text{ADC}}(b) , \quad (3)$$

$$S_{\text{ADC}}(b) = \exp(-b \times \text{ADC}) , \quad (4)$$

369 where  $S_{\text{ADC}}$  refers to signal drop due to diffusion effect, ADC is the apparent  
 370 diffusion coefficient and  $b$  is the attenuation coefficient depending only on gradient  
 371 pulses parameters: (i) gradient intensity and (ii) gradient duration (Le Bihan et al.  
 372 (1986)).

373 By using this formulation, image acquisition with a parameter  $b = 0 \text{ s.mm}^{-2}$   
 374 corresponds to a  $T_2$ -W MRI acquisition. Then, increasing the attenuation coef-  
 375 ficient  $b$  (cf., increase gradient intensity and duration) enhances the contrast in  
 376 DW MRI images.

377 To summarize, in DW MRI images, CaPs are characterized by high-SI com-  
 378 pared to normal tissues in PZ and CG as shown in Fig. 5(a) (Barentsz et al.  
 379 (2012)). However, some tissues in CG can look similar to CaP with higher SI  
 380 (Barentsz et al. (2012)).

381 Diagnosis using DW MRI combined with  $T_2$ -W MRI has shown a significant  
 382 improvement compared with  $T_2$ -W MRI alone and provides highly contrasted  
 383 images (Choi et al. (2007), Padhani (2011), Shimofusa et al. (2005)). As draw-  
 384 backs, this modality suffers from poor spatial resolution and specificity due to  
 385 false positive detection (Choi et al. (2007)).

386 With a view to eliminate these drawbacks, radiologists are extracting quanti-  
 387 tative maps from DW MRI. This imaging technique is presented next.

388 – **ADC Map:** The NMR signal measured for DW MRI images is not only affected  
 389 by diffusion as shown in Eq. (3). However, the signal drop (Eq. (4)) is formulated  
 390 such that the only variable is the acquisition parameter  $b$  (Le Bihan et al. (1986)).  
 391 The ADC is considered as a “pure” diffusion coefficient and can be extracted to  
 392 build a quantitative map.

393 From Eq. (3), it is clear that performing multiple acquisitions only varying  $b$   
 394 will not have any effect on the term  $M_{x,y}(0) \exp\left(-\frac{t}{T_2}\right)$ . Thus, Eq. (3) can be  
 395 rewritten as:

$$S(b) = S_0 \exp(-b \times \text{ADC}) . \quad (5)$$

396 To compute the ADC map, a minimum of two acquisitions are necessary: (i)  
 397 for  $b_0 = 0 \text{ s.mm}^{-2}$  where the measured signal is equal to  $S_0$ , and (ii)  $b_1 > 0$



398 s.mm<sup>-2</sup> (typically 1000 s.mm<sup>-2</sup>). Then, the ADC map can be computed as:

$$\text{ADC} = -\frac{\ln\left(\frac{S(b_1)}{S_0}\right)}{b_1} . \quad (6)$$

399 More accurate computation of the ADC map can be obtained by performing  
400 several acquisitions with different values for the parameter  $b$  and performing a  
401 semi-logarithmic linear fitting using the model presented in Eq. (5).

402 Regarding the appearance of the ADC maps, it was previously stated that by  
403 increasing the value of  $b$ , the signal of CaP tissue increases significantly. From Eq.  
404 (6), it can be shown that tissue appearance in the ADC map will be the inverse  
405 of DW MRI images. Then, CaP tissue is associated with low-SI whereas healthy  
406 tissue appears brighter as depicted in Fig. 5(b) (Barentsz et al. (2012)).

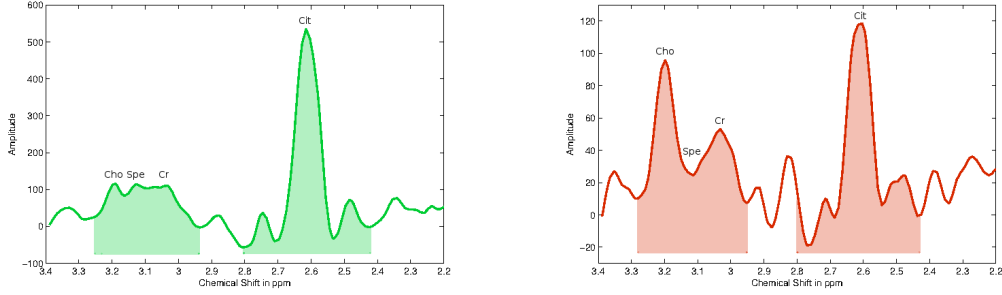
407 Similar to the gain achieved by DW MRI, diagnosis using ADC map combined  
408 with T<sub>2</sub>-W MRI significantly outperforms T<sub>2</sub>-W MRI alone (Choi et al. (2007),  
409 Doo et al. (2012)). Moreover, it has been shown that ADC is correlated with GS  
410 (Hambrock et al. (2011), Itou et al. (2011), Peng et al. (2013)).

411 However, some tissues of the CG zone mimic CaP with low-SI (Kirkham et al.  
412 (2006)) and image distortion can arise due to haemorrhage (Choi et al. (2007)).  
413 It has also been noted that a high variability of the ADC occurs between different  
414 patients making it difficult to define a static threshold to distinguish CaP from  
415 non-malignant tumours (Choi et al. (2007)).

416 – **MRSI:** CaP induces metabolic changes in the prostate compared with healthy  
417 tissue. Thus, CaP detection can be carried out by tracking changes of metabo-  
418 lite concentration in prostate tissue. MRSI is an NMR-based technique which  
419 generates spectra of relative metabolite concentration in a ROI.

420 In order to track changes of metabolite concentration, it is important to know  
421 which metabolites are associated with CaP. To address this question, clinical stud-  
422 ies identified three biological markers: (i) citrate, (ii) choline and (iii) polyamines  
423 composed mainly of spermine, and in less abundance of spermidine and putrescine  
424 (Awwad et al. (2012), Costello and Franklin (2006), Giskeodegard et al. (2013)).

425 Citrate is involved in the production and secretion of the prostatic fluid, and  
426 the glandular prostate cells are associated with a high production of citrate en-  
427 abled by zinc accumulation by these same cells (Costello and Franklin (2006)).  
428 However, the metabolism allowing the accumulation of citrate requires a large  
429 amount of energy (Costello and Franklin (2006)). In contrast, malignant cells  
430 do not have high zinc levels leading to lower citrate levels due to citrate oxyda-



(a) Illustration of an MRSI spectrum of a healthy voxel acquired with a 3.0 Tesla MRI. (b) Illustration of an MRSI spectrum of a cancerous voxel acquired with a 3.0 Tesla MRI.

Figure 6: Illustration of an MRSI spectrum both healthy and cancerous voxel with a 3.0 Tesla MRI. The highlighted areas corresponds to the related concentration of the metabolites which is computed by integrating the area under each peak. Acronyms: Choline (Cho), Spermine (Spe), Creatine (Cr) and Citrate (Cit).

tion (Costello and Franklin (2006)). Furthermore, this change results in a more energy-efficient metabolism enabling malignant cells to grow and spread (Costello and Franklin (2006)).

An increased concentration of choline is related to CaP (Awwad et al. (2012)). Malignant cell development requires epigenetic mechanisms resulting in metabolic changes and relies on two mechanisms: DNA methylation and phospholipid metabolism which both result in choline uptake, explaining its increased level in CaP tissue (Awwad et al. (2012)).

Spermine is also considered as a biological marker in CaP (Giskeodegard et al. (2013), van der Graaf et al. (2000)). In CaP, reduction of the ductal volume due to shifts in polyamine homeostasis might lead to a reduced spermine concentration (van der Graaf et al. (2000)).

To determine the concentration of these biological markers, one has to focus on the MRSI modality. In theory, in presence of a homogeneous magnetic field, identical nuclei precesses at the same operating frequency known as the Larmor frequency (Haacke et al. (1999)). However, MRSI is based on the fact that identical nuclei will slightly precess at different frequencies depending on the chemical environment in which they are immersed (Haacke et al. (1999)), a phenomenon known as the chemical shift effect (CSE) (Parfait (2010)). Given this property, metabolites can be identified and their concentrations can be determined. In this regard, the Fourier transform is used to obtain the frequency spectrum of the

452 NMR signal (Haacke et al. (1999), Parfait (2010)). In this spectrum, each peak is  
453 associated with a particular metabolite and the area under each peak corresponds  
454 to the relative concentration of this metabolite (see Fig. 6) (Parfait (2010)).

455 Two different quantitative approaches are used to decide or whether not the  
456 spectra of a ROI is associated with CaP classified either as relative quantification  
457 or absolute quantification (Lemaître (2011)). In relative quantification, the ratio  
458 of choline-polyamines-creatine to citrate is computed. The integral of the signal  
459 is computed from choline (cf., 3.21 ppm) to creatine (cf., 3.02 ppm) because the  
460 peaks in this region can be merged at clinical magnetic field strengths (see Fig.  
461 6) (van der Graaf et al. (2000), Hoeks et al. (2011)). Considering the previous  
462 assumption that choline concentration rises and citrate concentration decreases  
463 in the presence of CaP, the ratio computed should be higher in malignant tissue  
464 than in healthy tissue.

465 Two different quantitative approaches are used to decide or not the spectra  
466 of a ROI is associated with CaP classified either as relative quantification or  
467 absolute quantification (Lemaître (2011)). In relative quantification, the ratio of  
468 choline-polyamines-creatine to citrate is computed. The integral of the signal is  
469 computed from choline (cf., 3.21 ppm) to creatine (cf., 3.02 ppm) because the  
470 peaks in this region can be merged at clinical magnetic field strengths (see Fig.  
471 6) (van der Graaf et al. (2000), Hoeks et al. (2011)). Considering the previous  
472 assumption that choline concentration rises and citrate concentration decreases  
473 in the presence of CaP, the ratio computed should be higher in malignant tissue  
474 than in healthy tissue.

475 In contrast with relative quantification, absolute quantification measures mo-  
476 lar concentrations by normalizing relative concentrations using water as reference  
477 (Lemaître (2011)). In this case, “true” concentrations are directly used to differ-  
478 entiate malignant from healthy tissue. However, this method is not commonly  
479 used as it requires an additional step of acquiring water signals, inducing time  
480 and cost acquisition constraints.

481 MRSI allows examination with high specificity and sensitivity compared to  
482 other MRI modalities (Choi et al. (2007)). Furthermore, it has been shown that  
483 combining MRSI with MRI improves detection and diagnosis performance (Kaji  
484 et al. (1998), Scheidler et al. (1999a), Vilanova et al. (2009)). Citrate and spermine  
485 concentrations are inversely correlated with the GS allowing us to distinguish low  
486 from high grade CaPs (Giskeodegard et al. (2013)). However, choline concentra-  
487 tion does not provide the same properties (Giskeodegard et al. (2013)).

488 Unfortunately, MRSI also presents several drawbacks. First, MRSI acquisition  
489 is time consuming which prevents this modality from being used in daily clini-

cal practise (Barentsz et al. (2012)). In addition, MRSI suffers from low spatial resolution due to the fact that signal-to-noise (SNR) is linked to the voxel size. However, this issue is addressed by developing new scanners with higher magnetic field strengths such as 7.5 T (Giskeodegard et al. (2013)). Finally, a high variability of the relative concentrations between patients was observed (Choi et al. (2007)). The same observation was made depending on the zones studied (cf., PZ, CG, base, mid-gland, apex) (Lemaître (2011), Walker et al. (2010)). Due to this variability, it is difficult to use a fixed thresholds in order to differentiate CaP from healthy tissue.

### 2.3.3. Computer-aided systems for CaP: CAdE - CAdx

As previously mentioned in the introduction (see Sect. 1), CADs are developed to advise and backup radiologists in their tasks of CaP detection and diagnosis; CADs are not aimed to provide fully automatic decisions (Giger et al. (2008)). CADs can be divided into two different sub-groups either as CAdE, with the purpose to highlight probable lesions in MRI images, or CAdx, which focuses on differentiating malignant from non-malignant tumours (Giger et al. (2008)). Moreover, an intuitive approach, motivated by developing a framework combining detection-diagnosis, is to mix both CAdE and CAdx by using the output of the former mentioned as a input of the latter named. Although the outcomes of these two systems should differ, the framework of both CAD systems is similar. The CAD work-flow is presented in Fig. 2.3.2.

MRI modalities mentioned in Sect. 2.3.2 are used as inputs of CAD for CaP. It can be noted that ADC map is not considered as an input since it is a feature derived from the DW MRI images. The images acquired from the different modalities show a large variability between patients: the prostate organ can be located at different positions in images (e.g., patient motion, variation of acquisition plan), and the SI can be corrupted with noise or artefacts during the acquisition process (eg., magnetic field inhomogeneity, use of endorectal coil). To address these issues, the first stage of CAD is to pre-process multiparametric MRI images to reduce noise, remove artefacts and standardize the SI. Then, it is important to mention that most of the later processes would be only focused on the prostate. Thus, it is necessary to segment the prostate in each MRI-modality to define it as a ROI. However, data suffers of misalignment due to patient motions or different acquisition plan. Therefore, a registration step is performed so that all the previously segmented MRI images will be in the same reference frame.

Some studies do not fully apply the methodology depicted in Fig. 2.3.2. Details about those can be found in Tab. 2. Some studies preferred to work directly with raw data in order to demonstrate the robustness of their approaches to noise or artefacts.

528 In some cases, prostate segmentation is performed manually as well as registration.  
529 It is also sometimes assumed that no patient motions occur during the acquisition  
530 procedure, removing the need of registering the multiparametric MRI images.

531 Once the data are regularized, it becomes possible to extract features and classify  
532 the data to obtain the probabilistic maps. We referred this stage to image classification  
533 where CADe and CADx are the main components.

534 In a CADe framework, possible lesions will be segmented automatically and further  
535 used as input of CADx. We also included in CADe studies, the methods using  
536 voxel-based delineation in which the final results will highlight the boundaries of the  
537 lesions. On the other hand, manual lesions segmentation are not considered to be  
538 part of a CADe. The output of the CADe is used as input of the CADx.

539 CADx is composed of the processes allowing to distinguish malignant from non-  
540 malignant tumours. We divided CADx into three different stages. First, salient  
541 features are extracted, in an pixel-based or region-based manner, from MRI images  
542 to characterize the lesion. Of course, more discriminative features will be associated  
543 with a robust and accurate likelihood cancer map. Frequently, the number of features  
544 extracted can be large resulting in redundant or insufficient discriminative features  
545 which will negatively affect the performances of the further classification. Therefore,  
546 a step consists of selecting the best features or/and reducing the number of dimensions  
547 is commonly used. Then, this modified feature vector is finally classified using  
548 different pattern recognition approaches.

549 As pointed out in the introduction, performance of CaP detection and diagnosis  
550 are affected by observer interpretation and limitations (Giger et al. (2008), Hambrock  
551 et al. (2013)). CAD offers a possible solution in order to reduce this variability. As  
552 mentioned in the introduction, the effects of CAD on the observer performance has  
553 been studied (Hambrock et al. (2013)), with results showing that CADs benefit to  
554 less-experienced radiologist to perform similarly as experienced radiologist in their  
555 tasks (Hambrock et al. (2013)).

#### 556 2.4. Literature classification

Table 2: Overview of the different studies reviewed with their main characteristics. Acronyms: number (#) - image regularization (Img. Reg.).

Index	Study	# patients	MRI-modality				Strength of field		Studied zones		CAD stages		
			T <sub>2</sub> -W MRI	DCE MRI	DW MRI	MRSI	1.5 T	3.0 T	PZ	CG	Img. Reg.	CADe	CADx
[1]	Ampeliotis et al. (2007)	25	✓	✓	✗	✗	✓	✗	✓	✗	✓!	✗	✓
[2]	Ampeliotis et al. (2008)	25	✓	✓	✗	✗	✓	✗	✓	✗	✓!	✗	✓
[3]	Antic et al. (2013)	53	✓	✗	✓	✗	✓	✗	✓	✓	✗	✗	✓
[4]	Artan et al. (2009)	10	✓	✓	✓	✗	✓	✗	✓	✗	✗	✓	✓
[5]	Artan et al. (2010)	21	✓	✓	✓	✗	✓	✗	✓	✗	✓!	✓	✓
[6]	Chan et al. (2003)	15	✓	✗	✓	✗	✓	✗	✓	✗	✗	✗	✓
[7]	Giannini et al. (2013)	10	✓	✓	✓	✗	✓	✗	✓	✗	✓	✓	✓
[8]	Kelm et al. (2007)	24	✗	✗	✗	✓	✓	✗	✓	✓	✓!	✓	✓
[9]	Langer et al. (2009)	25	✓	✓	✓	✗	✓	✗	✓	✗	✓!	✗	✓
[10]	Litjens et al. (2011)	188	✓	✓	✓	✗	✗	✓	✓	✗	✓!	✓	✓
[11]	Litjens et al. (2012b)	288	✓	✓	✓	✗	✗	✓	✓	✓	✓!	✓	✓
[12]	Liu et al. (2009)	11	✓	✓	✓	✗	✓	✗	✓	✗	✓!	✓	✓
[13]	Liu et al. (2013)	54	✓	✓	✓	✗	✗	✓	✓	✓	✓!	✗	✓
[14]	Lopes et al. (2011)	27	✓	✗	✗	✗	✓	✗	✓	✗	✓!	✓	✓
[15]	Lv et al. (2009)	55	✓	✗	✗	✗	✓	✗	✓	✗	✓!	✗	✓
[16]	Matulewicz et al. (2013)	18	✗	✗	✗	✓	✗	✓	✓	✓	✗	✓	✓
[17]	Mazzetti et al. (2011)	10	✗	✓	✗	✗	✓	✗	✓	✗	✓!	✓	✓
[18]	Niaf et al. (2011)	23	✓	✓	✓	✗	✓	✗	✓	✗	✓!	✗	✓
[19]	Niaf et al. (2012)	30	✓	✓	✓	✗	✓	✗	✓	✗	✓!	✗	✓
[20]	Ozer et al. (2009)	20	✓	✓	✓	✗	✓	✗	✓	✗	✓!	✓	✓
[21]	Ozer et al. (2010)	20	✓	✓	✓	✗	✓	✗	✓	✗	✓!	✓	✓
[22]	Parfait et al. (2012)	22	✗	✗	✗	✓	✗	✓	✓	✓	✓!	✓	✓
[23]	Peng et al. (2013)	48	✓	✓	✓	✗	✗	✓	✓	✓	✗	✗	✓
[24]	Puech et al. (2009)	100	✗	✓	✗	✗	✓	✗	✓	✓	✗	✗	✓
[25]	Sung et al. (2011)	42	✗	✓	✗	✗	✗	✓	✓	✓	✗	✓	✓
[26]	Tiwari et al. (2007)	14	✗	✗	✗	✓	✓	✗	✓	✓	✓!	✓	✓
[27]	Tiwari et al. (2008)	18	✗	✗	✗	✓	✓	✗	✓	✓	✓!	✓	✓
[28]	Tiwari et al. (2009a)	18	✗	✗	✗	✓	✓	✗	✓	✓	✓!	✓	✓
[29]	Tiwari et al. (2009b)	15	✓	✗	✗	✓	✓	✗	✓	✓	✓!	✓	✓
[30]	Tiwari et al. (2010)	19	✓	✗	✗	✓	✓	✗	✓	✓	✓!	✓	✓
[31]	Tiwari et al. (2012)	36	✓	✗	✗	✓	✓	✗	✓	✓	✗	✓	✓
[32]	Tiwari et al. (2013)	29	✓	✗	✗	✓	✓	✗	✓	✓	✓!	✓	✓
[33]	Viswanath et al. (2008b)	16	✓	✗	✗	✓	✓	✗	✓	✓	✗	✓	✓
[34]	Viswanath et al. (2008a)	6	✓	✓	✗	✗	✗	✓	✓	✓	✓!	✓	✓
[35]	Viswanath et al. (2009)	6	✓	✓	✗	✗	✗	✓	✓	✓	✓	✓	✓
[36]	Viswanath et al. (2011)	12	✓	✓	✓	✗	✗	✓	✓	✓	✓!	✓	✓
[37]	Viswanath et al. (2012)	22	✓	✗	✗	✗	✗	✓	✓	✓	✓	✓	✓
[38]	Vos et al. (2008a)	29	✓	✓	✗	✗	✓	✗	✓	✗	✓!	✗	✓
[39]	Vos et al. (2008b)	29	✗	✓	✗	✗	✓	✗	✓	✗	✓!	✗	✓
[40]	Vos et al. (2010)	29	✓	✓	✗	✗	✓	✗	✓	✗	✓!	✗	✓
[41]	Vos et al. (2012)	NA	✓	✓	✓	✗	✗	✓	✓	✗	✓!	✓	✓

Notes:  
✗: not used or not implemented.  
✓!: partially implemented.  
✓: used or implemented.

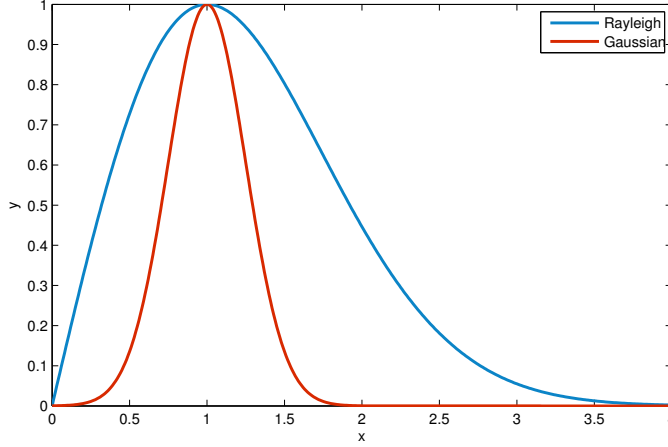


Figure 7: Illustration of a Gaussian distribution ( $\mu = 1, \sigma = 0.25$ ) and a Rayleigh distribution ( $\sigma = 2$ ). It can be seen that the Rayleigh distribution is suffering of a bias term when compared with the Gaussian distribution.

The CAD review is organized using the methodology presented in Fig. 2.3.2. Methods embedded in the image regularization framework are presented before to focus on the image classification framework, the later being divided into CADe and CADx. Table 2 summarizes the different CAD studies reviewed in this paper. Characteristics related to MRI acquisition as well as CAD strategies are reported. Only methods used in CAD system are discussed.

### 3. Image regularization framework

This section provides a review of the methods used in CADs in order to regularize input images. We start with pre-processing methods presented in Sect. 3.1, focusing mainly on the reduction of noise level and artefacts as well as standardization of SI. Sections 3.2 and 3.3 will be dedicated to segmentation methods, so that later methods only operate on the segmented prostate, and registration to align segmented images from different MRI-modalities in the same reference frame.

#### 3.1. Pre-processing

##### 3.1.1. MRI images pre-processing

Three different groups of pre-processing methods are commonly applied to images as initial stage in CAD.

Table 3: Overview of the pre-processing methods used in CAD systems.

Pre-processing operations	References
<i>MRI pre-processing:</i>	
Noise filtering:	
Median filtering	[20-21]
Wavelet-based filtering	[1-2,14]
Bias correction:	
Parametric methods	[15-35]
Non-parametric methods	[36]
Standardization:	
Statistical-based normalization:	[3-4,15,20-21,35,37]
Organ SI-based normalization	[18-19]
<i>MRSI pre-processing:</i>	
Phase correction	[22]
Water and lipid residuals filtering	[8]
Baseline correction	[22,31]
Frequency alignment	[31]
Normalization	[22]



574 – **Noise filtering:** The NMR signal measured and recorded in the k-space dur-  
575 ing an MRI acquisition is affected by noise. This noise obeys a complex Gaussian  
576 white noise mainly due to thermal noises in the patient area (Nowak (1999)). Fur-  
577 thermore, MRI images visualized by radiologists are in fact the magnitude images  
578 resulting from the complex Fourier transform of the k-space data. The complex  
579 Fourier transform, being a linear and orthogonal transform, does not affect the  
580 Gaussian noise characteristics (Nowak (1999)). However, the function involved  
581 in the magnitude computation is a non-linear transform (i.e., the square root of  
582 the sum of squares of real and the imaginary parts), implying that the noise dis-  
583 tribution is no longer Gaussian; it indeed follows a Rician distribution making  
584 the denoising task harder. Briefly, a Rician distribution can be characterized as  
585 follows: in low-SI region (low SNR), it can be approximated with a Rayleigh  
586 distribution while in high-SI region (high SNR), it is similar to a Gaussian distri-  
587 bution (see Fig. 7) (Manjon et al. (2008)). Reviews of all denoising methods can  
588 be found in the work of Buades et al. (2005) and Mohan et al. (2014).

589 Median filtering is the simplest approach used to address the denoising issue in  
590 MRI images (Ozer et al. (2009, 2010)). In both studies, Ozer et al. used a square  
591 kernel of size  $5 \times 5$  pixels with the image resolutions ranging from  $320 \times 256$   
592 (cf.,  $T_2$ -W MRI) to  $256 \times 128$  (cf.,  $T_2$  map, DCE and DW MRI) and a field of  
593 view (FOV) ranging from 14 cm (cf,  $T_2$ -W and DW MRI) to 20 cm (cf,  $T_2$  map  
594 and DCE MRI). However, from a theoretical point of view, this simple filtering  
595 method is not well formalized to address the noise distribution in MRI images.

596 More complex approaches were proposed to overcome this problem. A com-  
597 mon method used to denoise MRI images is based on wavelet-based filtering. This  
598 filtering exploits the sparsity property of the wavelet decomposition. The projec-  
599 tion of a noisy signal from the spatial-domain to the wavelet-domain implies that  
600 only few wavelet coefficients contribute to the “signal-free noise” while all wavelet  
601 coefficients contribute to the noise (Donoho and Johnstone (1994)). Therefore,  
602 denoising is performed by thresholding/attenuating the insignificant wavelet coef-  
603 ficients to enforce the sparsity in the wavelet-domain. Investigations focus on the  
604 strategies to perform the most adequate coefficient shrinkage method (e.g., using  
605 thresholding, singularity property or Bayesian framework) (Pizurica (2002)).

606 Ampeliotis et al. (2007, 2008) performed wavelet shrinkage to denoise magni-  
607 tude MRI images (cf.,  $T_2$ -W-MRI and DCE-MRI) using thresholding techniques  
608 (Mallat (2008)). However, since the wavelet transform is an orthogonal transform,  
609 the Rician distribution of the noise is preserved in the wavelet-domain. Hence,  
610 for low SNR, the wavelet and scaling coefficients still suffer from a bias due to  
611 this specific noise distribution (Nowak (1999)).

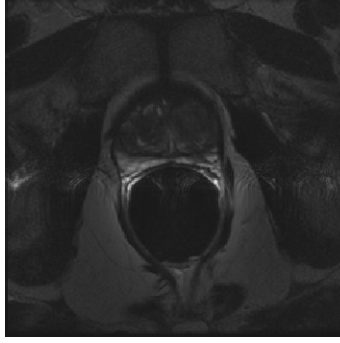


Figure 8: Example of artefacts with high SI due to perturbation from the endorectal coil which create inhomogeneity.

Lopes et al. (2011) used a technique proposed by Pizurica et al. (2003) to denoise T<sub>2</sub>-W-MRI. Pizurica et al. (2003) proposed a filtering technique based on joint detection and estimation theory (Middleton and Esposito (1968)). The wavelet coefficients “free-of-noise” are estimated from the noisy wavelet coefficients using a maximum *a posteriori* (MAP) estimate. Furthermore, the estimator designed takes spatial context into account by including both local and global information in the prior probabilities. The different probabilities needed by the MAP are empirically estimated by using mask images representing the locations of the significant wavelet coefficients. These mask images are computed by thresholding the detail images obtained from the wavelet decomposition. To remove the bias from the wavelet and scaling coefficients, the squared magnitude MRI image used instead of the magnitude MRI image as proposed by Nowak (1999). This involves changing the Rician distribution to a scaled non-central Chi-square distribution. It implies that the wavelet coefficients are also unbiased estimators and the scaling coefficients are unbiased estimators but up to a constant  $C$  as defined in Eq. (7) which needs to be subtracted from each scaling coefficient,

$$C = 2^{(J+1)}\hat{\sigma}^2, \quad (7)$$

where  $J$  is the number of levels of the wavelet decomposition and  $\hat{\sigma}$  is an estimate of the noise standard deviation.

- **Bias correction:** Besides being corrupted by noise, MRI images are also affected by the inhomogeneity of the MRI field commonly referred to as bias field (Styner et al. (2000)). This bias field results in a smooth variation of the SI through the image. When an endorectal coil is used, an artefact resulting of an hyper-

intense signal can be observed around the coil on the images (see Fig. 8). As a consequence, the SI of identical tissues varies depending on their spatial location in the image making further processes such as segmentation or registration harder (Jungke et al. (1987), Vovk et al. (2007)). A review of bias correction methods can be found in Vovk et al. (2007).

The model of image formation is usually formalized such that:

$$s(\mathbf{x}) = o(\mathbf{x})b(\mathbf{x}) + \eta(\mathbf{x}) , \quad (8)$$

where  $s(\mathbf{x})$  is the corrupted SI at the pixel for the image coordinates  $\mathbf{x} = \{x, y\}$ ,  $o(\mathbf{x})$  is the “noise-free signal” ,  $b(\mathbf{x})$  is the bias field function and  $\eta(\mathbf{x})$  is an additive white Gaussian noise.

Hence, the task of bias correction involves estimating the bias function  $b(\mathbf{x})$  in order to infer the “signal-free bias”  $o(\mathbf{x})$ .

Viswanath et al. (2009) performed bias correction on T<sub>2</sub>-W-MRI using a parametric Legendre polynomial model proposed by Styner et al. (2000) and available in the Insight Segmentation and Registration Toolkit (ITK) library<sup>3</sup>. Styner et al. (2000) chose to model the bias field by using a linear combination of Legendre polynomials as:

$$\hat{b}(\mathbf{x}, \mathbf{p}) = \sum_{i=0}^{m-1} p_i f_i(\mathbf{x}) = \sum_{i=0}^l \sum_{j=0}^{l-i} p_{ij} P_i(x) P_j(y) , \quad (9)$$

where  $\hat{b}$  is the bias estimation with the image coordinates  $\mathbf{x} = \{x, y\}$  and the  $m$  coefficients of the linear combination  $\mathbf{p} = p_{11}, \dots, p_{ij}$  ;  $m$  can be defined as  $m = (l+1)\frac{(l+2)}{2}$  where  $l$  is the degree of Legendre polynomials chosen and  $P_i(\cdot)$  denotes a Legendre polynomial of degree  $i$ .

This family of functions allows us to model the bias as a smooth inhomogeneity function across the image. To estimate the set of parameters  $\mathbf{p}$ , a cost function is defined which relies on the following assumptions: (i) an image is composed of  $k$  regions with  $\mu_k$  being the mean SI and a variance  $\sigma_k^2$  of each particular class, and (ii) each noisy pixel belongs to one of the  $k$  regions with its SI value close to the class mean  $\mu_k$ . Hence, the cost function is defined as:

$$C(\mathbf{p}) = \sum_{\mathbf{x}} \prod_k \rho_k(s(\mathbf{x}) - \hat{b}(\mathbf{x}, \mathbf{p}) - \mu_k) , \quad (10)$$

---

<sup>3</sup>The ITK library is available at: <http://www.itk.org/>

$$\rho_k(x) = \frac{x^2}{x^2 + 3\sigma_k^2} , \quad (11)$$

660 where  $\rho_k(\cdot)$  is a M-estimator allowing estimations to be less sensitive to outliers  
 661 than usual square distance (Li (1996)).

662 Finally, estimation of the parameters  $\mathbf{p}$  results in finding the minimum of the  
 663 cost function  $C(\mathbf{p})$ . This optimization was performed using the non-linear (1 + 1)  
 664 Evolution Strategy (ES) optimizer (Styner and Gerig (1997)).

665 In a later publication, Viswanath et al. (2012) make use of the well known  
 666 N3 algorithm<sup>4</sup> to correct T<sub>2</sub>-W-MRI developed by Sled et al. (1998). To estimate  
 667 the bias function, Sled et al. (1998) proposed to estimate the probability density  
 668 functions (PDFs) of the signal and bias.

669 Recalling Eq. (8) and taking advantage of logarithm property, it implies that  
 670 this model becomes additive such that:

$$\begin{aligned} \log s(\mathbf{x}) &= \log b(\mathbf{x}) + \log \left( o(\mathbf{x}) + \frac{\eta(\mathbf{x})}{b(\mathbf{x})} \right) , \\ &\approx \log b(\mathbf{x}) + \log \hat{o}(\mathbf{x}) , \end{aligned} \quad (12)$$

671 where  $\hat{o}(\mathbf{x})$  is the signal only degraded by noise. Sled et al. (1998) shows that Eq.  
 672 (12) can be related to PDFs such that:

$$S(s) = B(s) * O(s) , \quad (13)$$

673 where  $S$ ,  $B$  and  $O$  are respectively the probability densities of  $s$ ,  $b$  and  $o$ .

674 Restoring the corrupted signal  $s$  is carried out by finding the multiplicative  
 675 field  $b$  which maximizes the frequency content of the distribution  $O$ . Sled et al.  
 676 (1998) argue that a search through all possible fields  $b$  and selection of the one  
 677 which maximizes the high frequency content of  $O$  could be carried out but results  
 678 in an exhaustive search. However, they show that the bias field distribution can  
 679 be assimilated to a near Gaussian distribution. Using this fact as *a priori*, it is  
 680 then possible to infer the distribution  $O$  using Wiener deconvolution given  $B$  and  
 681  $S$  and later estimate the corresponding smooth field  $b$ .

682 Lv et al. (2009) corrected the inhomogeneity in T<sub>2</sub>-W-MRI images by using  
 683 the method proposed by Madabhushi et al. (2006). In this method, the MRI im-  
 684 ages are corrected iteratively by successively detecting the image foreground via

---

<sup>4</sup>The N3 algorithm implementation is available at: <http://www.bic.mni.mcgill.ca/software/N3/>

685 generalized scale ( $g$ -scale) and estimating a bias field function based on a second-  
686 order polynomial model. First the background of the MRI image is eliminated by  
687 thresholding. The threshold value is commonly equal to the mean SI of the consid-  
688 ered image. Then, in the seeded region growing algorithm is applied considering  
689 every thresholded pixel as a potential seed. However, pixels already assigned to  
690 a region will not be considered any more as seed. As in seeded region growing  
691 algorithm (Shapiro and Stockman (2001)), two criteria are taken into account to  
692 expand the region. First, the region will grow using a connected-neighbourhood,  
693 initially defined by the user. Then, the homogeneity of SI is based on a fuzzy  
694 membership function taking into account the absolute difference of the SIs of two  
695 pixels. Depending on the membership value (cf., a threshold has to be defined),  
696 the pixel considered is merged or not to the region. Once this segmentation is  
697 performed, the largest region  $R$  is used as a mask to select pixels of the origi-  
698 nal image and the mean SI,  $\mu_R$ , is computed. The background variation  $b(\mathbf{x})$  is  
699 estimated as:

$$b(\mathbf{x}) = \frac{s(\mathbf{x})}{\mu_R}, \quad \forall \mathbf{x} \in R, \quad (14)$$

700 where  $s(\mathbf{x})$  is the original MRI image.

701 Finally, a second order polynomial  $\hat{b}_\Theta(\mathbf{x})$  is fitted in a least-squares sense (Eq.  
702 (15)),

$$\hat{\Theta} = \arg \min_{\Theta} |b(\mathbf{x}) - \hat{b}_\Theta(\mathbf{x})|^2, \quad \forall \mathbf{x} \in R. \quad (15)$$

703 Finally, the whole original MRI image is corrected by dividing it by the es-  
704 timated bias field function  $\hat{b}_\Theta(\mathbf{x})$ . This process is repeated until the number of  
705 pixels in the largest region  $R$  does not change significantly between two iterations.

#### 706 – ***SI normalization/standardization:***

707 As discussed in the later section, segmentation or classification tasks are usu-  
708 ally performed by first learning from a training set of patients. Hence, one can  
709 emphasize the desire to perform MRI examinations with a high repeatability or  
710 in other words, one would ensure to obtain similar MRI images (cf., similar SIs)  
711 for patients of the same group (cf., healthy patients *vs.* patients with CaP), for a  
712 similar sequence.

713 However, it is a known fact that variability between patients occurs during the  
714 MRI examinations even using the same scanner, protocol or sequence parameters  
715 (Nyul and Udupa (1999)). Hence, the aim of normalization or standardization

of the MRI data is to remove the variability between patients and enforce the repeatability of the MRI examinations.

Approaches used to standardize MRI images can be either categorized as statistical-based standardization or organ SI-based standardization.

Artan et al. (2010, 2009) as well as Ozer et al. (2009, 2010) standardized T<sub>2</sub>-W, DCE and DW MRI images by computing the *standard score* (also called *z-score*) of the pixels of the PZ as:

$$I_s(\mathbf{x}) = \frac{I_r(\mathbf{x}) - \mu_{pz}}{\sigma_{pz}}, \quad \forall \mathbf{x} \in \text{PZ}, \quad (16)$$

where  $I_s(\mathbf{x})$  is the standardized SI with the image coordinates  $\mathbf{x} = \{x, y\}$ ,  $I_r(\mathbf{x})$  is the raw SI,  $\mu_{pz}$  is the mean-SI of the PZ and  $\sigma_{pz}$  is the SI standard deviation in the PZ.

This transformation enforces the image PDF to have a zero mean and a unit standard deviation. In a similar way, Liu et al. (2013) normalized T<sub>2</sub>-W-MRI by making use of the median and interquartile range for all the pixels.

Lv et al. (2009) scaled the SI of T<sub>2</sub>-W-MRI images using the method proposed by Nyul et al. (2000) based on PDF matching. This approach is based on the assumption that MRI images from the same sequence should share the same PDF appearance. Hence, one can approach this issue by transforming and matching the PDFs using some statistical landmarks such as median and different quantiles. Using a training set, these statistical landmarks are extracted for  $N$  training images as for instance for the minimum, the 25<sup>th</sup> quantile, the median, the 75<sup>th</sup> quantile and the maximum:

$$\begin{aligned} \Phi_0 &= \{\phi_0^1, \phi_0^2, \dots, \phi_0^N\}, \\ \Phi_{25} &= \{\phi_{25}^1, \phi_{25}^2, \dots, \phi_{25}^N\}, \\ \Phi_{50} &= \{\phi_{50}^1, \phi_{50}^2, \dots, \phi_{50}^N\}, \\ \Phi_{75} &= \{\phi_{75}^1, \phi_{75}^2, \dots, \phi_{75}^N\}, \\ \Phi_{100} &= \{\phi_{100}^1, \phi_{100}^2, \dots, \phi_{100}^N\}, \end{aligned} \quad (17)$$

where  $\phi_{n^{\text{th}}}^{i^{\text{th}}}$  is the  $n^{\text{th}}$  quantile of the  $i^{\text{th}}$  training image.

Then, the mean of each quantile  $\{\bar{\Phi}_0, \bar{\Phi}_{25}, \bar{\Phi}_{50}, \bar{\Phi}_{75}, \bar{\Phi}_{100}\}$  is also calculated. Once this training stage is performed, a linear transformation by parts  $\mathcal{T}(\cdot)$  can be computed (Eq. (18)) for each test image  $t$  by mapping each statistical landmark  $\varphi_{(\text{cdot})}^t$  of this image with the pre-learned statistical landmarks  $\bar{\Phi}_{(\cdot)}$ . This linear

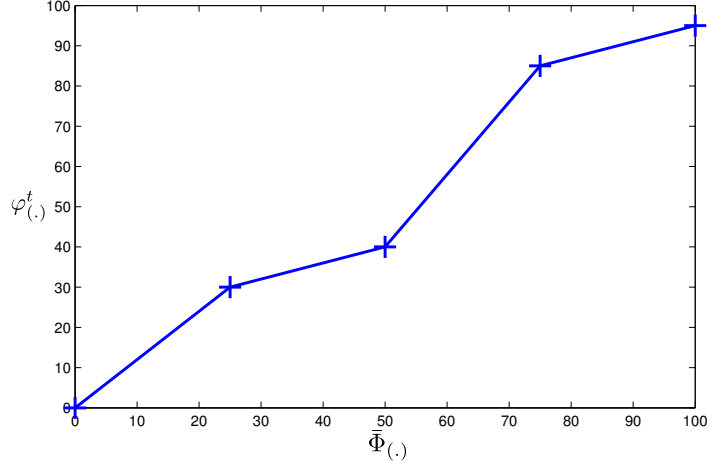


Figure 9: Example of linear mapping by parts as proposed by Nyul et al. (2000).

mapping is also depicted in Fig. 9.

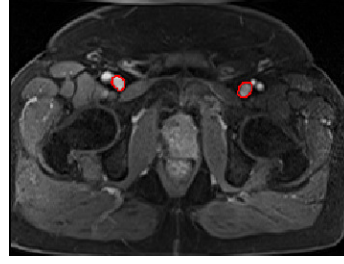
$$\mathcal{T}(s(\mathbf{x})) = \begin{cases} \lceil \bar{\Phi}_0 + (s(\mathbf{x}) - \varphi_0^t) \left( \frac{\bar{\Phi}_{25} - \bar{\Phi}_0}{\varphi_{25}^t - \varphi_0^t} \right) \rceil, & \text{if } \varphi_0^t \leq s(\mathbf{x}) < \varphi_{25}^t, \\ \lceil \bar{\Phi}_{25} + (s(\mathbf{x}) - \varphi_{25}^t) \left( \frac{\bar{\Phi}_{50} - \bar{\Phi}_{25}}{\varphi_{50}^t - \varphi_{25}^t} \right) \rceil, & \text{if } \varphi_{25}^t \leq s(\mathbf{x}) < \varphi_{50}^t, \\ \lceil \bar{\Phi}_{50} + (s(\mathbf{x}) - \varphi_{50}^t) \left( \frac{\bar{\Phi}_{75} - \bar{\Phi}_{50}}{\varphi_{75}^t - \varphi_{50}^t} \right) \rceil, & \text{if } \varphi_{50}^t \leq s(\mathbf{x}) < \varphi_{75}^t, \\ \lceil \bar{\Phi}_{75} + (s(\mathbf{x}) - \varphi_{75}^t) \left( \frac{\bar{\Phi}_{100} - \bar{\Phi}_{75}}{\varphi_{100}^t - \varphi_{75}^t} \right) \rceil, & \text{if } \varphi_{75}^t \leq s(\mathbf{x}) \leq \varphi_{100}^t, \end{cases} \quad (18)$$

Viswanath et al. (2011, 2009, 2012) use a variant of this previous approach presented in the work of Madabhushi and Udupa (2006) aiming to standardize the T<sub>2</sub>-W-MRI images. Instead of computing the PDF of an entire image, a pre-segmentation of the foreground is carried out via *g*-scale which was discussed in the bias correction section. Once the foreground is detected, the largest region is extracted and the same process than previously mentioned (see Eq. (18)) takes place in order to align PDFs of the foreground of the MRI images.

The methods described above were statistical-based methods. However, the standardization problem can be tackled by normalizing the MRI images using the SI of some known organs present in these images. Niaf et al. (2012, 2011) normalized T<sub>2</sub>-W-MRI images by dividing the original SI of the images by the mean SI of the bladder (see Fig. 10(a)). Likewise, Niaf et al. (2011) standardized the T<sub>1</sub>-W-MRI images using the arterial input function (AIF). They computed the AIF by taking the mean of the SI in the most enhanced part of the common



(a) Illustration and location of the bladder on a T<sub>2</sub>-W-MRI image acquired with a 3.0 Tesla MRI scanner



(b) Illustration and location of the femoral arteries on a T<sub>1</sub>-W-MRI image acquired with a 3.0 Tesla MRI scanner

Figure 10: Illustration of the two organs used by Niaf et al. (2012, 2011) to normalize T<sub>2</sub>-W and T<sub>1</sub>-W MRI images.

femoral arteries (see Fig. 10(b)) as proposed by Wiart et al. (2007).

### 3.1.2. MRSI spectra

Presented in Sect. 2.3.2, MRSI is a modality related to a one dimensional signal. Hence, specific pre-processing steps for this type of signals have been applied instead of standard signal processing methods.

— **Phase correction:** MRSI data acquired suffer from zero-order and first-order phase misalignments as shown in Fig. 11 (Chen et al. (2002), Osorio-Garcia et al. (2012)).

Parfait et al. (2012) used a method proposed by Chen et al. (2002) where the phase of MRSI signal is corrected based on entropy minimization in the frequency domain. The corrected MRSI signal  $o(\xi)$  can be expressed as:

$$\begin{aligned}\Re(o(\xi)) &= \Re(s(\xi)) \cos(\Phi(\xi)) - \Im(\xi) \sin(\Phi(\xi)) , \\ \Im(o(\xi)) &= \Im(s(\xi)) \cos(\Phi(\xi)) + \Re(\xi) \sin(\Phi(\xi)) , \\ \Phi(\xi) &= \phi_0 + \phi_1 \frac{\xi}{N} ,\end{aligned}\tag{19}$$

where  $\Re(\cdot)$  and  $\Im(\cdot)$  are the real and imaginary part of the complex signal respectively,  $s(\xi)$  is the corrupted MRSI signal,  $\phi_0$  and  $\phi_1$  are the zero-order and first-order phase correction terms respectively and  $N$  is the total number of samples of the MRSI signal.



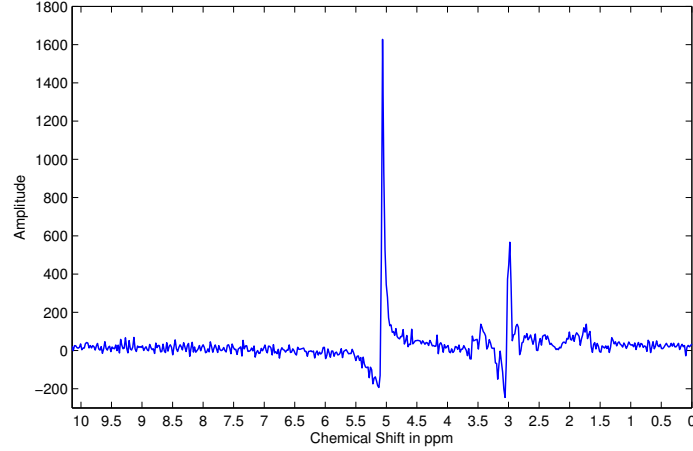


Figure 11: Illustration of phase misalignment in an MRSI spectra acquire with a 3.0 Tesla MRSI scanner. Note the distortion of the signal specially visible for the water and citrate peaks.

772        Chen et al. (2002) tackled this problem using an optimization framework where  
 773         $\phi_0$  and  $\phi_1$  had to be inferred. Hence, the simplex Nelder-Mead optimization  
 774        method was used to minimize the following cost function based on the *Shannon*  
 775        *entropy* formulation:

$$\hat{\Phi} = \arg \min_{\Phi} \left[ - \sum \Re(s'(\xi)) \ln \Re(s'(\xi)) + \lambda \|\Re(s(\xi))\|_2 \right] , \quad (20)$$

776        where  $s'(\xi)$  is the first derivative of the corrupted signal  $s(\xi)$  and  $\lambda$  is a regular-  
 777        ization parameter.

778        Once the best parameter  $\Phi$  is obtained, the MRSI signal is corrected using Eq.  
 779        (19).

780    — **Water and lipid residuals filtering:** The water and lipid metabolites occur  
 781    in much higher concentrations the metabolites of interests (cf., choline, creatine  
 782    and citrate) (Osorio-Garcia et al. (2012), Zhu et al. (2010)). Fortunately, specific  
 783    MRSI sequences were developed in order to suppress water and lipid metabolites  
 784    using pre-saturation techniques (Zhu et al. (2010)). However, these techniques do  
 785    not perfectly remove water and lipids peaks and some residuals are still present  
 786    in the MRSI spectra as shown in Fig. 12. Therefore, different post-processing  
 787    methods have been proposed to enhance the quality of the MRSI spectra by  
 788    removing these residuals.

789        Kelm et al. (2007) used the well known HSVD algorithm proposed by Pijnappel

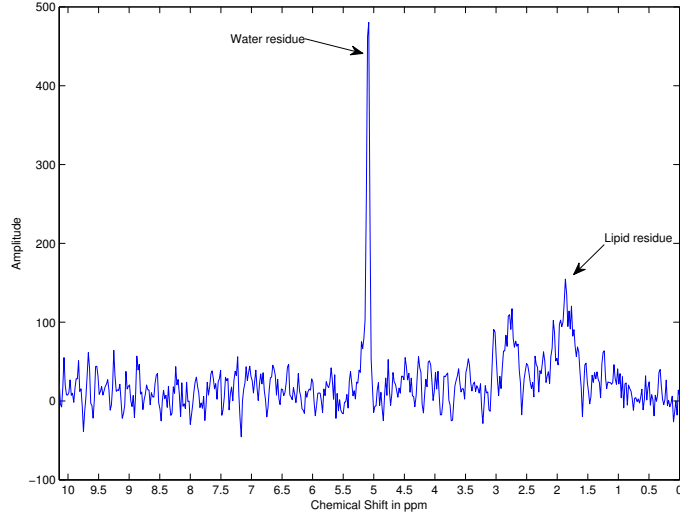


Figure 12: Illustration of the residues of water and fat even after their suppression during the acquisition protocol. The acquisition was carried out with a 3.0 Tesla MRI.

et al. (1992). In the time domain, a MRSI signal  $s(t)$  is modelled by a sum of  $K$  exponentially damped sinusoids such that:

$$s(t) = \sum_{k=1}^K a_k \exp(i\phi_k) \exp(-d_k + i2\pi f_k)t + \eta(t) , \quad (21)$$

where  $a_k$  is the amplitude proportional to the metabolite concentration with a resonance frequency  $f_k$ ,  $d_k$  represents the damping factor of the exponential,  $\phi_k$  is the first-order phase and  $\eta(t)$  is a complex white noise.

Pijnappel et al. (1992) showed that the “noise-free signal” can be found using the singular value decomposition (SVD) decomposition. First the noisy signal is reorganized inside a Hankel matrix  $H$ . It can be shown that if the signal considered would be a “noise-free signal”, the rank of  $H$  would be equal to rank  $K$ . However, due to the presence of noise,  $H$  is in fact a full rank matrix. Thus, to recover the “noise-free signal”, the rank of  $H$  can be truncated to  $K$  using its SVD decomposition. Hence, knowing the cut off frequencies of water (cf., 4.7 ppm) and lipid (cf., 2.2 ppm) metabolites, their corresponding peaks can be reconstructed and subtracted from the original signal (Laudadio et al. (2002)).

— **Baseline correction:** Sometimes, the problem discussed in the above section

regarding the lipid molecules is not addressed simultaneously with water residuals suppression. Lipids and macromolecules are known to affect the baseline of the MRSI spectra. They could cause errors during further fitting processes aiming to quantify the metabolites, especially regarding the citrate metabolite.

Parfait et al. (2012) made the comparison of two different methods to detect the baseline and correct the MRSI spectra which are based on the work of Lieber and Mahadevan-Jansen (2003) and Devos et al. (2004). Lieber and Mahadevan-Jansen (2003) addressed the problem of baseline detection in the frequency domain by fitting a polynomial of low degree  $p(x)$  (e.g., second or third degree) to the MRSI signal  $s(x)$  in a least-squares sense. Then, the values of the fitted polynomial are re-assigned as:

$$p_f(x) = \begin{cases} p(x) , & \text{if } p(x) \leq s(x) , \\ s(x) , & \text{if } p(x) > s(x) . \end{cases} \quad (22)$$

Finally, this procedure of fitting and re-assignment is iteratively repeated on  $p_f(x)$  until a stopping criterion is reached. The final polynomial function can be subtracted from the original signal  $s(x)$  to correct it.

Parfait et al. (2012) modified this algorithm by convolving a Gaussian kernel to smooth the MRSI signal instead of fitting a polynomial function, keeping the rest of the algorithm identical.

Unlike Lieber and Mahadevan-Jansen (2003), Devos et al. (2004) proposed to correct the baseline in the time domain by multiplying the MRSI signal by a decreasing exponential function as:

$$c(t) = \exp(-\beta t) , \quad (23)$$

Having a typical value for  $\beta$  of 0.15.

However, Parfait et al. (2012) concluded that the method proposed by Lieber and Mahadevan-Jansen (2003) outperforms the one of Devos et al. (2004). In the contemporary work of Tiwari et al. (2012), the authors detected the baseline using a local non-linear fitting method avoiding regions with significant peaks which were detected using a experimentally parametrised signal-to-noise ratio (i.e. a value larger than 5 dB).

- **Frequency alignment:** Due to variations of the experimental conditions, a frequency shift can be observed in the MRSI spectra as shown in Fig. 13 (Chen et al. (2002), Osorio-Garcia et al. (2012)).

Tiwari et al. (2012) correct the frequency shift by first detecting known metabolite peaks such as choline, creatine and citrate. The frequency shift is corrected by

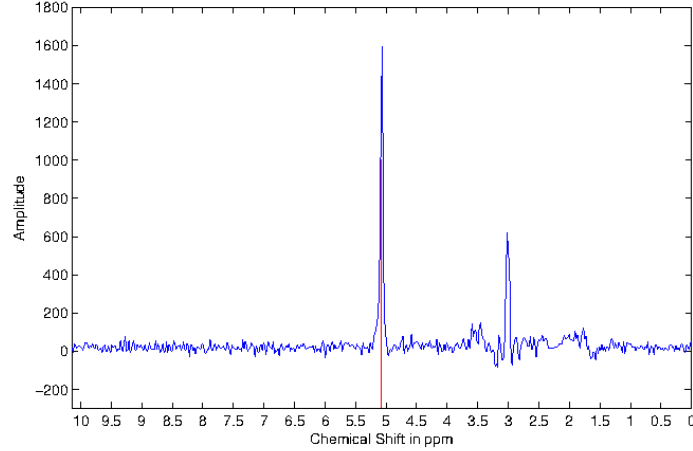


Figure 13: Illustration of frequency misalignment in an MRSI spectra acquired with a 3.0 Tesla MRSI scanner. The water peak is known to be aligned at 4.65 ppm. However, it can be seen that the peak on this spectra is aligned at around 5.1 ppm.

837 minimizing the frequency error between the experimental and theoretical values  
838 of each of these peaks.

839 – **Normalization:** Due to variations of the experimental conditions, the MRSI  
840 signal may also vary between patients.

841 Parfait et al. (2012) as Devos et al. (2004) compared two methods to nor-  
842 malize MRSI signal. In each method, the original MRSI spectra is divided by a  
843 normalization factor, similar to the intensity normalization described earlier.

844 The first approach to obtain the normalization factor is based on an estimation  
845 of the water concentration. It is required to have an additional MRSI sequence  
846 where the water metabolites are unsuppressed. Using this sequence, an estimation  
847 of the water concentration can be performed using the previously reported HSVD  
848 algorithm. The second approach to normalization is based on using the  $L_2$  norm  
849 of the MRSI spectra  $\|s(\xi)\|_2$ . It should be noted that both Parfait et al. (2012)  
850 and Devos et al. (2004) concluded that the  $L_2$  normalization was more efficient in  
851 their framework.

### 852 3.2. Segmentation

853 The segmentation task consists in delineating the prostate boundaries in the MRI.  
854 This procedure is of particular importance for focusing the posterior processing on the  
855 organ of interest (Ghose et al. (2012)). In this section, only the segmentation methods

Table 4: Overview of the segmentation methods used in CAD systems.

Segmentation methods	References
<i>MRI-based segmentation:</i>	
Manual segmentation	[4-5,16,18-21,24,38-40]
Region-based segmentation	[11]
Model-based segmentation	[10,34-36,41]
<i>MRSI-based segmentation:</i>	
Clustering	[28]

used in CAD systems are presented and summarized in Tab. 4. An exhaustive review of prostate segmentation methods in MRI can be found in Ghose et al. (2012).

### 3.2.1. MRI-based segmentation

— **Manual segmentation:** To highlight the importance of prostate segmentation task in CAD systems, it is interesting to note the large number of studies which segment manually the prostate organs (Artan et al. (2010, 2009), Matulewicz et al. (2013), Niaf et al. (2012, 2011), Ozer et al. (2009, 2010), Puech et al. (2009), Vos et al. (2008a,b)). In all the cases, the boundaries of the prostate gland is defined in order to limit the further processing to only this area. This approach ensure the right delineation of the organ nevertheless this procedure is highly time consuming and should be perform by a radiologist.

— **Region-based segmentation:** Litjens et al. (2012b) used a multi-atlas-based segmentation using multi-modal images (e.g., T<sub>2</sub>-W-MRI and ADC map) to segment the prostate with an additional pattern recognition method to differentiate CG and PZ as proposed in Litjens et al. (2012a). This method consists of three different steps: (i) the registration between each atlas and the multi-modal images, (ii) the atlas selection and finally (iii) the classification of the prostate segmented voxels in either CG or PZ.

The registration between each atlas and the MRI images is performed using two successive registrations: the first registration is a rigid registration to roughly align the atlases and the MRI images and the second is an elastic registration using B-spline transformation. The objective function to perform the registration is defined as the weighted sum of the metric of both T<sub>2</sub>-W-MRI and ADC map. The metric is based on mutual information (MI). We refer to the next section

for more details in regard to registration. Two strategies of atlas selection were performed by using either a majority voting approach or the simultaneous truth and performance level estimation (STAPLE) approach (Warfield et al. (2004)).

Subsequently, CG and PZ segmentation within the prostate region is achieved by classifying each voxel using a linear discriminant analysis (LDA) classifier. Three types of features were considered: (i) anatomy, (ii) intensity and (iii) texture. Regarding the anatomy, relative position and relative distance from the pixel to the border of the prostate were used. The intensity features consist of the intensity of the voxel in the ADC coefficient and the  $T_2$  map. The texture features were composed of five different features: homogeneity, correlation (Amadasun and King (1989)), entropy, texture strength (Li et al. (2005)) and local binary pattern (LBP) (Ojala et al. (1996)). Finally, morphological operations were applied to remove artefacts and the contours between the zones were smoothed using thin plate spline (TPS) (Bookstein (1989)).

- **Model-based segmentation:** Viswanath et al. (2008a, 2009) used the multi-attribute non-initializing texture reconstruction based active shape model (MANTRA) method as proposed by Toth et al. (2008). MANTRA is closely related to the active shape model (ASM) from Cootes et al. (1995). This algorithm consists of two stages: (i) a training stage where a shape and appearance model is generated and (ii) the actual segmentation performed based on the learned model.

For the training stage, a set of landmarks is defined and the shape model is generated as in the original ASM method (Cootes et al. (1995)). Then, to model the appearance, a set of  $K$  texture images  $\{I_1, I_2, \dots, I_k\}$  based on first and second order statistical texture features are computed. For a given landmark  $l$  with its given neighbourhood  $\mathcal{N}(l)$ , its feature matrix extracted can be expressed as:

$$f_l = \{I_1(\mathcal{N}(l)), I_2(\mathcal{N}(l)), \dots, I_k(\mathcal{N}(l))\}, \quad (24)$$

where  $I_k(\mathcal{N}(l))$  represents a feature vector obtained by sampling the  $k^{\text{th}}$  texture map using the neighbourhood  $\mathcal{N}(l)$ .

By generating multiple landmarks in the same fashion as ASM, principal components analysis (PCA) (Pearson (1901)) is applied to learn the appearance variations.

For the segmentation stage, the mean shape learned previously is initialised in the test image. The same associated texture images as in the training stage are computed. For each landmark  $l$ , a neighbourhood of patches are used to sample the texture images and a reconstruction is obtained using the appearance model

915 previously trained. The new landmark location will be defined as the position  
916 where the MI is maximal between the reconstructed and original values. This  
917 scheme is performed in a multi-resolution manner as in Cootes et al. (1995).

918 Subsequently, the same authors (Viswanath et al. (2012)) used the weighted  
919 ensemble of regional image textures for active shape model segmentation (WERITAS)  
920 method also proposed by Toth et al. (2009). As with the MANTRA method,  
921 WERITAS is based on the ASM formulation. In fact it is very close to the  
922 MANTRA itself. The same texture features are used to construct the appearance  
923 models, but instead of using MI between the landmarks and neighbour patches  
924 for adapting the landmark positions, it defines a metric based on the Mahalanobis  
925 distance. In the training stage, the Mahalanobis distance is computed between  
926 landmarks and neighbour patches for each of the features. Subsequently, a new  
927 metric is proposed as a linear weighted combination of those Mahalanobis dis-  
928 tances which maximises the correlation with the Euclidean distance between the  
929 patches and the true landmarks. In the segmentation step, this metric is then  
930 computed between the initialised landmarks and neighbouring patches in order  
931 to update landmark positions, in a similar fashion to other active contour model  
932 (ACM) models.

933 Litjens et al. (2011) and Vos et al. (2012) used an approach proposed by  
934 Huisman et al. (2010) in which the bladder, prostate and rectum are segmented  
935 tackling the segmentation task as an optimization problem. A probabilistic model  
936 is first trained by embedding the three following aspects: (i) the shape by defining  
937 each organ as an ellipse, (ii) the position by defining the distance and the angle  
938 between each organ center and (iii) the appearance using the PDFs of SI of each  
939 organ. Litjens et al. (2011) used only ADC map to encode the appearance whereas  
940 Vos et al. (2012) used both ADC and  $T_2$  maps. Then, during the optimization  
941 using a quasi-Newton optimizer, an objective function is minimized. This function  
942 is defined as the sum of the deviations from the above model learnt. This rough  
943 segmentation is then used inside a Bayesian framework to refine the segmentation.

### 944 3.2.2. MRSI-based segmentation

945 Tiwari et al. (2009a) localized the voxels corresponding to the prostate organ  
946 using a hierarchical spectral clustering. First, each MRSI spectrum is projected  
947 into a lower dimension space using graph embedding (Shi and Malik (2000)). To  
948 proceed, a similarity matrix  $W$  is computed using a Gaussian similarity measure

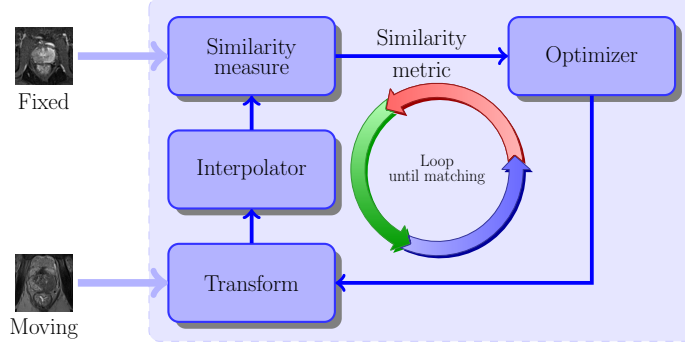


Figure 14: Typical framework involved to solve the registration problem.

949 from the Euclidean distance (Belkin and Niyogi (2001)) such that:

$$W(\mathbf{x}, \mathbf{y}) = \begin{cases} \exp\left(\frac{\|s(\mathbf{x}) - s(\mathbf{y})\|_2^2}{\sigma^2}\right) & , \text{ if } \|\mathbf{x} - \mathbf{y}\|_2 < \epsilon , \\ 0 & , \text{ if } \|\mathbf{x} - \mathbf{y}\|_2 > \epsilon , \end{cases} \quad (25)$$

950 where  $s(\mathbf{x})$  and  $s(\mathbf{y})$  are the MRSI spectra for the voxels  $\mathbf{x}$  and  $\mathbf{y}$  respectively,  $\sigma$  is  
 951 the standard deviation of the Gaussian similarity measure and  $\epsilon$  is a parameter used  
 952 to define an  $\epsilon$ -neighbourhood.

953 The MRSI spectra projection into the lower dimension space is approached as  
 954 a generalized eigenvector problem. Subsequently, a replicate k-means clustering  
 955 method is run defining two clusters. The data corresponding to larger cluster is  
 956 assumed to belong to the non-prostate voxels and these voxels will be eliminated  
 957 from the processing. The full procedure is repeated until the total number of voxels  
 958 left is inferior to a given threshold set experimentally.

### 959 3.3. Registration

960 The role of image registration is vital in CAD systems using multi-parametric  
 961 MRI images. As it will be discussed in Sect. 4, for the sake of an optimal classi-  
 962 fication, the features detected in each modality will be grouped depending of their  
 963 spatial locations. Hence, one has to ensure the perfect alignment of the multi-modal  
 964 MRI images ahead of performing any classification scheme.

965 Image registration is the procedure consisting of aligning an unregistered image  
 966 (also called moving image) into a template image (also called fixed image) via a  
 967 geometric transformation. This problem is usually addressed as presented in Fig. 14.  
 968 An iterative procedure takes place to infer the geometric transformation (parametric



Table 5: Classification of the different registration methods used in the CAD systems reviewed. Acronyms: gradient descent (GD), Nelder-Mead (NM).

Study index	Modality registered	Type	Geometric transform			Similarity measure			Optimizer		
			Rigid	Affine	Elastic	MSE	MI	CMI	GD	L-BFGS-B	NM simplex
[1-2]	T <sub>2</sub> -W - DCE	2D	—	✓	—	✓	—	—	—	—	—
[7]	T <sub>2</sub> -W - DW	2D	—	✓	✓	—	—	—	—	—	—
[7]	T <sub>2</sub> -W - DCE	2D	—	✓	✓	—	✓	—	✓	—	—
[34-35]	T <sub>2</sub> -W - DCE	2D	—	✓	—	—	✓	—	—	—	—
[36]	T <sub>2</sub> -W - DCE - DW	3D	—	✓	—	—	—	✓	✓	—	—
[38]	T <sub>2</sub> -W - DCE	3D	—	✓	—	—	✓	—	—	—	—
[40]	T <sub>2</sub> -W - DCE	3D	—	✓	✓	—	✓	—	—	✓	—

Notes:

—: not used or not mentioned.

✓: used or implemented.

or non-parametric) via an optimizer, which maximizes the similarity between the two images.

From Sect. 3.3.1 to 3.3.4, we individually review the different components of a typical registration framework (Fig 14). Section 3.3.5 will summarize the combinations of these components especially for the frameworks used in CAD systems. Exhaustive reviews covering all registration methods in computer science and medical fields can be found in Maintz and Viergever (1998) and Zitová and Flusser (2003).

### 3.3.1. Geometric transformation models

As previously mentioned, the registration problem is to align two images or volumes by finding the geometric transformation. Regarding the transformation, from all CAD systems reviewed, only parametric methods have been implemented.

Three different groups of parametric transformation models have been used, each of them are characterized by the degree of freedom that they offer.

The first type of transformation is usually referred to as rigid transformation. These transformations are only composed of rotation and translation transforms. Hence, for a 2D space where  $\mathbf{x} = (x, y) \in \mathbb{R}^2$  a rigid transformation  $\mathcal{T}_R$  is formalized as as:

$$\begin{aligned}
\mathcal{T}_R(\mathbf{x}) &= \begin{bmatrix} R & \mathbf{t} \\ \mathbf{0}^T & 1 \end{bmatrix} \mathbf{x} , \\
&= \begin{bmatrix} \cos \theta & -\sin \theta & t_x \\ \sin \theta & \cos \theta & t_y \\ 0 & 0 & 1 \end{bmatrix} \begin{bmatrix} x \\ y \\ 1 \end{bmatrix} , \tag{26}
\end{aligned}$$

where  $\theta$  is the rotation angle and  $\{t_x, t_y\}$  represents the translation along  $\{x, y\}$  respectively.

In the case of 3D registration using volume, an additional component  $z$  has to be taken into account such that  $\mathbf{x} = (x, y, z)$ . Thus, the rotation matrix  $\mathbf{R}$  becomes of size  $3 \times 3$  whereas the translation vector  $\mathbf{t}$  consists of a vector of three elements. Hence, the geometric transformation  $\mathcal{T}_R(\cdot)$  is embedded into a matrix of size  $4 \times 4$ .

Affine transformations provide additional degrees of freedom managing rotations and translation as with the rigid transformations but also shearing and scaling. Hence, for a 2D space where  $\mathbf{x} = (x, y) \in \mathbb{R}^2$ , an affine transformation  $\mathcal{T}_A$  is formalized as:

$$\begin{aligned}
\mathcal{T}_A(\mathbf{x}) &= \begin{bmatrix} A & \mathbf{t} \\ \mathbf{0}^T & 1 \end{bmatrix} \mathbf{x} , \\
&= \begin{bmatrix} a_{11} & a_{12} & t_x \\ a_{21} & a_{22} & t_y \\ 0 & 0 & 1 \end{bmatrix} \begin{bmatrix} x \\ y \\ 1 \end{bmatrix} . \tag{27}
\end{aligned}$$

Hence the four parameters  $\{a_{11}, a_{12}, a_{21}, a_{22}\}$  of the affine matrix and  $\{t_x, t_y\}$  of the translation encode an affine transformation.

Regarding volume registered, the same remark as previously mentioned can be applied in this case. Thus the geometric transformation  $\mathcal{T}_A(\cdot)$  is of size  $4 \times 4$  with nine parameters involved.

Finally, the last group of transformations is known as elastic transformations and offer the advantage to handle local distortions. In the reviewed CAD systems, the radial basis functions are used to formalize the local distortions such as:

$$\mathcal{T}_E(\mathbf{x}) = \frac{a_{11}x - a_{12}y + t_x + \sum_i c_i g(\|\mathbf{x} - p_i\|)}{a_{21}x + a_{22}y + t_y + \sum_i c_i g(\|\mathbf{x} - p_i\|)} , \tag{28}$$

where  $\mathbf{x}$  are the control points in both images and  $g(\cdots)$  is the actual radial basis function.

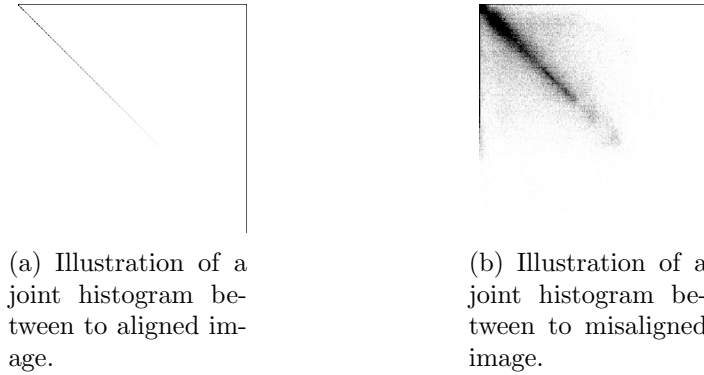


Figure 15: Difference observed in joint histogram between aligned and misaligned images. The joint measure will be more concentrated of the histogram in the case that the images are aligned and more randomly distributed in the case that both images are more misaligned.

Two radial basis functions are used: (i) the TPS and (ii) the B-splines. Apart from the formalism, these two approaches have a main difference. With B-splines, the control points are usually uniformly and densely placed on a grid where as with TPS, the control points correspond to detected or selected key points. By using TPS, Mitra et al. (2011) obtained more accurate and time efficient results than with the B-splines strategy (Mitra et al. (2012)).

It is reasonable to point out that usually only rigid or affine registrations are used to register multi-parametric images from a same protocol. Elastic registration methods are more commonly used to register multi-protocol images (e.g., histopathology with MRI images) (Toth et al. (2008, 2009)).

### 3.3.2. Similarity measure

During the registration procedure, a similarity criterion is computed in order to evaluate the quality of the alignment performed. Roughly speaking, this criterion will give the direction to take to the optimizer, in order to assign the most optimal values to the geometric transformation parameters.

The most naive similarity measure is the mean squared error (MSE) of the SI of MRI images. For a pair of images  $I$  and  $J$ , the MSE is formalized as:

$$\text{MSE} = \frac{1}{N} \sum_x \sum_y (I(x, y) - J(x, y))^2, \quad (29)$$

where  $N$  is the total number of pixels.

However, this metric is not well suited when multi-parametric images are involved due to the tissue appearance variations between the different modalities.

1026 In that regard, MI was introduced as a registration measure in the late 1990's by  
 1027 Pluim et al. (2003). The MI measure finds its foundation in the assumption that a  
 1028 homogeneous region in the first modality image should also appear as a homogeneous  
 1029 region in the second modality even if their SIs are not identical. Thus, those regions  
 1030 share information and the registration task can be achieved by maximizing this  
 1031 common information. Hence, MI of two images  $A$  and  $B$  is defined as:

$$MI(A; B) = S(A) + S(B) - S(A, B) , \quad (30)$$

1032 where  $S(A)$  and  $S(B)$  are the marginal entropies and  $S(A, B)$  is the joint entropy.

1033 Then, maximizing the MI is equivalent to minimizing the joint entropy. The joint  
 1034 entropy measure is related with the degree of uncertainty or dispersion of the data  
 1035 in the joint histogram of the images  $A$  and  $B$ . As shown in Fig. ??, the data in the  
 1036 joint histogram will be concentrated in the case of aligned images while will be more  
 1037 randomly distributed in the case of misaligned images. Regarding the computation  
 1038 of the entropies, an estimation of the PDFs have to be carried out. Histogram or  
 1039 Parzen window methods are a common way to estimate these PDFs.

1040 A generalized form of MI, CMI, was proposed by Chappelow et al. (2011). CMI  
 1041 encompasses interdependent information such as texture and gradient into the metric.  
 1042 Hence, for both of images  $A$  and  $B$ , the image ensembles  $\epsilon_n^A$  and  $\epsilon_m^B$  are generated  
 1043 and composed of  $n$  and  $m$  images based on the texture and gradient. Then, the CMI  
 1044 can be formulated such as:

$$CMI(\epsilon_n^A; \epsilon_m^B) = S(\epsilon_n^A) + S(\epsilon_m^B) - S(\epsilon_n^A, \epsilon_m^B) . \quad (31)$$

1045 From Eq. (31), it can be seen that CMI is estimated using high dimensional data  
 1046 and that histogram-based methods to estimate the PDFs are not suitable any more  
 1047 (Chappelow et al. (2011)). However, other approaches can be used such as the one  
 1048 employed by Staring et al. (2009) to compute the  $\alpha$ -MI (Hero et al. (2002)) which  
 1049 is based on the construction of entropic graphs using  $k$ -nearest neighbour ( $k$ -NN)  
 1050 inside the high dimensional feature space later used to estimate the MI.

### 1051 3.3.3. Optimization methods

1052 Registration is usually regarded as an optimization problem where the parame-  
 1053 ters of the geometric transformation model have to be inferred by minimizing the  
 1054 similarity measure. Iterative estimation methods are commonly used: Nelder-Mead  
 1055 simplex method (Nelder and Mead (1965)), L-BFGS-B quasi-Newton method (Byrd  
 1056 et al. (1995)) and gradient descent (Viola and Wells (1997)). During our review, we  
 1057 noticed that authors do not usually linger over optimizer choice.

#### 1058 3.3.4. Interpolation

1059 The registration procedure involves transforming an image, and pixels mapped  
1060 to non-integer points must be approximated using interpolation methods. As for the  
1061 optimization methods, we notice that little attention has been paid on the choice  
1062 of those interpolations methods. However, commonly used methods are bilinear,  
1063 nearest-neighbour, bi-cubic, spline and inverse-distance weighting method (Mitra  
1064 (2012)).

#### 1065 3.3.5. Review of the methods used in CAD system

1066 Studies presenting CAD pipeline incorporating an automatic registration proce-  
1067 dure are summarized in Tab. 5.

1068 Ampeliotis et al. (2007, 2008) did not use the framework as presented in Fig.  
1069 14 to register 2D T<sub>2</sub>-W and DCE images. By using image symmetries and the  
1070 MSE metric, they find the parameters of an affine transformation but not using a  
1071 common objective function. They are finding independently and consecutively the  
1072 scale factor, the rotation and finally the translation.

1073 Giannini et al. (2013) used also a in-house development registration method to  
1074 register 2D T<sub>2</sub>-W and DW images. To register both images using an affine transfor-  
1075 mation model, the bladder is first segmented in both modalities in order to obtain  
1076 its contours.

1077 Giannini et al. (2013) and also Vos et al. (2010) used the same framework (Rueck-  
1078 ert et al. (1999)) which is based on finding an affine transformation to register the  
1079 T<sub>2</sub>-W and DCE images using MI. Then, an elastic registration using B-spline takes  
1080 place using the affine parameters to initialize the geometric model with the same sim-  
1081 ilarity measure. However, the approaches differ regarding the choice of the optimizer  
1082 since Giannini et al. (2013) used a gradient descent and Vos et al. (2010) tackle the  
1083 optimization via a quasi-Newton method. Moreover, Giannini et al. (2013) performed  
1084 a 2D registration whereas Vos et al. (2010) registered 3D volumes.

1085 Viswanath et al. (2008a, 2009) as well as Vos et al. (2008a) performed an affine  
1086 registration using the MI as similarity measure to correct the misalignment between  
1087 T<sub>2</sub>-W and DCE images. The choice of the optimizer was not specified. Viswanath  
1088 et al. (2008a, 2009) focused on 2D registration while Vos et al. (2008a) performed  
1089 3D registration.

1090 Finally, Viswanath et al. (2011) performed a 3D registration with the three modal-  
1091 ities, T<sub>2</sub>-W and DCE and DW MRI, by using an affine transformation model com-  
1092 bined with the CMI similarity measure as presented in Chappelow et al. (2011).  
1093 Moreover, Chappelow et al. (2011) employed gradient descent to solve this problem  
1094 but suggested Nelder-Mead simplex and quasi-Newton method as other solutions.

Table 6: Overview of the CADe strategies employed in CAD systems.

CADe: ROIs selection strategy	References
All voxels-based approach	[4-5,7-8,12,14,16-17,20-22,25-37]
Lesions candidate detection	[10-11,41]

## 4. Image classification framework

### 4.1. CADe: ROIs detection/selection

As discussed in the introduction and shown in Fig. 2.3.2, the image classification framework is composed of eventually a CADe and a CADx. In this section, we will focus on studies embedding a CADe in their framework. Two approaches are considered to define a CADe (see Tab. 6): (i) voxel-based delineation and (ii) lesion segmentation.

The first strategy, which concerns the majority of the studies reviewed (see Tab. 6), is in fact linked to the nature of the classification framework. All voxels are considered as a possible threat and the output of the framework will be the lesions classified as cancerous.

The secondary group of methods is composed of method implementing a lesion segmentation algorithm to delineate potential candidates to further obtain a diagnosis through the CADx. This approach was borrowed from methodologies applied successfully in CADe for breast cancers.

Vos et al. (2012) highlighted lesion candidates by detecting blobs in the ADC map. These candidates were filter using some *a priori* criteria such as SI or diameter. As mentioned in Sect. 2.3.2 (see also Tab. 2.3.2), CaP can be interpreted as region of lower SI in ADC map. Hence, blob detectors are suitable to highlight these regions. Blobs are detected in a multi-resolution scheme by computing the three main eigenvalues  $\{\lambda_{\sigma,1}, \lambda_{\sigma,2}, \lambda_{\sigma,3}\}$  of the Hessian matrix for each voxel location of the ADC map at a specific scale  $\sigma$  as proposed by Li et al. (2003). The probability  $p$  of a voxel  $\mathbf{x}$  being a part of a blob at the scale  $\sigma$  is given by:

$$P(\mathbf{x}, \sigma) = \begin{cases} \frac{\|\lambda_{\sigma,3}(\mathbf{x})\|^2}{\|\lambda_{\sigma,1}(\mathbf{x})\|} , & \text{if } \lambda_{\sigma,k}(\mathbf{x}) > 0 \text{ with } k = \{1, 2, 3\} , \\ 0 , & \text{otherwise .} \end{cases} \quad (32)$$

1118 The fusion of the different scales is computed as:

$$L(\mathbf{x}) = \max P(\mathbf{x}, \sigma), \forall \sigma . \quad (33)$$

1119 The resulting map  $L(\mathbf{x})$  is then filtered depending on its appearance (cf. maxi-  
1120 mum of the likelihood of the region, diameter of the lesion) and their SI in ADC and  
1121 T<sub>2</sub>-W images. The detected regions are then used as inputs for the CADx.

1122 Litjens et al. (2011) used a pattern recognition approach in order to delineate  
1123 the ROIs. A blobness map was calculated in the same manner as previously men-  
1124 tioned using the multi-resolution Hessian blob detector on the ADC map, T<sub>2</sub>-W and  
1125 pharmacokinetic parameters maps (see Sect. 4.2 for details about those parameters).  
1126 Additionally, the position of the voxel  $\mathbf{x} = \{x, y, z\}$  was used as a feature as well as  
1127 the Euclidean distance of the voxel to the prostate center. Hence, the feature vectors  
1128 were composed of eight features and a support vector machines (SVM) classifier was  
1129 trained using a radial basis function (RBF) kernel (see Sect. 4.4 for more details).

1130 Subsequently, Litjens et al. (2012b) modified this approach by including only  
1131 features related to the blob detection on the different maps as well as the original  
1132 SIs of the parametric images. Two new maps were introduced based on texture.  
1133 Instead of a SVM classifier, a  $k$ -NN classifier was used. The candidate regions were  
1134 then extracted by performing a local maxima detection followed by post-processing  
1135 region-growing and morphological operations.

#### 1136 4.2. Feature detection

1137 Discriminative features which can be used to recognize CaP from healthy tissue  
1138 have to be first detected. This section will summarize the different strategies em-  
1139 ployed for this task. The feature type used is summarized in Tab. 7 while Tab. 8  
1140 sums up which strategies were used by the different studies reviewed.

Table 7: Overview of the feature detection methods used in CAD systems.

Feature detection methods	Indexes
<b>MRI image:</b>	
<i>Voxel-wise detection</i>	
Intensity-based	A
Edge-based	
Prewitt operator	B <sub>1</sub>
Sobel operator	B <sub>2</sub>
Kirsch operator	B <sub>3</sub>
Gabor filtering	B <sub>4</sub>
Texture-based	
Haralick features	C <sub>1</sub>
Fractal analysis	C <sub>2</sub>
Discrete cosine transform (DCT)	C <sub>3</sub>
Wavelet-based features	C <sub>4</sub>
Position-based	D
<i>Region-wise detection</i>	
Statistical-based	
Percentiles	E <sub>1</sub>
Statistical-moments	E <sub>2</sub>
Histogram-based	
PDF	F <sub>1</sub>
Histogram of oriented gradient (HOG)	F <sub>2</sub>
Shape context	F <sub>3</sub>
LBP	F <sub>4</sub>
Anatomical-based	G
<b>DCE signal:</b>	
Whole spectra approach	H
Semi-quantitative approach	I
Quantitative approach	
Toft model	J <sub>1</sub>
Brix model	J <sub>2</sub>
Weibull function	J <sub>3</sub>
Phenomenological universalities model	J <sub>4</sub>
<b>MRSI signal:</b>	
Whole spectra approach	K
Quantification approach	L
Wavelet-based approach	M



Table 8: Overview of the different features extracted by studies reviewed. The indexes of the features are presented in Tab. 7.

	A	B <sub>1</sub>	B <sub>2</sub>	B <sub>3</sub>	B <sub>4</sub>	C <sub>1</sub>	C <sub>2</sub>	C <sub>3</sub>	C <sub>4</sub>	D	E <sub>1</sub>	E <sub>2</sub>	F <sub>1</sub>	F <sub>2</sub>	F <sub>3</sub>	F <sub>4</sub>	G	H	I	J <sub>1</sub>	J <sub>2</sub>	J <sub>3</sub>	J <sub>4</sub>	K	L	M
[1]	△ --											△ --						✓								
[2]	△ --											△ --						✓								
[3]						△ --					-- ◇	-- ◇														
[4]	△ -- ◇																				✓!					
[5]	△ -- ◇																				✓!					
[6]	△ -- ◇							△ -- ◇		✓																
[7]	-- ◇																			✓		✓	✓			
[8]																								✓	✓	
[9]	△ -- ◇																			✓						
[10]	△ -- ◇									✓	△ • ◇	△ • ◇								✓						
[11]	△ -- ◇					△ • ◇				✓	△ • ◇	△ • ◇					✓			✓						
[12]	△ -- ◇																				✓					
[13]													△ • ◇	△ • ◇	△ • ◇	△ • ◇				✓!						
[14]							△ --																			
[15]							△ --																			
[16]																	✓								✓	
[17]																			✓	✓		✓	✓			
[18]	△ • ◇		△ • ◇	△ • ◇		△ • ◇					△ • ◇	△ • ◇							✓	✓						
[19]	△ • ◇		△ • ◇	△ • ◇		△ • ◇					△ • ◇	△ • ◇							✓	✓						
[20]	△ -- ◇																				✓!					
[21]	△ -- ◇																				✓!					
[22]																								✓	✓	
[23]										-- ◇	△ -- ◇									✓!						
[24]																			✓!							
[25]																			✓		✓					
[26]																								✓		
[27]																								✓		
[28]																								✓		
[29]		△ --	△ --	△ --		△ --						△ --												✓		
[30]		△ --	△ --	△ --		△ --						△ --												✓		
[31]					△ --																					✓
[32]		△ --	△ --	△ --		△ --						△ --												✓		
[33]		△ --	△ --	△ --	△ --	△ --						△ --												✓		
[34]																		✓								
[35]			△ --	△ --		△ --						△ --						✓								
[36]			△ --	△ --		△ • --						△ • --						✓								
[37]			△ --	△ --	△ --	△ --		△ --				△ --														
[38]	△ --																			✓						
[39]											-- • --									✓						
[40]											△ • --									✓						
[41]											△ • ◇									✓						

Notes:

△: implemented for T<sub>2</sub>-W-MRI images.

•: implemented for DCE-MRI images.

◇: implemented for DW-MRI images.

--: not used or not implemented.

✓: used or implemented.

✓!: partially implemented.

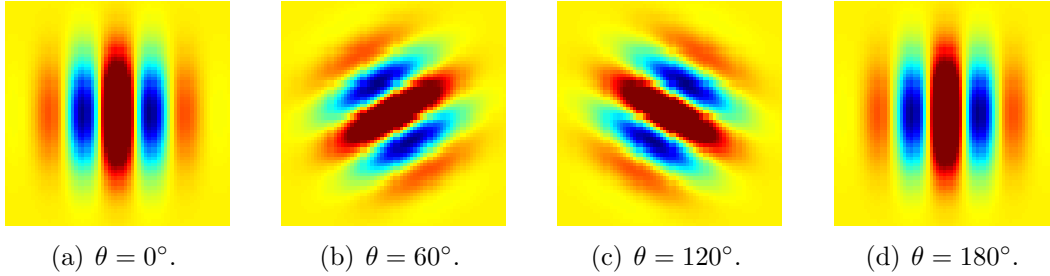


Figure 16: Illustration of four different Gabor filters varying their orientations  $\theta$ .

#### 4.2.1. Image-based features

This section will focus on image-based features detection. Two main strategies to detect features have been identified and used for the purpose of our classification: (i) voxel-wise detection and (ii) region-wise detection.

- **Voxel-wise detection:** This strategy refers to the fact that a feature is extracted at each voxel location of an image.

CaP as previously discussed (see Tab. 2.3.2) can be discerned due to SI changes. Hence, intensity-based features are one of the most common features used to build the feature vector which has to be classified (Ampeliotis et al. (2007, 2008), Artan et al. (2010, 2009), Chan et al. (2003), Langer et al. (2009), Liu et al. (2009), Niaf et al. (2012, 2011), Viswanath et al. (2011, 2008a)). This type of feature consists simply of the SI of each voxel of the different MRI modalities.

SI changes can be viewed as heterogeneous regions and edge-based features are used in that regard. Each feature is computed by convolving the original image with an edge operator. Three of these operators are used in CAD systems: (i) Prewitt operator (Prewitt (1970)), (ii) Sobel operator (Sobel (1970)) and (iii) Kirsch operator (Kirsch (1971)). Results obtained with these operators vary, due to their different kernels.

These features are commonly incorporated in the feature vector for further classification in the CAD systems reviewed (Niaf et al. (2012, 2011), Tiwari et al. (2013, 2010, 2009b), Viswanath et al. (2011, 2008b)).

Gabor filters offer another approach to extract information related to edges and texture and were found to perform similar processing to that in the human visual system (Daugman (1985), Gabor (1946)). A Gabor filter is defined by the modulation of a Gaussian function with a sinusoid which can be further rotated.

1167 Hence, a Gabor filter  $g$  can be formalized as:

$$g(x, y; \theta, \psi, \sigma, \gamma) = \exp\left(-\frac{x'^2 + \gamma^2 y'^2}{2\sigma^2}\right) \cos\left(2\pi\frac{x'}{\lambda} + \phi\right) , \quad (34)$$

1168 with

$$\begin{aligned} x' &= s(x \cos \theta + y \sin \theta) , \\ y' &= s(-x \sin \theta + y \cos \theta) , \end{aligned}$$

1169 where  $\lambda$  is the wavelength of the sinusoidal factor,  $\theta$  represents the orientation of  
1170 the Gabor filter,  $\psi$  is the phase offset,  $\sigma$  is the standard deviation of the Gaussian  
1171 envelope,  $\gamma$  is the spatial aspect ratio and  $s$  is the scale factor.

1172 To perform Gabor analysis to extract features for a classification scheme, a  
1173 bank of Gabor filters is usually created with different angles, scale and dilatations  
1174 (see Fig. 16) and then convolved with the image. Viswanath et al. (2008a, 2012)  
1175 and Tiwari et al. (2012) integrated Gabor analysis in their feature vector.

1176 Texture-based features provide other characteristics discerning CaP from healthy  
1177 tissue. The most common texture analysis for image classification was proposed  
1178 by Haralick et al. (1973) and is commonly used in CAD systems (Antic et al.  
1179 (2013), Niaf et al. (2012, 2011), Tiwari et al. (2013, 2010, 2009b), Viswanath  
1180 et al. (2011, 2008a,b, 2012)). At each voxel, a neighbourhood is defined around  
1181 this center and a gray-level co-occurrence matrix is built by selecting a pair of  
1182 voxels based on a defined distance and angle. Then, using this co-occurrence  
1183 matrix, a set of features can be computed based on the statistics describing the  
1184 texture around each voxel. Computation of these features is presented in Tab. 9.

1185 Fractal analysis and more precisely a local estimation of the fractal dimension  
1186 (Benassi et al. (1998)) describing the texture roughness at a specific location  
1187 was used in Lopes et al. (2011). A wavelet-based method in a multi-resolution  
1188 framework was used to estimate the fractal dimension. Cancerous tissue were  
1189 characterized to have a higher fractal dimension than healthy tissue.

1190 Chan et al. (2003) aimed to describe the texture using the frequency signature  
1191 via the discrete cosine transform (DCT) (Ahmed et al. (1974)) defining a neigh-  
1192 bourhood of  $7 \times 7$  pixels for each of the modalities that they used.. The DCT  
1193 allows to decompose a portion of image into a coefficients space where few of these  
1194 coefficients encoded the visually significant information. The DCT coefficients are

Table 9: The fourteen statistical features for texture analysis commonly computed from the gray level co-occurrence matrix  $p$  as presented by Haralick et al. (1973).

Statistical features	Formula
Angular second moment	$\sum_i \sum_j p(i, j)^2$ .
Contrast	$\sum_{n=0}^{N_g-1} n^2 \{ \sum_{i=1}^{N_g-1} \sum_{j=1}^{N_g-1} p(i, j) \} ,  i - j  = n$ .
Correlation	$\frac{\sum_i \sum_j (ij) p(i, j) - \mu_x \mu_y}{\sigma_x \sigma_y}$ .
Variance	$\sum_i \sum_j (i - \mu)^2 p(i, j)$ .
Inverse difference moment	$\sum_i \sum_j \frac{1}{1+(i-\mu)^2} p(i, j)$ .
Sum average	$\sum_{i=2}^{2N_g} i p_{x+y}(i)$ .
Sum variance	$\sum_{i=2}^{2N_g} (i - f_s)^2 p_{x+y}(i)$ .
Sum entropy	$-\sum_{i=2}^{2N_g} p_{x+y}(i) \log p_{x+y}(i)$ .
Entropy	$-\sum_i \sum_j p(i, j) \log p(i, j)$ .
Difference variance	$\sum_{i=0}^{N_g-1} i^2 p_{x-y}(i)$ .
Difference entropy	$-\sum_{i=0}^{N_g-1} p_{x-y}(i) \log p_{x-y}(i)$ .
Info. measure of corr. 1	$\frac{S(X;Y) - S_1(X;Y)}{\max(S(X), S(Y))}$ .
Info. measure of corr. 2	$\sqrt{(1 - \exp[-2(H_2(X;Y) - H(X;Y))])}$ .
Max. corr. coeff.	$\sqrt{\lambda_2}$ , of $Q(i, j) = \sum_k \frac{p(i, k)p(j, k)}{p_x(i)p_y(k)}$ .

1195 computed such as:

$$C_{k_1, k_2} = \sum_{m=0}^{M-1} \sum_{n=0}^{N-1} p_{m,n} \cos \left[ \frac{\pi}{M} \left( m + \frac{1}{2} \right) k_1 \right] \cos \left[ \frac{\pi}{N} \left( n + \frac{1}{2} \right) k_2 \right] , \quad (35)$$

1196 where  $C_{k_1, k_2}$  is the DCT coefficient at the position  $k_1, k_2$ ,  $M$  and  $N$  are the di-  
 1197 mension of the neighbourhood and  $p_{m,n}$  is the pixel SI at the position  $p_{m,n}$ .

1198 In the same spirit, Viswanath et al. (2012) projected T<sub>2</sub>-W images into the  
 1199 wavelet space and used the coefficients obtained from the decomposition as fea-  
 1200 tures. The wavelet family used for the decomposition was the Haar wavelet.

1201 The position of a voxel within the prostate was also considered a possible  
 1202 feature. Litjens et al. (2011) computed the Euclidean distance from each voxel  
 1203 to the prostate center as well as the individual distance in the three directions  
 1204  $x$ ,  $y$  and  $z$ . Chan et al. (2003) embedded the same information but this time  
 1205 using cylindrical coordinate  $r$ ,  $\theta$  and  $z$  corresponding to the radius, azimuth and  
 1206 elevation respectively.

#### 1207 – *Region-wise detection:*

1208 Unlike the previous section, another strategy is to study an entire region and  
 1209 extract characteristic features corresponding to this region.

1210 The most common approach reviewed can be classified as statical methods.  
 1211 Full map corresponding to feature types presented in the previous section are  
 1212 computed. Then, ROIs are defined and statistics are extracted from each of these  
 1213 regions. The first type of statistic is based on percentiles and is widely used (Antic  
 1214 et al. (2013), Litjens et al. (2012b, 2011), Peng et al. (2013), Tiwari et al. (2013,  
 1215 2010, 2009b), Viswanath et al. (2011, 2008a,b, 2012), Vos et al. (2012, 2008a,  
 1216 2010, 2008b)). In fact, once that a ROI is defined, the features corresponding  
 1217 the  $n^{\text{th}}$  percentile is used as feature. This  $n$  can take any value between 0 and  
 1218 100. This threshold is usually manually determined observing the distribution and  
 1219 corresponds to the best discriminant value differentiating malignant and healthy  
 1220 tissue. in addition, statistic-moments such as mean, standard deviation, kurtosis  
 1221 and skewness are also used (Ampeliotis et al. (2007, 2008), Antic et al. (2013),  
 1222 Niaf et al. (2012, 2011), Peng et al. (2013)).

1223 Another subset of features are anatomic which were also used by Litjens et al.  
 1224 (2012b) and Matulewicz et al. (2013). Litjens et al. (2012b) computed the volume,  
 1225 compactness and sphericity related to the region to integrate it in their feature  
 1226 vector to later classify. Matulewicz et al. (2013) introduced four features corre-  
 1227 sponding to the percentage of tissue belonging to the regionsPZ, CG, periurethral

region or outside prostate region for the considered ROI.

In contrast to anatomical are histogram-based features. For instance, Liu et al. (2013) introduced four different types of histogram-based features. The first type corresponds to the histogram of the SI of the image. The second type is the histogram of oriented gradient (HOG) (Dalal and Triggs (2005)). HOG descriptor describes the local shape of the object of interest by using gradient directions distribution. This descriptor is extracted mainly in three steps. First the gradient image and its corresponding magnitude and direction are computed. Then, the ROI is divided into cells and an oriented-based histogram is generated for each cell. At each pixel location, the orientation of the gradient will vote for a bin of the histogram and this vote is weighted by the magnitude of the same gradient. Finally, The cells are grouped into block and each block is normalized. The third histogram-based type used by Liu et al. (2013) was shape context (Belongie et al. (2002)). The shape context is also a way to describe the shape of an object of interest. First, a set of points defining edges have to be detected and for each point of each edge, a log-polar-based histogram is computed using the relative points distribution. The last set of histogram-based feature extracted is based on the framework of Zhao et al. (2012) which is using the Fourier transform of the histogram created via local binary pattern (LBP) (Ojala et al. (1996)). LBP is generated by comparing the value of the central pixel with its 8-connected neighbours. Then, in the ROI, the histogram of the LBP distribution is computed. The discrete fourier transform (DFT) of the LBP histogram is used to make the feature invariant to rotation.

The last group of region-based feature is based on fractal analysis. The features proposed are based on estimating the fractal dimension which is a statistical index representing the complexity of what is analysed. Lv et al. (2009) proposed two features based on fractal dimension: (i) texture fractal dimension and (ii) histogram fractal dimension. The first feature is based on estimating the fractal dimension on the SI of each image. Hence, this feature is a statistical characteristic of the image roughness. The second fractal dimension is estimated in the PDF of each image and is characteristic of the complexity of the PDF. Lopes et al. (2011) proposed a 3D version to estimate the fractal dimension of a volume using wavelet decomposition.

#### *4.2.2. DCE-based features*

DCE-MRI is more commonly based on a SI analysis over time as presented in Sect. 2.3.2. The parameters extracted used in CAD system during the DCE-MRI analysis are presented

Table 10: Parameters used as features for a DCE semi-quantitative analysis in CAD systems.

Semi-quantitative features	Explanations
<i>Amplitude features:</i>	
$S_0$	Amplitude at the onset of the enhancement
$S_{\max}$	Amplitude corresponding to 95% of the maximum amplitude
$S_p$	Amplitude corresponding to the maximum amplitude
$S_f$	Amplitude at the final time point
<i>Time features:</i>	
$t_0$	Time at the onset of the enhancement
$t_{\max}$	Time corresponding to 95% of the maximum amplitude
$t_p$	Time corresponding to the maximum amplitude
$t_f$	Final time
$t_{tp}$	Time to peak which is the time from $t_0$ to $t_p$
<i>Derivatives and integral features:</i>	
$WI$	Wash-in rate corresponding to the signal slope from $t_0$ to $t_m$ or $t_p$
$WO$	Wash-out rate corresponding to the signal slope from $t_m$ or $t_p$ to $t_p$
$IAUC$	Initial area under the curve which is the area between $t_0$ to $t_f$

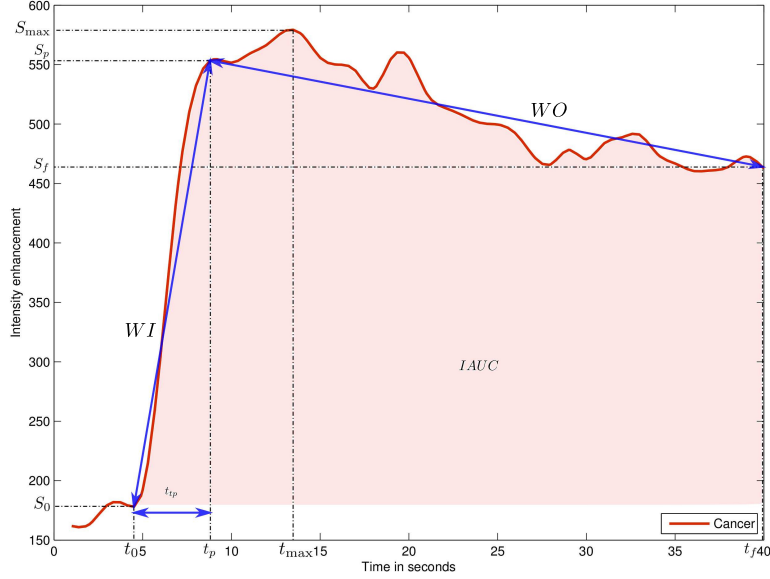


Figure 17: Graphical representation of the different semi-quantitative features used for DCE-MRI analysis.

- 1265 — **Whole-spectra approach:** Some studies are using the whole DCE time series  
1266 as feature vector such as Ampeliotis et al. (2007, 2008), Tiwari et al. (2012) and  
1267 Viswanath et al. (2008a,b). In some cases, the high-dimensional feature space is  
1268 reduced using dimension reduction methods as it will be presented in the next  
1269 section (see Sect. 4.3).
- 1270 — **Semi-quantitative approach:** Semi-quantitative approaches are based on mod-  
1271 elling mathematically the DCE time series. The parameters modelling the signal  
1272 are commonly used mainly due to the simplicity of their computation. Paramet-  
1273 ers included in semi-quantitative analysis are summarized in Tab. 10 and also  
1274 graphically depicted in Fig. 17. A set of time features corresponding to specific  
1275 amplitude level (start, maximum and end) are extracted. Then, derivative and in-  
1276 tegral features are also considered as discriminative and are commonly computed.
- 1277 — **Quantitative approach:** As presented in Sect. 2.3.2, quantitative approaches  
1278 correspond to mathematical-pharmacokinetic models based on physiological ex-  
1279 changes. Four different models have been used in CAD systems.  
1280 The most common model reviewed was the *Brix model* (Artan et al. (2010,



1281 2009), Liu et al. (2009), Ozer et al. (2009, 2010), Sung et al. (2011)). This model  
 1282 is formalized such as:

$$\frac{S(t)}{S(0)} = 1 + Ak_{ep} \left( \frac{\exp(-k_{ep}t) - \exp(-k_{el}t)}{k_{el} - k_{ep}} \right) , \quad (36)$$

1283 where  $S(\cdot)$  is the DCE signal,  $A$  is the parameter simulating the tissue proper-  
 1284 ties,  $k_{el}$  is the parameter related to the first-order elimination from the plasma  
 1285 compartment and  $k_{ep}$  is the parameter of the transvascular permeability and the  
 1286 parameters  $k_{ep}$ ,  $k_{el}$  and  $A$  are computed from the MRI data and used as features.

1287 Thus, the parameters  $k_{ep}$ ,  $k_{el}$  and  $A$  are computed and used as features.

1288 The Tofts model (Tofts (1997)) was used by Giannini et al. (2013), Langer  
 1289 et al. (2009), Mazzetti et al. (2011), Niaf et al. (2012, 2011). The DCE signal  
 1290 relative to the concentration is modelled as:

$$C_t(t) = v_p C_p(t) + K_{trans} \int_0^t C_p(\tau) \exp(-k_{ep}(t - \tau)) d\tau , \quad (37)$$

1291 where  $C_t(\cdot)$  is the concentration of the medium,  $C_p(\cdot)$  is the AIF which have to be  
 1292 estimated independently,  $K_{trans}$  is the parameter related to the diffuse transport  
 1293 of media across the capillary endothelium,  $k_{ep}$  is the parameter related to the  
 1294 exchanges back into the vascular space and  $v_e$  is the extravascular-extracellular  
 1295 space fraction defined such that  $v_e = 1 - v_p$ . Thus, the parameters  $K_{trans}$ ,  $k_{ep}$  and  
 1296  $v_e$  are computed and used as features in this model.

1297 Mazzetti et al. (2011) and Giannini et al. (2013) used the Weibull function  
 1298 empirically formalized as:

$$S(t) = At \exp(-t^B) , \quad (38)$$

1299 where  $A$  and  $B$  are the two parameters which have to be inferred.

1300 They also used another empirical model which is based on the West-like  
 1301 function and named the phenomenological universalities model (Castorina et al.  
 1302 (2006)) formalized as:

$$S(t) = \exp \left[ rt + \frac{1}{\beta} a_0 - r (\exp(\beta t) - 1) \right] , \quad (39)$$

1303 where the parameters  $\beta$ ,  $a_0$  and  $r$  are inferred.

1304 For all these models, the parameters are inferred using an optimization curve  
 1305 fitting approach.

### 4.2.3. MRSI-based features

— **Whole spectra approach:** As in the case of DCE analysis, one common approach is to incorporate the whole MRSI spectra in the feature vector for classification (Kelm et al. (2007), Matulewicz et al. (2013), Parfait et al. (2012), Tiwari et al. (2013, 2010, 2007, 2009a,b), Viswanath et al. (2008a)). Sometimes post-processing involving dimension reduction methods is performed to reduce the complexity during the classification as it will be presented in Sect. 4.3.

— **Quantification approach:** We can reiterate that in MRSI only few biological markers (cf., choline, creatine and citrate metabolites mainly) are known to be useful to discriminate CaP and healthy tissue. Then, concentrations of these metabolites can be considered as a feature used for classification. In order to perform this quantification, four different approaches have been used. The QUEST (Ratiney et al. (2005)), AMARES (Vanhamme et al. (1997)) and VARPRO (Coleman and Li (1993)) models were used by Kelm et al. (2007). They are all time-domain quantification methods varying by the type of pre-knowledge embedded and the optimization approaches used to solve the quantification problem. Unlike the time-domain quantification approaches, Parfait et al. (2012) used the LcModel approach (Provencher (1993)) which solves the optimization problem in the frequency domain.

Once the different concentrations are computed, Kelm et al. (2007) calculated the relative concentrations (Eq. (40) and (41)) and used them as features. However, Parfait et al. (2012) used each metabolite concentrations individually.

$$R_1 = \frac{[\text{Cho}] + [\text{Cr}]}{[\text{Cit}]} . \quad (40)$$

$$R_2 = \frac{[\text{Cit}]}{[\text{Cho}] + [\text{Cr}] + [\text{Cit}]} , \quad (41)$$

where Cit, Cho and Cr are the concentration of citrate, choline and creatine respectively.

— **Wavelet decomposition approach:** Tiwari et al. (2012) performed a wavelet packet decomposition (Coifman and Wickerhauser (1992)) with the Haar wavelet basis function and used the coefficients of this decomposition as features for further classification.

### 4.3. Feature selection and feature extraction

As presented in the previous section, a wide variety of features can be computed (see Tab. 7). This often leads from multi-parametric MRI data to a high complexity

Table 11: Overview of the feature selection and extraction methods used in CAD systems.

Dimension reduction methods	References
<i>Feature selection:</i>	
Statistical test	[17-18,41]
MI-based methods	[18-19,37]
<i>Feature extraction:</i>	
Linear mapping	
PCA	[27-28,31]
Non-linear mapping	
Laplacian eigenmaps	[26,28-30,33,36]
LLE and LLE-based	[27-28,33-34]

feature space which might mislead or corrupt the classifier which used for training. Thus, it is of interest to reduce the number of dimensions before proceeding to the classification task. The strategies used can be grouped as: (i) feature selection and (ii) feature extraction. Those methods used in CAD system are summarized in Tab. 11.

#### 4.3.1. Feature selection

The feature selection strategy is based on selecting the most discriminative feature dimensions of the high-dimensional space. Thus, the low-dimensional space is then composed of a subset of the original features detected. In this section, methods employed in the studies reviewed will be briefly presented. More extensive reviews specific to feature selection can be found in Saeys et al. (2007).

Niaf et al. (2012, 2011) make use of the p-value by using the independent two-sample t-test with equal mean for each feature dimension. In this statistical test, it is that there are two classes: CaP and healthy tissue. Hence, for each particular feature, the distribution of each class can be characterized by their means  $\bar{X}_1$  and  $\bar{X}_2$  and standard deviation  $s_{X_1}$  and  $s_{X_2}$ , respectively. Hence, the null hypothesis test is based on the fact that these both distribution means are equal. Thus, the t-statistic used to verify the null hypothesis is then formalized such that:

$$t = \frac{\bar{X}_1 - \bar{X}_2}{s_{X_1 X_2} \cdot \sqrt{\frac{1}{n_1} + \frac{1}{n_2}}} , \quad (42)$$

$$s_{X_1 X_2} = \sqrt{\frac{(n_1 - 1)s_{X_1}^2 + (n_2 - 1)s_{X_2}^2}{n_1 + n_2 - 2}} ,$$

1355 where  $n_1$  and  $n_2$  are the number of samples in each class.

1356 From Eq. (42), it can be seen that more the means of the class distribution  
1357 diverge, the larger the  $t$ -statistic  $t$  will be, implying that this particular feature is  
1358 more relevant and able to make the distinction between the two classes.

1359 The  $p$ -value statistic can be deduced from the  $t$ -test and corresponds to the  
1360 probability of obtaining such an extreme test assuming that the null hypothesis is  
1361 true (Goodman (1999)). Hence, smaller the  $p$ -value, the more likely we are to reject  
1362 the null hypothesis and more relevant the feature is likely to be.

1363 Finally, the features can be ranked and the most significant features can be se-  
1364 lected. However, this technique suffers from a main drawback since it assumes that  
1365 each feature is independent, which is unlikely to happen and introduces a high degree  
1366 of redundancy in the features selected.

1367 Vos et al. (2012) employed a similar feature ranking approach but make use of  
1368 the Fisher discriminant ratio to compute the relevance of each feature dimension.  
1369 Taking the aforementioned formulation, the Fisher discriminant ratio is formalized  
1370 as the ratio of the interclass variance to the intraclass variance as:

$$F_r = \frac{\bar{X}_1 - \bar{X}_2}{s_{X_1}^2 + s_{X_2}^2} . \quad (43)$$

1371 Hence, a feature dimension can be seen as more relevant when the interclass  
1372 variance is maximum and the intraclass variance in minimum. Once the features  
1373 are ordered, Vos et al. (2012) select the feature dimensions with the larger Fisher  
1374 discriminant ratio.

1375 MI can also be used to select a subset of feature dimensions. Definition of the MI  
1376 was presented in Sect. 3.3.2 and formalized in Eq. (30) and as previously mentioned,  
1377 the computation of the entropies involves the estimation of some PDFs and the data  
1378 being usually continuous variables, it is then necessary to estimate the PDFs using  
1379 a method such as Parzen windows.

1380 Peng et al. (2005) introduced two main criteria to select the feature dimensions:  
1381 (i) maximal relevance and (ii) minimum redundancy.

1382 Maximal relevance criterion is based on the paradigm that the classes and the  
 1383 feature dimension which has to be selected have to share a maximal MI and can be  
 1384 formalized:

$$\arg \max Rel(\mathbf{x}, c) = \frac{1}{|\mathbf{x}|} \sum_{x_i \in \mathbf{x}} MI(x_i, c) , \quad (44)$$

1385 where  $\mathbf{x} = \{x_i, i = 1, \dots, d\}$  is a feature vector of  $d$  dimensions and  $c$  is the class  
 1386 considered.

1387 As in the previous method, using maximal relevance criterion alone will imply  
 1388 independence between each feature dimension which is usually not true.

1389 Minimal redundancy criterion will force selection of a new feature dimension  
 1390 which shares as little as possible MI previously selected feature dimension. It can be  
 1391 formalized as:

$$\arg \min Red(\mathbf{x}) = \frac{1}{|\mathbf{x}|^2} \sum_{x_i, x_j \in \mathbf{x}} MI(x_i, x_j) . \quad (45)$$

1392 Combination of these two criteria is known as minimum redundancy maximum  
 1393 relevance (mRMR)<sup>5</sup> (Peng et al. (2005)) and are computed as a difference or quotient  
 1394 of Eqs. (44) and (45).

1395 Niaf et al. (2012, 2011) make use of maximal relevance criterion alone and also of  
 1396 both mRMR difference and quotient criterion. Viswanath et al. (2012) also reduced  
 1397 their feature vector via mRMR difference and quotient.

#### 1398 4.3.2. Feature extraction

1399 The feature extraction strategy is related to dimension reduction methods but not  
 1400 selecting discriminative features. Instead, these methods aim at mapping the data  
 1401 from the high-dimensional space into a low-dimensional space created to maximize  
 1402 the separability between the classes. The mapping can be performed in a linear or a  
 1403 non-linear manner. Again, only methods employed in CAD system will be reviewed  
 1404 in this section. We refer the reader to the review of Fodor (2002) for a full review of  
 1405 feature extraction techniques.

1406 PCA is the most commonly used linear mapping method in CAD systems. PCA  
 1407 is based on finding the orthogonal linear transform mapping the original data into a  
 1408 low-dimensional space. The space is defined such that the linear combinations of the

---

<sup>5</sup>mRMR implementation can be found at: <http://penglab.janelia.org/proj/mRMR/>

original data with the  $k^{th}$  greatest variances will lie on the  $k^{th}$  principal components (Jolliffe (2002)).

The principal components can then be computed by using the eigenvectors-eigenvalues decomposition of the covariance matrix. Let  $\mathbf{x}$  denote the data matrix. Then the covariance matrix is defined as:

$$\Sigma = \mathbf{x}^T \mathbf{x} . \quad (46)$$

The eigenvectors-eigenvalues decomposition can be formalized as:

$$\mathbf{v}^{-1} \Sigma \mathbf{v} = \Lambda , \quad (47)$$

where  $\mathbf{v}$  are the eigenvectors matrix and  $\Lambda$  is a diagonal matrix containing the eigenvalues.

It is then possible to find the new low-dimensional space by sorting the eigenvectors using the eigenvalues and finally selecting the largest eigenvalues. The total variation that is the sum of the principal eigenvalues of the covariance matrix (Fodor (2002)), usually corresponds to the 95% to 98% of the cumulative sum of the eigenvalues. Tiwari et al. (2008, 2009a, 2012) used PCA in order to reduce the dimensionality of their feature vector.

Non-linear mapping was also used for dimension reduction. It is mainly based on Laplacian eigenmaps and locally linear embedding (LLE) methods. Laplacian eigenmaps<sup>6</sup>, also referred as spectral clustering in computer vision, aim to find a low-dimensional space in which the proximity of the data should be preserved from the high-dimensional space (Belkin and Niyogi (2001), Shi and Malik (2000)). Thus, two adjacent data points in the high-dimensional space should also be close in the low-dimensional space. Similarly, two far away data points in the high-dimensional space also should be distant in the low-dimensional space. To compute this projection, an adjacency matrix is defined as:

$$W(i, j) = \exp \|\mathbf{x}_i - \mathbf{x}_j\|_2 , \quad (48)$$

where  $\mathbf{x}_i$  and  $\mathbf{x}_j$  are the two samples considered.

Then, the low-dimensional space will be found by solving the generalized eigenvectors-eigenvalues problem:

$$(D - W)\mathbf{y} = \lambda D\mathbf{y} , \quad (49)$$

---

<sup>6</sup>Laplacian eigenmap implementation is available at: <http://www.cse.ohio-state.edu/~mbelkin/algorithms/algorithms.html>

where  $D$  is a diagonal matrix such that  $D(i, i) = \sum_j W(j, i)$ .

Finally the low-dimensional space is defined by the  $k$  eigenvectors of the  $k$  smallest eigenvalues (Belkin and Niyogi (2001)). Tiwari et al. (2007, 2009a,b), Viswanath et al. (2008b) used this spectral clustering to project their feature vector into a low-dimensional space. The feature space in these studies is usually composed of features extracted from a single or multiple modalities and then concatenated before applying the Laplacian eigenmaps dimension reduction technique.

Tiwari et al. (2013, 2009a) used a slightly different approach by combining the Laplacian eigenmaps techniques with a prior multi-kernel learning strategy. First, multiple features were extracted for multiple modalities. The features of a single modality were then mapped to a higher dimensional space via the Kernel trick (Aizerman et al. (1964)) and more precisely using a Gaussian kernel. Then, each kernel associated with each modality was linearly combined to obtain a combined kernel  $K$ . Then, the computation of the adjacency matrix  $W$  took place and the same scheme as in Laplacian eigenmaps is applied. However, in order to use the combined kernel, Eq. (49) is rewritten as:

$$K(D - W)K^T \mathbf{y} = \lambda K D K^T \mathbf{y} . \quad (50)$$

It can be solved as a generalized eigenvectors-eigenvalues problem as previously. Viswanath et al. (2011) used Laplacian eigenmaps inside a bagging framework in which multiple embeddings are generated by successively selecting feature dimensions.

LLE<sup>7</sup> is another common non-linear dimension reduction technique widely used, first proposed by Roweis and Saul (2000). LLE is based on the fact that a data point in the feature space can be characterized by its neighbours. Thus, it was proposed to represent each data point in the high-dimensional space as the linear combination of its  $k$ -nearest neighbours. This can be expressed as:

$$\hat{\mathbf{x}}_i = \sum_j W(i, j) \mathbf{x}_j , \quad (51)$$

where  $\hat{\mathbf{x}}_i$  are the data point estimated using its neighbouring data points  $\mathbf{x}_j$ .

Hence, this problem which has to be solved at this stage is to estimate the weight matrix  $W$ . This problem can be tackled using a least square optimization scheme by optimizing the following objective function:

---

<sup>7</sup>LLE implementation is available at: <http://www.cs.nyu.edu/~roweis/lle/code.html>

$$\begin{aligned} \hat{W} &= \arg \min_W \sum_i |\mathbf{x}_i - \sum_j W(i, j) \mathbf{x}_j|^2, \\ &\text{subject to } \sum_j W(i, j) = 1, \end{aligned} \quad (52)$$

1464 Then, the essence of LLE is to project the data into a low dimension space, while  
 1465 retaining the data organization. Thus, the projection into the low dimension space  
 1466 can be seen as an optimization problem as:

$$\hat{\mathbf{y}} = \arg \min_{\mathbf{y}} \sum_i |\mathbf{y}_i - \sum_j W(i, j) \mathbf{y}_j|^2. \quad (53)$$

1467 This optimization can be performed as an eigenvectors-eigenvalues problem by  
 1468 finding the  $k^{\text{th}}$  eigenvectors corresponding to the  $k^{\text{th}}$  smallest eigenvalues of the sparse  
 1469 matrix  $(I - W)^T(I - W)$ . Tiwari et al. (2008, 2009a), Viswanath et al. (2008a,b) used  
 1470 LLE as a dimension reduction technique to reduce the complexity of their feature  
 1471 vector.

1472 Tiwari et al. (2008) used a modified version of the LLE algorithm in which they  
 1473 applied LLE in a bagging approach with multiple neighbourhood sizes. The different  
 1474 embeddings obtained are then fused using the maximum likelihood (ML) estimation.

#### 1475 4.4. Classification

##### 1476 4.4.1. Classifier

1477 Once the feature vector has been extracted and eventually the complexity re-  
 1478 duced, it is possible to make a decision and classify this feature vector to belong to  
 1479 CaP or healthy tissue. Classification methods used in CAD system to distinguish  
 1480 these two classes are summarized in Tab. 12. A full review of classification methods  
 1481 used in pattern recognition can be found in Bishop (2006).

##### 1482 – **Rule-based method:**

1483 Lv et al. (2009) make use of a decision stump classifier to distinguish CaP and  
 1484 healthy classes.

1485 Puech et al. (2009) detect CaP by implementing a given set of rules using a  
 1486 score medical decision making approach. The feature values are compared with  
 1487 a pre-defined threshold. Then, at each comparison, the final score is incremented  
 1488 or not, depending on the threshold and the final decision is taken depending of  
 1489 the final score.



Table 12: Overview of the classifiers used in CAD systems.

Classifier	References
<i>Rule-based method:</i>	[15,24]
<i>Clustering methods:</i>	
<i>k</i> -means clustering	[26-28,33-34]
<i>k</i> -NN	[11,18-19]
<i>Linear model classifiers:</i>	
LDA	[3,6,18-19,41]
Logistic regression	[8-9]
<i>Non-linear classifier:</i>	
QDA	[37]
<i>Probabilistic classifier:</i>	
Naive Bayes	[7,17-19]
<i>Ensemble learner classifiers:</i>	
AdaBoost	[14]
Random forest	[8,31-32,35]
Probabilistic boosting tree	[29-31,36]
<i>Kernel method:</i>	
Gaussian processes	[8]
<i>Sparse kernel methods:</i>	
SVM	[4-6,8,10-11,13-14,18-23,25,31,38-40]
RVM	[20-21]
<i>Neural network:</i>	
Multiple layer perceptron	[16,22]
Probabilistic neural network	[1-2,36]
<i>Graphical model classifiers:</i>	
Markov random field	[12,21]
Conditional random field	[4-5]

1490 – ***Clustering methods:***

1491  $k$ -nearest neighbour ( $k$ -NN) is one of the simplest supervised machine learn-  
 1492 ing classification methods. In this method, a new unlabelled vector is assigned  
 1493 to the most represented class from its  $k$  nearest-neighbours in the feature space.  
 1494 The parameter  $k$  is usually an odd number in order to avoid any tie case.  $k$ -NN  
 1495 was one of the method used by Niaf et al. (2012, 2011) mainly to make a compar-  
 1496 ison with different machine learning techniques. Litjens et al. (2012b) used this  
 1497 method to roughly detect potential CaP voxels before performing a region-based  
 1498 classification.

1499  $k$ -means is an unsupervised clustering method in which the data have to be  
 1500 partitioned into  $k$  clusters. The discovery of the clusters is an iterative procedure.  
 1501 First  $k$  random centroids are defined in the feature space and each data point is  
 1502 assigned to the nearest centroid. Then, the centroid position for each cluster is  
 1503 updated by computing the mean of all the data points belonging to this partic-  
 1504 ular cluster. Both assignment and updating are repeated until the centroids are  
 1505 stable. The number of clusters  $k$  is usually defined as the number of classes. This  
 1506 algorithm can also be used for “on-line” learning. In case that new data has to  
 1507 be incorporated, the initial centroid positions correspond to the results of a previ-  
 1508 ous  $k$ -means training and is followed by the assignment-updating stage previously  
 1509 explained.

1510 Tiwari et al. (2007, 2009a) used  $k$ -means in an iterative procedure. Three clus-  
 1511 ters were defined corresponding to CaP, healthy and non-prostate, respectively.  
 1512  $k$ -means was applied iteratively and the voxels corresponding to the largest cluster  
 1513 were excluded under the assumption that it is assigned to “non-prostate” cluster.  
 1514 The iteration stop when the number of voxels composing all clusters remaining is  
 1515 smaller than a threshold.

1516 Tiwari et al. (2008), Viswanath et al. (2008a,b) used  $k$ -means in a repetitive  
 1517 manner to be less sensitive to the centroids initialisation. Thus,  $k$  clusters were  
 1518 generated  $T$  times. The final assignment was performed by majority voting using  
 1519 a co-association matrix as proposed by Fred and Jain (2005).

1520 – ***Linear model classifiers:***

1521 Linear discriminant analysis (LDA) can be used as a classification method in  
 1522 which the optimal linear separation between two classes is found by maximizing  
 1523 the interclass variance and minimizing the intraclass variance (Friedman (1989)).  
 1524 The linear discriminant function is defined as:

$$\delta_k(\mathbf{x}_i) = \mathbf{x}_i^T \Sigma^{-1} \mu_k - \frac{1}{2} \mu_k^T \Sigma^{-1} \mu_k + \log(\pi_k) , \quad (54)$$

where  $\mathbf{x}_i$  is an unlabelled feature vector,  $\Sigma$  is the covariance matrix of the training data,  $\mu_k$  is the mean vector of the class  $k$  and  $\pi_k$  is the prior probability of class  $k$ .

To perform the classification, a sample  $\mathbf{x}_i$  will be assigned to the class which maximizes the discriminant function:

$$C(\mathbf{x}_i) = \arg \max_k \delta_k(\mathbf{x}_i) . \quad (55)$$

covariance matrix  $\Sigma_k$  specific at each class is computed Antic et al. (2013), Chan et al. (2003), Niaf et al. (2012, 2011), Vos et al. (2012) used LDA to classify their feature vectors defining two classes CaP *versus* healthy.

Logistic regression can be used to perform binary classification and can provide the probability of an observation to belong to a class. The posterior probability of one of the class  $c_1$  can be written as:

$$p(c_1|\mathbf{x}_i) = \frac{1}{1 + \exp(-\mathbf{w}^T \mathbf{x}_i)} , \quad (56)$$

with  $p(c_2|\mathbf{x}_i) = 1 - p(c_1|\mathbf{x}_i)$  and where  $\mathbf{w}$  is the vector of the regression parameters allowing to obtain a linear combination of the input feature vector  $\mathbf{x}_i$ .

Thus, an unlabelled observation  $\mathbf{x}_i$  will be assigned to the class which maximizes the posterior probability:

$$C(\mathbf{x}_i) = \arg \max_k p(C = k|\mathbf{x}_i) . \quad (57)$$

From Eq. (56), one can see that the key to classification using logistic regression model is to infer the set of parameters  $\mathbf{w}$  through a learning stage in the training set. This vector of parameters  $\mathbf{w}$  can be inferred by finding the maximum likelihood estimates. This step can be performed through an optimization scheme, using a quasi-Newton method (Byrd et al. (1995)), which iteratively seeks for the local minimum in the derivative of Eq. (56).

Kelm et al. (2007), Puech et al. (2009) used a logistic regression to create a linear probabilistic model in order to classify their feature vectors.

#### – ***Non-linear model classifier:***

Viswanath et al. (2012) used the most general quadratic discriminant analysis (QDA) instead of LDA. Unlike in LDA in which one assumes that the class covariance matrix  $\Sigma$  is identical for all the classes, in QDA, a covariance matrix

1552  $\Sigma_k$  specific to each class is computed. Thus, Eq. (54) becomes:

$$\delta_k(\mathbf{x}_i) = \mathbf{x}_i^T \Sigma_k^{-1} \mu_k - \frac{1}{2} \mu_k^T \Sigma_k^{-1} \mu_k + \log(\pi_k) . \quad (58)$$

1553 The classification scheme in the case of the QDA is identical to Eq. (55).

1554 – ***Probabilistic classifier:***

1555 The most commonly used classifier is the naive Bayes classifier which is a prob-  
1556 abilistic classifier assuming independence between each feature dimension (Rish  
1557 (2001)). This classifier is based on Bayes' theorem:

$$p(C = k|\mathbf{x}) = \frac{p(C)p(\mathbf{x}|C)}{p(\mathbf{x})} , \quad (59)$$

1558 where  $p(C = k|\mathbf{x})$  is the posterior probability,  $p(C)$  is the prior probability,  $p(\mathbf{x}|C)$   
1559 is the likelihood and  $p(\mathbf{x})$  is the evidence.

1560 However, the evidence term is usually discarded since it is not class dependent  
1561 and plays the role of a normalization term. Hence, in a classification scheme, an  
1562 unlabelled observation will be classified to the class which maximizes the posterior  
1563 probability as:

$$C(\mathbf{x}_i) = \arg \max_k p(C = k|\mathbf{x}_i) , \quad (60)$$

$$p(C = k|\mathbf{x}_i) = p(C = k) \prod_{j=1}^n p(x_{ij}, |C = k) , \quad (61)$$

1564 where  $d$  is the number of dimensions of the feature vector  $\mathbf{x}_i = \{x_{i1}, \dots, x_{id}\}$ .

1565 Usually, a model includes both the prior and likelihood probabilities and it  
1566 is common to use an equal prior probability for each class or eventually a value  
1567 depending of the relative frequency derived from the training set. Regarding the  
1568 likelihood probability, it is common to choose a Normal distribution to character-  
1569 ize each class. Thus, each class will be characterized by two parameters: (i) the  
1570 mean and (ii) the standard deviation. These parameters can be inferred from the  
1571 training set by using the ML approach.

1572 Giannini et al. (2013), Mazzetti et al. (2011), Niaf et al. (2012, 2011) used  
1573 the naive Bayes classifier to classify their feature vectors to either malignant or  
1574 healthy. The Normal distribution was used as the likelihood probability for that  
1575 model.

– **Ensemble learner classifiers:**

AdaBoost is an adaptive method based on an ensemble learner and was initially proposed by Freund and Schapire (1997). AdaBoost linearly combines several weak learners resulting into a final strong classifier. A weak learner is defined as a classification method performing slightly better than random classification. Popular choices regarding the weak learner methods are: decision stump, decision tree learners (cf., iterative dichotomiser 3 (ID3) (Quinlan (1986)), C4.5 (Quinlan (1993)), classification and regression tree (CART) (Breiman et al. (1984))).

AdaBoost is considered as an adaptive method in the way that the weak learners are selected. The selection is performed in an iterative manner. At each iteration  $t$ , the weak learner selected  $h_t$  corresponds to the one minimizing the classification error on a distribution of weights  $D_t$ , that is associated to the training sample. A weight  $\alpha_t$  is affected at each weak learner such that:

$$\alpha_t = \frac{1}{2} \ln \frac{1 - \epsilon_t}{\epsilon_t} , \quad (62)$$

where  $\epsilon_t$  corresponds to the classification error rate of the weak learner on the distribution of weight  $D_t$ .

Before performing a new iteration, the distribution of weight  $D_t$  is updated such that the weight associated with the misclassified samples by  $h_t$  will increase and the weights of well classified samples will decrease as shown in Eq. (63).

$$D_{t+1}(i) = \frac{D_t(i) \exp(-\alpha_t y_i h_t(\mathbf{x}_i))}{Z_t} , \quad (63)$$

where  $\mathbf{x}_i$  is the  $i^{\text{th}}$  sample corresponding to class  $y_i$  and  $Z_t$  is a normalization factor to impose that  $D_{t+1}$  to be a probability distribution.

This procedure allows to select a weak learner at the next iteration  $t+1$  which will classify in priority previous misclassified samples. Thus, after  $T$  iterations, the final strong classifier corresponds to the linear combination of the weak learners and the classification is performed such that:

$$C(\mathbf{x}_i) = \text{sign} \left( \sum_{t=1}^T \alpha_t h_t(\mathbf{x}_i) \right) . \quad (64)$$

Lopes et al. (2011) make use of the AdaBoost technique to perform their classification.

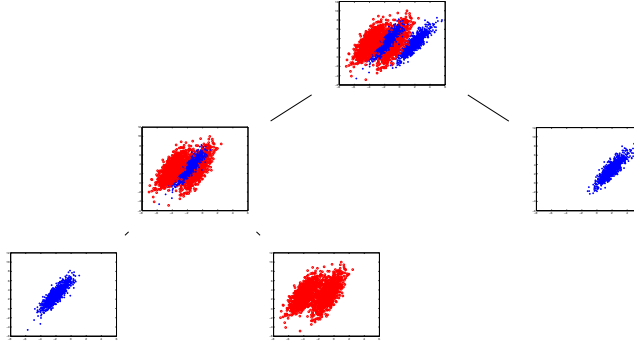


Figure 18: Representation of the capabilities of the probabilistic boosting tree algorithm to split at each node of the tree the positive and negative samples.

Random forest<sup>8</sup> is a classification method which is based on creating an ensemble of decision trees and was introduced by Breiman (2001). In the learning stage, multiple decision tree learners (Breiman et al. (1984)) will be trained. However, each decision tree will be trained with a different dataset. Each of these datasets corresponds to a bootstrap sample generated by randomly choosing  $n$  samples with replacement from the  $N$  samples available in the original set (Efron (1979)). Then, randomization is also part of the decision tree growth. At each node of the decision tree, from the bootstrap sample of  $D$  dimensions, a number of  $d \ll D$  dimensions will be randomly selected. Finally, the  $d^{\text{th}}$  dimension splitting the best the data will be used. This best splitting is often evaluated using MI (see Sect. 3.3.2). Finally, each tree is grown as much as possible without using any pruning procedure.

In the prediction stage, a sample is introduced in each tree and each of the tree will assign a class to this sample. Finally, it is common to use a majority voting approach to choose the final class label.

Kelm et al. (2007), Tiwari et al. (2013, 2012), Viswanath et al. (2009) make use of the random forest classifier to classify their feature vector.

Probabilistic boosting-tree is an ensemble classifier method which is sharing principles from AdaBoost but using them inside a decision tree (Tu (2005)). In the training stage, the probabilistic boosting-tree method grows a decision tree and at each node a strong classifier is learnt in an almost comparable scheme than

---

<sup>8</sup>Random forest implementation can be found at: [http://www.stat.berkeley.edu/~breiman/RandomForests/cc\\_software.htm](http://www.stat.berkeley.edu/~breiman/RandomForests/cc_software.htm)

1623 AdaBoost (see Eq. 64). Once the strong learner is trained, the training set will  
 1624 be split into two subsets which will be used to train the next strong classifiers  
 1625 in the next descending nodes. Thus, three cases are conceivable to decide which  
 1626 branch to propagate each sample  $\mathbf{x}_i$ :

- 1627 • if  $q(+1, \mathbf{x}_i) - \frac{1}{2} > \epsilon$  then  $\mathbf{x}_i$  is propagated to the right branch set and a weight  
 1628  $w_i = 1$  is assigned.
- 1629 • if  $q(-1, \mathbf{x}_i) - \frac{1}{2} > \epsilon$  then  $\mathbf{x}_i$  is propagated to the left branch set and a weight  
 1630  $w_i = 1$  is assigned.
- 1631 • else  $\mathbf{x}_i$  will be propagated in both branches with  $w_i = q(+1, \mathbf{x}_i)$  in the right  
 1632 branch and  $w_i = q(-1, \mathbf{x}_i)$  in the left branch.

1633 with  $\mathbf{w} = w_i, i = \{1, \dots, N\}$  corresponding to distribution of weights,  $N$  the  
 1634 number of samples as in AdaBoost and  $q(\cdot)$  is defined such as:

$$q(+1, \mathbf{x}_i) = \frac{\exp(2H(\mathbf{x}_i))}{1 + \exp(2H(\mathbf{x}_i))} , \quad (65)$$

$$q(-1, \mathbf{x}_i) = \frac{\exp(-2H(\mathbf{x}_i))}{1 + \exp(-2H(\mathbf{x}_i))} . \quad (66)$$

1635 Employing such a scheme tends to divide the data in such a way that positive  
 1636 and negative samples are naturally split as shown in Fig. 18.

1637 In the classification stage, the sample  $\mathbf{x}$  is propagated through the trees, where  
 1638 at each node, it will be classified by the strong classifier previously learned and  
 1639 where an estimation of the posterior distribution will be computed. The posterior  
 1640 distribution will correspond to the sum of the posterior distribution at each node  
 1641 of the tree.

1642 Tiwari et al. (2010, 2009b, 2012), Viswanath et al. (2011) make use of the  
 1643 probabilistic boosting-tree classifier.

#### 1644 – **Kernel method:**

1645 A Gaussian process<sup>9</sup> for classification is a kernel method in which it is assumed  
 1646 that the data can be represented by a single sample from a multivariate Gaus-  
 1647 sian distribution (Rasmussen and Williams (2005)). In the case of linear logistic  
 1648 regression for classification, the posterior probability can be expressed as:

---

<sup>9</sup>Gaussian process implementation can be found at: <http://www.gaussianprocess.org/gpml/code/matlab/doc/index.html>

$$\begin{aligned} p(y_i|\mathbf{x}_i, \mathbf{w}) &= \sigma(y_i f(\mathbf{x}_i)) , \\ f(\mathbf{x}_i) &= \mathbf{x}_i^T \mathbf{w} , \end{aligned} \quad (67)$$

where  $\sigma(\cdot)$  is the logistic function and  $\mathbf{w}$  are the parameters of the model.

Thus, the classification using Gaussian processes is based on affecting a Gaussian process prior over the function  $f(\mathbf{x})$  which will be characterized by a mean  $\bar{f}$  and covariance functions  $K$ . Thus, in the training stage, the best mean and covariance functions have to be inferred in regard to our training data using a Newton optimization and a Laplacian approximation.

The prediction stage can be performed in two stages. First, for a new observation  $\mathbf{x}_*$ , the corresponding probability  $p(f(\mathbf{x}_*)|f(\mathbf{x}))$  can be computed such that:

$$\begin{aligned} p(f(\mathbf{x}_*)|f(\mathbf{x})) &= \mathcal{N}(K_* K^{-1} \bar{f}, K_{**} - K_*(K')^{-1} K_*^T) , \\ K' &= K + W^{-1} , \\ W &= \nabla \nabla \log p(\mathbf{y}|f(\mathbf{x})) , \end{aligned} \quad (68)$$

where  $K_{**}$  is the variance of the testing sample  $\mathbf{x}_*$ ,  $K_*$  is the covariance of training-testing samples  $\mathbf{x}$  and  $\mathbf{x}_*$ .

Then, the function  $f(\mathbf{x}_*)$  is squashed using the sigmoid function and the probability of the class membership can be defined such that:

$$C(\mathbf{x}_*) = \sigma \left( \frac{\bar{f}(\mathbf{x}_*)}{\sqrt{1 + \text{var}(f(\mathbf{x}_*))}} \right) . \quad (69)$$

Only the work of Kelm et al. (2007) used Gaussian process for classification in order to distinguish CaP in MRSI data.

#### – *Sparse kernel methods:*

In Gaussian process, when a prediction has to be performed, the whole training data will be used to assign a label to the new observations. That is why, this method is also called kernel method. Sparse kernel category is composed of methods which rely only on few labelled observations in order to label new observations (Bishop (2006)).

Support vector machines (SVM)<sup>10</sup> is a sparse kernel method based on finding the best linear hyperplane (non-linear separation is discussed further) which

---

<sup>10</sup>SVM implementation can be found at: <http://www.csie.ntu.edu.tw/~cjlin/libsvm/>



separates two classes such as the margin between the two classes is maximized (Vapnik and Lerner (1963)). The margin is in fact the region defined by two hyperplanes splitting the two classes, such that no points lie in between. The distance between these two hyperplanes is equal to  $\frac{2}{\|\mathbf{w}\|}$  where  $\mathbf{w}$  is the normal vector of the hyperplane splitting the classes. Thus, maximizing the margin is equivalent to minimizing  $\|\mathbf{w}\|$ . Hence, This problem is solved by an optimization approach and formalized such that:

$$\begin{aligned} \arg \min_{\mathbf{w}} \quad & \frac{1}{2} \|\mathbf{w}^2\| , \\ \text{subject to} \quad & y_i(\mathbf{w} \cdot \mathbf{x}_i - b) \geq 1, \quad i = \{1, \dots, N\} , \end{aligned} \quad (70)$$

where  $\mathbf{x}_i$  is a training sample with is corresponding class label  $y_i$ .

From Eq. (70), it is important to notice that only few points from the set of  $n$  points have to be selected which will later define the hyperplane. This can be introduced in the optimization problem using Lagrange multipliers  $\alpha$ . All points which are not lying on the margin will be assigned a corresponding  $\alpha_i = 0$ . This can be formalized as:

$$\arg \min_{\mathbf{w}, b} \max_{\alpha \geq 0} \left\{ \frac{1}{2} \|\mathbf{w}\|^2 - \sum_{i=1}^n \alpha_i [y_i(\mathbf{w} \cdot \mathbf{x}_i - b) - 1] \right\} . \quad (71)$$

The different parameters can be inferred using quadratic programming. This version of SVM is known as hard-margin since that no point can lie in the margin area. However, this is highly probable to not find any hyperplane splitting the classes such as specified previously. Thus, a soft-margin optimization approach was proposed (Cortes and Vapnik (1995)), where points can lie into the margin but at the cost of penalty which will be minimized in the optimization process such that:

$$\arg \min_{\mathbf{w}, \xi, b} \max_{\alpha, \beta} \left\{ \frac{1}{2} \|\mathbf{w}\|^2 + C \sum_{i=1}^n \xi_i - \sum_{i=1}^n \alpha_i [y_i(\mathbf{w} \cdot \mathbf{x}_i - b) - 1 + \xi_i] - \sum_{i=1}^n \beta_i \xi_i \right\} . \quad (72)$$

The decision to assign the label to a new observation  $\mathbf{x}_i$  is taken such that:

$$C(\mathbf{x}_i) = \text{sign} \left( \sum_{n=1}^N \alpha_n (\mathbf{x}_n \cdot \mathbf{x}_i) + b_0 \right) , \quad (73)$$

where  $\mathbf{x}_n | n = \{1, \dots, S\}$ ,  $S$  being the support vectors.

SVM can also be used as a non-linear classifier by performing a kernel trick Boser et al. (1992). The original data  $\mathbf{x}$  can be projected in an high-dimensional space in which it is assumed that a linear hyperplane will split the classes. Different kernels are popular such as the RBF kernel, polynomial kernels or Gaussian kernel.

In prostate CAD system, SVM is the most popular classification method and was used in a multitude of research works: Artan et al. (2010, 2009), Chan et al. (2003), Kelm et al. (2007), Litjens et al. (2012b, 2011), Liu et al. (2013), Lopes et al. (2011), Niaf et al. (2012, 2011), Ozer et al. (2009, 2010), Parfait et al. (2012), Peng et al. (2013), Sung et al. (2011), Tiwari et al. (2012), Vos et al. (2012, 2008a, 2010, 2008b).

Relevant vector machine (RVM) is a sparse version of Gaussian process previously presented and was proposed by Tipping (2001). RVM is identical to a Gaussian process with following covariance function (Quinonero-Candela et al. (2002)):

$$K_{RVM}(\mathbf{x}_p, \mathbf{x}_q) = \sum_{j=1}^M \frac{1}{\alpha_j} \Phi_j(\mathbf{x}_p) \Phi_j(\mathbf{x}_q) , \quad (74)$$

where  $\phi(\cdot)$  is a Gaussian basis function,  $\mathbf{x}_i | i = \{1, \dots, N\}$  are the  $N$  training points and  $\boldsymbol{\alpha}$  are the weights.

As mentioned in Quinonero-Candela et al. (2002), the sparsity regarding the relevance vector arises if  $j\alpha_j^{-1} = 0$ . The set of parameters  $\boldsymbol{\alpha}$  is inferred using the expectation maximization algorithm. Ozer et al. (2009, 2010) make use of RVM and make a comparison with SVM for the task of CaP detection.

#### – **Neural network:**

Multilayer perceptron is a feed-forward neural network considered as well as the most successful model of this kind in pattern recognition (Bishop (2006)). The most well spread model used is based on a two layers model where a prediction of an observation is computed as:

$$C(\mathbf{x}_n, w_{ij}^{(1)}, w_{kj}^{(2)}) = \sigma \left[ \sum_{j=0}^M w_{kj}^{(2)} h \left( \sum_{i=0}^D w_{ij}^{(1)} x_{in} \right) \right] , \quad (75)$$

where  $h(\cdot)$  and  $\sigma(\cdot)$  are two activation functions usually non-linear,  $w_{ij}^{(1)}$  and  $w_{kj}^{(2)}$  are the weights associated with the linear combination with the input feature  $\mathbf{x}_n$  and the hidden unit, respectively.

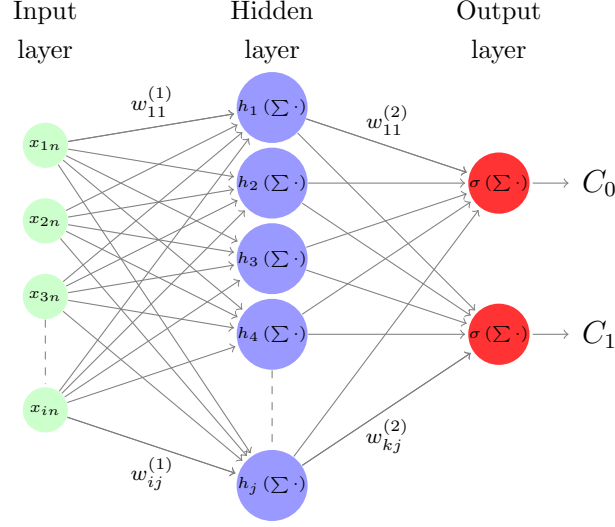


Figure 19: Representation of a neural network of the multilayer perceptron family.

A graphical representation of this network is presented in Fig. 19. Relating Fig. 19 with Eq. (75), it can be noted that this network is composed of some successive non-linear mapping of the input data. First, a linear combination of the input vector  $\mathbf{x}_i$  is performed into some hidden units through a set of weights  $w_{ij}^{(1)}$ . This combination becomes non-linear by the use of the activation function  $h(\cdot)$  which is usually chosen to be a sigmoid function. Then, a linear combination of these hidden units is performed into the output of the neural network through a set of weights  $w_{kj}^{(2)}$ . This combination is also mapped non-linearly using an activation function  $\sigma(\cdot)$  which is usually a logistic function.

Thus, the training of such a network resides in finding the best weights  $w_{ij}^{(1)}$  and  $w_{kj}^{(2)}$  which will model our data the best. The error of this model can be computed such that:

$$E(w_{ij}^{(1)}, w_{kj}^{(2)}) = \frac{1}{2} \sum_{n=1}^N \left( C(\mathbf{x}_n, w_{ij}^{(1)}, w_{kj}^{(2)}) - y(\mathbf{x}_n) \right)^2, \quad (76)$$

where  $\mathbf{x}_n|n = \{1, \dots, N\}$  are the  $N$  training vectors with their corresponding class label  $y(\mathbf{x}_n)$ .

Thus the best set of weights can be inferred in an optimization framework

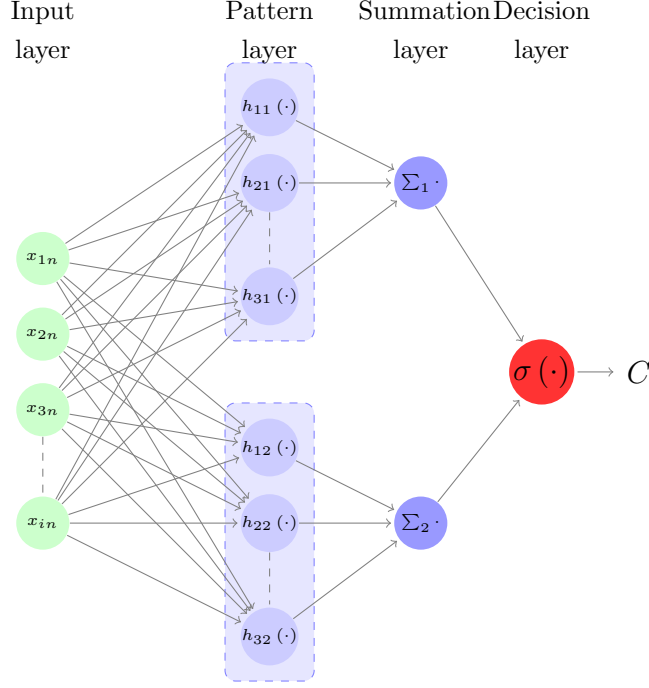


Figure 20: Representation of a neural network of the probabilistic neural network family.

such that:

$$\arg \min_{w_{ij}^{(1)}, w_{kj}^{(2)}} E(w_{ij}^{(1)}, w_{kj}^{(2)}) . \quad (77)$$

This optimization can be performed using a gradient descent method where the derivative of Eq. (76) can be computed using the backpropagation algorithm proposed by Rumelhart et al. (1988).

Matulewicz et al. (2013), Parfait et al. (2012) used this method to classify MRSI spectra.

Probabilistic neural networks are another type of feed-forward networks which can be derived from the multilayer perceptron case and was proposed by Specht (1988). This classifier can be modelled by changing the activation function  $h(\cdot)$  in Eq. (75) to an exponential function such that:

$$h(\mathbf{x}_n) = \exp \left( -\frac{(\mathbf{w}_j - \mathbf{x})^T (\mathbf{w}_j - \mathbf{x})}{2\sigma^2} \right) , \quad (78)$$

where  $\sigma$  is a free parameter.

The other difference of the probabilistic neural network with the multilayer perceptron resides in the architecture as shown in Fig. 20. This network is formed by two hidden layers. The first hidden layer corresponds to the pattern layer which is the mapping done using Eq. (78). This pattern layer is sub-divided into groups corresponding to the class. The second hidden layer corresponds to the summation layer which simply sums the output of each sub-group of the pattern layer. This method was used by Ampeliotis et al. (2007, 2008), Viswanath et al. (2011) in order to perform the classification of their feature vector.

– **Graphical model classifiers:**

Markov random fields can also be used as a lesion segmentation method to detect CaP. First, we can define  $s$  as a pixel which will belong to a certain class denoted by  $\omega_s$ . The labelling process can be noted as  $\omega = \{\omega_s, s \in I\}$  where  $I$  is the set of all the pixels inside the image. The observations corresponding to SI in the image are noted  $\mathcal{F} = \{f_s | s \in I\}$ . Thus, the image process  $\mathcal{F}$  represents the deviation from the labelling process  $\omega$  (Kato and Pong (2001)). Hence, lesion segmentation is equivalent to estimate to estimating the best  $\hat{\omega}$  which maximizes the posterior probability  $p(\omega | \mathcal{F})$ . Thus, using a Bayesian approach, this can be formulated such that:

$$p(\omega | \mathcal{F}) = \arg \max_{\omega} \prod_{s \in I} p(f_s | \omega_s) p(\omega) . \quad (79)$$

It is generally assumed that  $p(f_s | \omega_s)$  follows a Gaussian distribution and that the pixels classes  $\lambda = \{1, 2\}$  for a binary classification will be characterized by their respective mean  $\mu_\lambda$  and standard deviation  $\sigma_\lambda$ . Then,  $\omega$  is supposed to be a Markov random field thus:

$$p(\omega) = \frac{1}{Z} \exp(-U(\omega)) , \quad (80)$$

where  $Z$  is a normalization factor to obtain a probability value,  $U(\cdot)$  is the energy function.

Thus the segmentation problem can be solved as an optimization problem where the energy function  $U(\cdot)$  has to be minimized. There are different possibilities to define the energy function  $U(\cdot)$ . However, this is common to define the energy function such that it combines two type of potential function: (i) a local term relative to the pixel itself and (ii) a smoothing prior which embeds neighbourhood information which will more or less penalizes the energy function to obtain more or less homogeneous region. This optimization of such function

Table 13: Overview of the model validation techniques used in CAD systems.

Model validation techniques	References
LOOCV	[1-8,11,17-21,23,25,32,36,38-40]
$k$ -CV	[10,22,28-32,37,35,41]

can be performed with an algorithm such as iterated conditional modes (Kato and Pong (2001)).

Liu et al. (2009), Ozer et al. (2010) used Markov random fields as an unsupervised method to segment lesions in multi-parametric MRI images.

Artan et al. (2010, 2009) used conditional random fields instead of Markov random fields to segment their MRI images. The difference between these two methods reside in the fact that conditional probabilities are used such as:

$$p(\omega|\mathcal{F}) = \frac{1}{Z} \exp \left[ - \sum_{s \in I} V_{C1}(\omega_s|\mathcal{F}) - \sum_{\{s,r\} \in C} V_{C2}(\omega_s, \omega_r|\mathcal{F}) \right]. \quad (81)$$

$V_{C1}(\cdot)$  is the state (or partition) feature function and  $V_{C2}(\cdot)$  is the transition (or edge) feature function (Kato and Zerubia (2012)).

#### 4.4.2. Model validation

In pattern recognition, the use of model validation techniques to assess the performance of trained classifiers is quite important. Two techniques are broadly used in the development of CAD system and are summarized in Tab. 13.

The most popular technique used in CAD systems (see Tab. 13) is the leave-one-out cross-validation (LOOCV) technique. From the whole data, one patient is kept to validate and the other cases are used to train. This manipulation is repeated until each patient is used for validation. This technique is popular when working with medical data due to the restricted number of patients included in datasets. Thus, it allows to train on a fair number of patients even with a small dataset. However, this technique suffer from high variance and can considered as a non reliable estimate (Efron (1983)).

The other very well known technique used for assessing classifier is the  $k$ -fold cross-validation ( $k$ -CV) technique. This technique is based on splitting the dataset into  $k$  subsets where the samples are randomly selected. Then, one fold is kept for the validation and the remaining subsets for training. The classification is then repeated

Table 14: Overview of the evaluation metrics used in CAD systems.

Evaluation metrics	References
Accuracy	[4-5,12,25,31]
Sensitivity - Specificity	[4-5,7,12,14,17,20-23,25,27-28,33-34]
ROC - AUC	[2-3,6-9,13-19,23,29-32,35-40]
FROC	[10-11,41]
Dice's coefficient	[4-5,12,20]

as in the LOOCV technique. In our review, the typical values used for  $k$  were set to three and five. This technique is more appropriate than the previous one since that it does not suffer from large variance. However, the number of patients in the dataset needs to be large enough to apply such technique.

#### 4.4.3. Evaluation measure

Several metrics can be used in order to assess the performance of the classifier trained when tested on the test data. The techniques used for evaluation of the CAD system for CaP detection are summarized in Tab. 14.

Using the classification approach previously presented, each voxel in the MRI image will be classified into a class. Comparison with a ground-truth can give rise to a confusion matrix by counting true positive, true negative, false positive and false negative samples. From this analysis, different statistics can be extracted.

The first statistic used is the accuracy which computes the ratio of true detection over the number of samples. However, depending on the strategy employed in the CAD work-flow, this statistic can be highly biased by a high number of true negative samples which will boost the accuracy score and does not represent the actual performance of the classifier.

That is why, the most common statistic computed are sensitivity and specificity which are giving a full overview of the performance of the classifier trained. Sensitivity is also called the true positive rate and is equal to the ratio of the true positive samples over the true positive added with the false negative samples. Specificity is also named the true negative rate and is equal to the ratio of the true negative samples over the true negative added with the false positive samples.

These both statistics gave rise to the receiver operating characteristic (ROC)

analysis. This analysis represents graphically the sensitivity as a function of (1 - specificity), which is in fact the false positive rate, by varying the discriminative threshold of the classifier. By varying this threshold, more true negative samples will be found but at the cost to detect also more false negative. However, this fact is interesting in CAD since that it could be possible to obtain a high sensitivity and to ensure that no cancers were missed even if more false alarm will have to be investigated. A statistic derive from ROC analysis is the area under the curve (AUC) which corresponds to the area under the ROC and is a measure used to make comparison between models.

The previous method could have been classified on pixel-based evaluation method. However, a cancer can be also considered as a region. Free-response receiver operating characteristic (FROC) extends the ROC analysis but at region-based level. The same confusion matrix can be computed were the sample are not pixels any more but refer to a lesion. However, this is important to define what is a true positive sample in that case. Usually, a lesion is considered as a true positive sample if the region detected by the classifier and the one inside the ground-truth are overlapping “enough”. “Enough” is defined by each researcher and can correspond to one pixel only!!!

Finally, Dice’s coefficient is sometimes computed which is corresponding to the similarity of a lesion between the ground-truth and the output of the classifier. This coefficient corresponds to the ratio of twice the number of pixels in common over the sum of the pixels of the lesions in the ground-truth and the output of the classifier.

## 5. Discussion

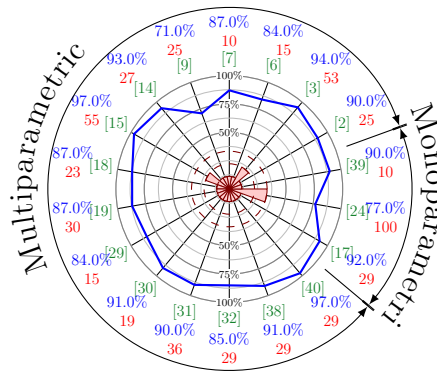
### 5.1. Brief comparison

As discussed previously in Sect. 4.4.3, different metrics have been used to report results. A comparison of the different methods reviewed is given depending on the metric used in each research and also the type of MRI scanner used (cf., 1.5 *versus* 3.0 Tesla). For each research, the experiment obtaining the best result was reported into these figures.

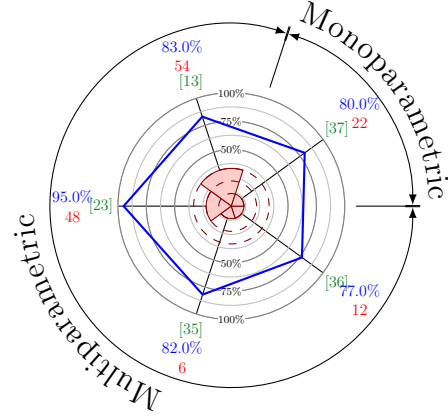
The results given in term of AUC-ROC are depicted in Fig. 21. The results vary between 77% and 95% for some experiments with a 1.5 MRI Tesla scanner and 77% and 95% with a 3.0 Tesla MRI scanner.

The results related with sensitivity and specificity are reported in Fig. 22. In the case that the data were collected with a 1.5 Tesla MRI scanner, the sensitivity is ranging from 74% and 100% and the specificity from 43% and 93%. For the experiments carried out with a 3.0 Tesla MRI scanner, the sensitivity is varying from 60% to 90% and the specificity from 66% to 99%.





(a) Comparison in term of AUC-ROC of the methods using data from 1.5 Tesla MRI scanner.



(b) Comparison in term of AUC-ROC of the methods using data from 3.0 Tesla MRI scanner.

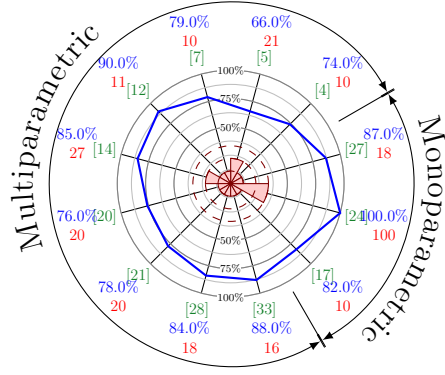
Figure 21: Comparison of the results in term of AUC for 1.5 and 3.0 Tesla MRI scanners. The blue value represents the metric and are graphically reported in the blue curve in the center of the figure. The red value and areas correspond to the number of patients in the dataset. The numbers between brackets in green correspond to the reference as reported in Tab. 2.

Three studies also use FROC analysis to report their results and are shown in Fig. 23. The results are ranging from 65% to 80%

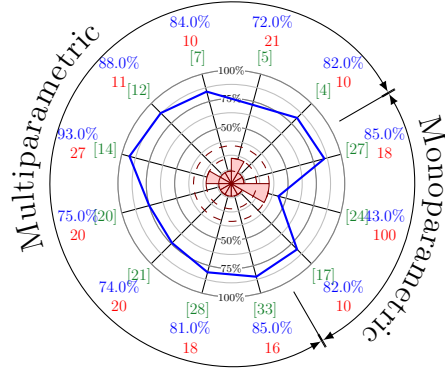
However, we would like to emphasize the fact that the results obtained from these different experiments cannot be fairly compared. Different datasets were used implying different complexity involved and set of input parameter during the data acquisition. To our mind, the only to provide a real and fair comparison would be to provide a common working dataset where those algorithms could be tested.

## 5.2. General discussion

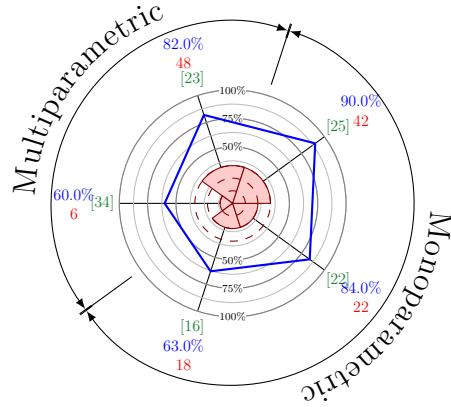
This review leads to some general discussions which could direct to future avenues for research. As previously mentioned, no open multi-parametric dataset is currently available. This fact leads to an impossibility to fairly compare the different algorithms designed over years. Also, the availability of a full multi-parametric dataset (cf., MRI and MRSI), could lead to the development of algorithms which use all the different modalities currently available. Recalling Tab. 2, it can be noted that none of the current works provide a solution using at the same time the four different modalities. We can also mention that all the algorithms are focused on one type of scanner only, either 1.5 Tesla and 3.0 Tesla. A dataset including both these types of imaging could allow to develop more generic algorithms.



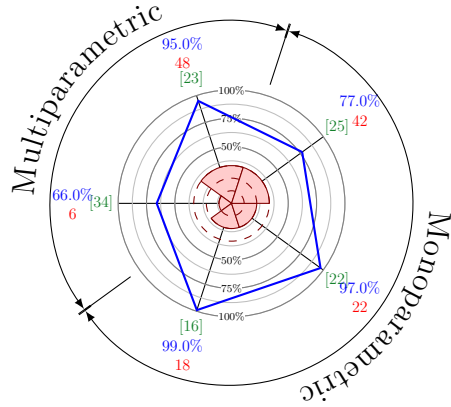
(a) Comparison in term of sensitivity of the methods using data from 1.5 Tesla MRI scanner.



(b) Comparison in term of specificity of the methods using data from 1.5 Tesla MRI scanner.



(c) Comparison in term of sensitivity of the methods using data from 3.0 Tesla MRI scanner.



(d) Comparison in term of specificity of the methods using data from 3.0 Tesla MRI scanner.

Figure 22: Comparison of the results in term of sensitivity (22(a),22(c)) and specificity (22(b),22(d)) for 1.5 and 3.0 Tesla MRI scanners. The blue value represents the metric and are graphically reported in the blue curve in the center of the figure. The red value and areas correspond to the number of patients in the dataset. The numbers between brackets in green correspond to the reference as reported in Tab. 2.

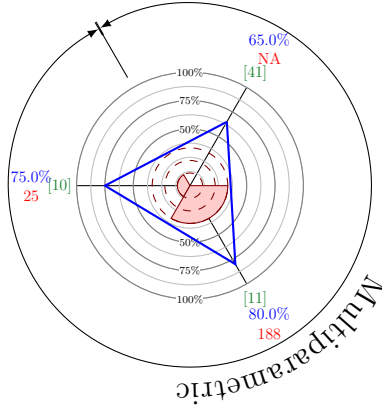


Figure 23: Comparison in term of FROC of the methods using data from 3.0 Tesla MRI scanner. The blue value represent the metric and are graphically reported in the blue curve in the center of the figure. The red value correspond to the number of patients in the dataset and is also reported in the center of the figure. The numbers between brackets correspond to the reference as reported in Tab. 2.

Then, by analysing the different stages of the CAD work-flow, it can be noticed that the actual CAD systems do not include all the different pre-processing steps. It could be interesting to evaluate the improvement using these pre-processing steps on the final results obtained after the classification. Regarding segmentation and registration of the prostate, CAD systems could highly benefit from specific research in these areas which could lead to a better automation of those system. Moreover, other methods specific to segmentation and registration which are not actually used in CAD systems could also perform better than the one currently used in CADs.

Regarding the classification framework, it seems that the current well-known pattern recognition methods have been widely studied. However, more investigations should be carried out regarding the feature detection stage. Lately, histogram-based features have shown good capabilities in the field of computer vision and could be further investigated. Only one study by Liu et al. (2013) used some of these features.

An important point allowing a fair comparison between methods resides in the fact that no universal evaluation model and metric has been defined by the research community allowing such comparison. Usually, it is quite common to choose an evaluation model which fits the dataset limitations, usually the size. Regarding the evaluation, the community would benefit from settling a standard metric which fairly represents the most performance of the algorithms designed.

Finally, we would like to focus the intention of the reader on the availability of a multi-parametric dataset from 1.5 and 3.0 Tesla MRI provided by the authors

of this review. This dataset can be available at the following webpage address:  
<http://visor.udg.edu/dataset>. The dataset is composed of the four modalities  
discussed in this review with the corresponding ground-truth.

## 6. Conclusion

This review presented an overview and gave a staging of the research related  
to CAD development for CaP using multi-parametric MRI and MRSI data. We  
aimed at providing background information regarding multi-parametric MRI imaging  
techniques. A work-flow describing the CAD stages were proposed. The methods  
used in the literature for each of this stage were reviewed. The results of the available  
CAD systems were briefly reviewed. Subsequently, an insight discussion were given  
to conclude this survey.

## 7. Acknowledgement

G. Lemaître was supported by the Generalitat de Catalunya (grant nb. FI-DGR2012) and partly by the Mediterranean Office for Youth (grant nb. 2011/018/06).

We would like to acknowledge Sharad Nagappa for all the discussions involved and  
his precious advices and corrections regarding the redaction of this entire manuscript.

We would like also to thank the Clinica Girona (Catalunya, Espanya) and the  
Centre Hospitalier of Dijon (France) for providing the MRI images used in this  
review.

## References

- Agalliu, I., Gern, R., Leanza, S., Burk, R.D., 2009. Associations of high-grade  
prostate cancer with BRCA1 and BRCA2 founder mutations. *Clin. Cancer Res.*  
15, 1112–1120.
- Ahmed, N., Natarajan, T., Rao, K., 1974. Discrete cosine transform. *Computers,*  
*IEEE Transactions on C-23*, 90–93.
- Aizerman, M.A., Braverman, E.A., Rozonoer, L., 1964. Theoretical foundations of  
the potential function method in pattern recognition learning, in: *Automation and*  
*Remote Control*, pp. 821–837.
- Akin, O., Sala, E., Moskowitz, C.S., Kuroiwa, K., Ishill, N.M., Pucar, D., Scardino,  
P.T., Hricak, H., 2006. Transition zone prostate cancers: features, detection,  
localization, and staging at endorectal MR imaging. *Radiology* 239, 784–792.

- 1936 Alexander, D.D., Mink, P.J., Cushing, C.A., Scurman, B., 2010. A review and  
1937 meta-analysis of prospective studies of red and processed meat intake and prostate  
1938 cancer. *Nutr J* 9, 50.
- 1939 Amadasun, M., King, R., 1989. Textural features corresponding to textural proper-  
1940 ties. *Systems, Man and Cybernetics, IEEE Transactions on* 19, 1264–1274.
- 1941 American Cancer Society, A.C., 2010. Cancer Facts and Figures 2010.  
1942 <http://www.cancer.org/research/cancerfactsfigures>. URL: <http://www.cancer.org/research/cancerfactsfigures>. accessed: 2013-08-01.
- 1943
- 1944 American Cancer Society, A.C., 2013. Cancer Facts and Figures 2013.  
1945 <http://www.cancer.org/research/cancerfactsfigures>. Accessed: 2013-08-01.
- 1946 Ampeliotis, D., Anonakoudi, A., Berberidis, K., Psarakis, E.Z., 2007. Computer  
1947 aided detection of prostate cancer using fused information from dynamic contrast  
1948 enhanced and morphological magnetic resonance images, in: *IEEE International  
1949 Conference on Signal Processing and Communications*, pp. 888–891.
- 1950 Ampeliotis, D., Anonakoudi, A., Berberidis, K., Psarakis, E.Z., Kounoudes, A., 2008.  
1951 A computer-aided system for the detection of prostate cancer based on magnetic  
1952 resonance image analysis, in: *International Symposium on Communications, Con-  
1953 trol and Signal Processing*.
- 1954 Amundadottir, L.T., Sulem, P., Gudmundsson, J., Helgason, A., Baker, A., Agnars-  
1955 son, B.A., Sigurdsson, A., Benediktsdottir, K.R., Cazier, J.B., Sainz, J., Jakobs-  
1956 dottir, M., Kostic, J., Magnusdottir, D.N., Ghosh, S., Agnarsson, K., Birgisdot-  
1957 tir, B., Le Roux, L., Olafsdottir, A., Blondal, T., Andresdottir, M., Gretarsdot-  
1958 tir, O.S., Bergthorsson, J.T., Gudbjartsson, D., Gylfason, A., Thorleifsson, G.,  
1959 Manolescu, A., Kristjansson, K., Geirsson, G., Isaksson, H., Douglas, J., Johans-  
1960 son, J.E., Balter, K., Wiklund, F., Montie, J.E., Yu, X., Suarez, B.K., Ober, C.,  
1961 Cooney, K.A., Gronberg, H., Catalona, W.J., Einarsson, G.V., Barkardottir, R.B.,  
1962 Gulcher, J.R., Kong, A., Thorsteinsdottir, U., Stefansson, K., 2006. A common  
1963 variant associated with prostate cancer in European and African populations. *Nat.  
1964 Genet.* 38, 652–658.
- 1965 Andriole, G.L., Crawford, E.D., Grubb, R.L., Buys, S.S., Chia, D., Church, T.R.,  
1966 Fouad, M.N., Gelmann, E.P., Kvale, P.A., Reding, D.J., Weissfeld, J.L., Yokochi,  
1967 L.A., O'Brien, B., Clapp, J.D., Rathmell, J.M., Riley, T.L., Hayes, R.B., Kramer,  
1968 B.S., Izmirlian, G., Miller, A.B., Pinsky, P.F., Prorok, P.C., Gohagan, J.K., Berg,

- 1969 C.D., 2009. Mortality results from a randomized Prostate-cancer screening trial.  
1970 New England Journal of Medicine 360, 1310–1319.
- 1971 Antic, T., Peng, Y., Jiang, Y., Giger, M.L., Eggener, S., Oto, A., 2013. A study of  
1972 T2-weighted MR image texture features and diffusion-weighted MR image features  
1973 for computer-aided diagnosis of prostate cancer, in: Proc. SPIE 8670, Medical  
1974 Imaging 2013: Computer-Aided Diagnosis, pp. 86701H–86701H–6.
- 1975 Artan, Y., Haider, M.A., Langer, D.L., van der Kwast, T.H., Evans, A.J., Yang, Y.,  
1976 Wernick, M.N., Trachtenberg, J., Yetik, I.S., 2010. Prostate cancer localization  
1977 with multispectral MRI using cost-sensitive support vector machines and condi-  
1978 tional random fields. IEEE Trans Image Process 19, 2444–2455.
- 1979 Artan, Y., Langer, D., Haider, M., Van der Kwast, T.H., Evans, A., Wernick, M.,  
1980 Yetik, I., 2009. Prostate cancer segmentation with multispectral MRI using cost-  
1981 sensitive Conditional Random Fields, in: Biomedical Imaging: From Nano to  
1982 Macro, 2009. ISBI '09. IEEE International Symposium on, pp. 278–281.
- 1983 Awwad, H.M., Geisel, J., Obeid, R., 2012. The role of choline in prostate cancer.  
1984 Clin. Biochem. 45, 1548–1553.
- 1985 Barentsz, J.O., Richenberg, J., Clements, R., Choyke, P., Verma, S., Villeirs, G.,  
1986 Rouviere, O., Logager, V., Futterer, J.J., 2012. ESUR prostate MR guidelines  
1987 2012. Eur Radiol 22, 746–757.
- 1988 Belkin, M., Niyogi, P., 2001. Laplacian eigenmaps and spectral techniques for em-  
1989 bedding and clustering, in: Advances in Neural Information Processing Systems  
1990 14, MIT Press. pp. 585–591.
- 1991 Belongie, S., Malik, J., Puzicha, J., 2002. Shape matching and object recognition us-  
1992 ing shape contexts. Pattern Analysis and Machine Intelligence, IEEE Transactions  
1993 on 24, 509–522.
- 1994 Benassi, A., Cohen, S., Istat, J., 1998. Identifying the multifractional function of a  
1995 Gaussian process. Statistics & Probability Letters 39, 337 – 345.
- 1996 Bishop, C.M., 2006. Pattern recognition and machine learning. Springer-Verlag New  
1997 York, Inc., Secaucus, NJ, USA.
- 1998 Bookstein, F.L., 1989. Principal warps: thin-plate splines and the decomposition of  
1999 deformations. Pattern Analysis and Machine Intelligence, IEEE Transactions on  
2000 11, 567–585.

- 2001 Boser, B.E., Guyon, I.M., Vapnik, V.N., 1992. A training algorithm for optimal mar-  
2002 gin classifiers, in: Proceedings of the Fifth Annual Workshop on Computational  
2003 Learning Theory, ACM, New York, NY, USA. pp. 144–152.
- 2004 Bourdounis, A., Papatsoris, A.G., Chrisofos, M., Efstathiou, E., Skolarikos, A.,  
2005 Deliveliotis, C., 2010. The novel prostate cancer antigen 3 (PCA3) biomarker. *Int*  
2006 *Braz J Urol* 36, 665–668.
- 2007 Breiman, L., 2001. Random forests. *Machine Learning* 45, 5–32.
- 2008 Breiman, L., Friedman, J., Olshen, R., Stone, C., 1984. Classification and regression  
2009 trees. Wadsworth and Brooks, Monterey, CA.
- 2010 Brenner, J., Chinnaiyan, A., Tomlins, S., 2013. ETS fusion genes in prostate cancer,  
2011 in: Tindall, D.J. (Ed.), *Prostate Cancer*. Springer New York. volume 16 of *Protein*  
2012 *Reviews*, pp. 139–183.
- 2013 Buades, A., Coll, B., Morel, J., 2005. A review of image denoising algorithms, with  
2014 a new one. *Simul* 4, 490–530.
- 2015 Buckley, D.L., Roberts, C., Parker, G.J., Logue, J.P., Hutchinson, C.E., 2004.  
2016 Prostate cancer: evaluation of vascular characteristics with dynamic contrast-  
2017 enhanced T1-weighted MR imaging—initial experience. *Radiology* 233, 709–715.
- 2018 Byrd, R.H., Lu, P., Nocedal, J., Zhu, C., 1995. A limited memory algorithm for  
2019 bound constrained optimization. *SIAM J. Sci. Comput.* 16, 1190–1208.
- 2020 Carmeliet, P., Jain, R.K., 2000. Angiogenesis in cancer and other diseases. *Nature*  
2021 407, 249–257.
- 2022 Carrol, C.L., Sommer, F.G., McNeal, J.E., Stamey, T.A., 1987. The abnormal  
2023 prostate: MR imaging at 1.5 T with histopathologic correlation. *Radiology* 163,  
2024 521–525.
- 2025 Castorina, P., Delsanto, P.P., Guiot, C., 2006. Classification scheme for phenom-  
2026 ological universalities in growth problems in physics and other sciences. *Phys. Rev.*  
2027 *Lett.* 96, 188701.
- 2028 Chan, H.P., Doi, K., Galhotra, S., Vyborny, C.J., MacMahon, H., Jokich, P.M.,  
2029 1987. Image feature analysis and computer-aided diagnosis in digital radiography.  
2030 I. Automated detection of microcalcifications in mammography. *Med Phys* 14,  
2031 538–548.

2032 Chan, H.P., Hadjiiski, L., Zhou, C., Sahiner, B., 2008. Computer-aided diagnosis of  
2033 lung cancer and pulmonary embolism in computed tomography-a review. *Acad*  
2034 *Radiol* 15, 535–555.

2035 Chan, H.P., Sahiner, B., Helvie, M.A., Petrick, N., Roubidoux, M.A., Wilson, T.E.,  
2036 Adler, D.D., Paramagul, C., Newman, J.S., Sanjay-Gopal, S., 1999. Improvement  
2037 of radiologists' characterization of mammographic masses by using computer-aided  
2038 diagnosis: an ROC study. *Radiology* 212, 817–827.

2039 Chan, I., Wells, W., Mulkern, R.V., Haker, S., Zhang, J., Zou, K.H., Maier, S.E.,  
2040 Tempany, C.M., 2003. Detection of prostate cancer by integration of line-scan dif-  
2041 fusion, T2-mapping and T2-weighted magnetic resonance imaging; a multichannel  
2042 statistical classifier. *Med Phys* 30, 2390–2398.

2043 Chappelow, J., Bloch, B.N., Rofsky, N., Genega, E., Lenkinski, R., DeWolf, W.,  
2044 Madabhushi, A., 2011. Elastic registration of multimodal prostate MRI and his-  
2045 tology via multiattribute combined mutual information. *Med Phys* 38, 2005–2018.

2046 Chen, L., Weng, Z., Goh, L., Garland, M., 2002. An efficient algorithm for automatic  
2047 phase correction of {NMR} spectra based on entropy minimization . *Journal of*  
2048 *Magnetic Resonance* 158, 164 – 168.

2049 Cheng, H.D., Shan, J., Ju, W., Guo, Y., Zhang, L., 2010. Automated breast cancer  
2050 detection and classification using ultrasound images: A survey. *Pattern Recogn.*  
2051 43, 299–317.

2052 Choi, Y.J., Kim, J.K., Kim, N., Kim, K.W., Choi, E.K., Cho, K.S., 2007. Functional  
2053 MR imaging of prostate cancer. *Radiographics* 27, 63–75.

2054 Chou, R., Croswell, J.M., Dana, T., Bougatsos, C., Blazina, I., Fu, R., Gleitsmann,  
2055 K., Koenig, H.C., Lam, C., Maltz, A., Rugge, J.B., Lin, K., 2011. Screening for  
2056 prostate cancer: a review of the evidence for the U.S. Preventive Services Task  
2057 Force. *Ann. Intern. Med.* 155, 762–771.

2058 Coakley, F.V., Hricak, H., 2000. Radiologic anatomy of the prostate gland: a clinical  
2059 approach. *Radiol. Clin. North Am.* 38, 15–30.

2060 Cohen, R.J., Shannon, B.A., Phillips, M., Moorin, R.E., Wheeler, T.M., Garrett,  
2061 K.L., 2008. Central zone carcinoma of the prostate gland: a distinct tumor type  
2062 with poor prognostic features. *J. Urol.* 179, 1762–1767.



- 2063 Coifman, R., Wickerhauser, M., 1992. Entropy-based algorithms for best basis se-  
2064 lection. *Information Theory, IEEE Transactions on* 38, 713–718.
- 2065 Coleman, T., Li, Y., 1993. An interior trust region approach for nonlinear minimiza-  
2066 tion subject to bounds. Technical Report. Cornell University.
- 2067 Cootes, T.F., Taylor, C.J., Cooper, D.H., Graham, J., 1995. Active shape mod-  
2068 els—Their training and application. *Comput. Vis. Image Underst.* 61, 38–  
2069 59.
- 2070 Cortes, C., Vapnik, V., 1995. Support-Vector networks. *Machine Learning* 20, 273–  
2071 297.
- 2072 Costello, L.C., Franklin, R.B., 2006. The clinical relevance of the metabolism of  
2073 prostate cancer; zinc and tumor suppression: connecting the dots. *Mol. Cancer* 5,  
2074 17.
- 2075 Cruz, M., Tsuda, K., Narumi, Y., Kuroiwa, Y., Nose, T., Kojima, Y., Okuyama, A.,  
2076 Takahashi, S., Aozasa, K., Barentsz, J.O., Nakamura, H., 2002. Characterization  
2077 of low-intensity lesions in the peripheral zone of prostate on pre-biopsy endorectal  
2078 coil MR imaging. *Eur Radiol* 12, 357–365.
- 2079 Dalal, N., Triggs, B., 2005. Histograms of oriented gradients for human detection,  
2080 in: *Computer Vision and Pattern Recognition, 2005. CVPR 2005. IEEE Computer*  
2081 *Society Conference on*, pp. 886–893 vol. 1.
- 2082 Daugman, J.G., 1985. Uncertainty relation for resolution in space, spatial frequency,  
2083 and orientation optimized by two-dimensional visual cortical filters. *J Opt Soc*  
2084 *Am A* 2, 1160–1169.
- 2085 Dean, J.C., Ilvento, C.C., 2006. Improved cancer detection using computer-aided  
2086 detection with diagnostic and screening mammography: prospective study of 104  
2087 cancers. *AJR Am J Roentgenol* 187, 20–28.
- 2088 Delongchamps, N.B., Peyromaure, M., Schull, A., Beuvon, F., Bouazza, N., Flam,  
2089 T., Zerbib, M., Muradyan, N., Legman, P., Cornud, F., 2013. Prebiopsy magnetic  
2090 resonance imaging and prostate cancer detection: comparison of random and tar-  
2091 geted biopsies. *J. Urol.* 189, 493–499.
- 2092 Delpierre, C., Lamy, S., Kelly-Irving, M., Molinie, F., Velten, M., Tretarre, B.,  
2093 Woronoff, A.S., Buemi, A., Lapotre-Ledoux, B., Bara, S., Guizard, A.V., Colonna,

2094 M., Grosclaude, P., 2013. Life expectancy estimates as a key factor in over-  
2095 treatment: the case of prostate cancer. *Cancer Epidemiol* 37, 462–468.

2096 Devos, A., Lukas, L., Suykens, J.A., Vanhamme, L., Tate, A.R., Howe, F.A., Majos,  
2097 C., Moreno-Torres, A., van der Graaf, M., Arus, C., Van Huffel, S., 2004. Classi-  
2098 fication of brain tumours using short echo time 1H MR spectra. *J. Magn. Reson.*  
2099 170, 164–175.

2100 Doi, K., Chan, H.P., Giger, M., 1990. Method and system for enhancement and  
2101 detection of abnormal anatomic regions in a digital image.

2102 Donoho, D.L., Johnstone, J.M., 1994. Ideal spatial adaptation by wavelet shrinkage.  
2103 *Biometrika* 81, 425–455.

2104 Doo, K.W., Sung, D.J., Park, B.J., Kim, M.J., Cho, S.B., Oh, Y.W., Ko, Y.H., Yang,  
2105 K.S., 2012. Detectability of low and intermediate or high risk prostate cancer with  
2106 combined T2-weighted and diffusion-weighted MRI. *Eur Radiol* 22, 1812–1819.

2107 Efron, B., 1979. Bootstrap methods: Another look at the jackknife. *The Annals of*  
2108 *Statistics* 7, 1–26.

2109 Efron, B., 1983. Estimating the error rate of a prediction rule: Improvement on  
2110 cross-validation. *Journal of the American Statistical Association* 78, pp. 316–331.

2111 Elter, M., Horsch, A., 2009. CADx of mammographic masses and clustered micro-  
2112 calcifications: a review. *Med Phys* 36, 2052–2068.

2113 Epstein, J.I., Allsbrook, W.C., Amin, M.B., Egevad, L.L., 2005. The 2005 Interna-  
2114 tional Society of Urological Pathology (ISUP) Consensus Conference on Gleason  
2115 Grading of Prostatic Carcinoma. *Am. J. Surg. Pathol.* 29, 1228–1242.

2116 Etzioni, R., Penson, D.F., Legler, J.M., di Tommaso, D., Boer, R., Gann, P.H., Feuer,  
2117 E.J., 2002. Overdiagnosis due to prostate-specific antigen screening: lessons from  
2118 U.S. prostate cancer incidence trends. *J. Natl. Cancer Inst.* 94, 981–990.

2119 Ferlay, J., Shin, H.R., Bray, F., Forman, D., Mathers, C., Parkin, D.M., 2010. Esti-  
2120 mates of worldwide burden of cancer in 2008: GLOBOCAN 2008. *Int. J. Cancer*  
2121 127, 2893–2917.

2122 Fodor, I., 2002. A survey of dimension reduction techniques.

2123 Fred, A., Jain, A., 2005. Combining multiple clusterings using evidence accumula-  
 2124 tion. *Pattern Analysis and Machine Intelligence, IEEE Transactions on* 27, 835–  
 2125 850.

2126 Freedman, M.L., Haiman, C.A., Patterson, N., McDonald, G.J., Tandon, A., Wal-  
 2127 iszewska, A., Penney, K., Steen, R.G., Ardlie, K., John, E.M., Oakley-Girvan, I.,  
 2128 Whittmore, A.S., Cooney, K.A., Ingles, S.A., Altshuler, D., Henderson, B.E., Re-  
 2129 ich, D., 2006. Admixture mapping identifies 8q24 as a prostate cancer risk locus  
 2130 in African-American men. *Proc. Natl. Acad. Sci. U.S.A.* 103, 14068–14073.

2131 Freund, Y., Schapire, R., 1997. A decision-theoretic generalization of on-line learning  
 2132 and an application to boosting. *Journal of Computer and System Sciences* 55, 119  
 2133 – 139.

2134 Friedman, J., 1989. Regularized discriminant analysis. *Journal of the American*  
 2135 *Statistical Association* 84, pp. 165–175.

2136 Gabor, D., 1946. Theory of communication. Part 1: The analysis of information.  
 2137 *Electrical Engineers - Part III: Radio and Communication Engineering, Journal of*  
 2138 *the Institution of* 93, 429–441.

2139 Ghose, S., Oliver, A., Marti, R., Llado, X., Vilanova, J.C., Freixenet, J., Mitra, J.,  
 2140 Sidibe, D., Meriaudeau, F., 2012. A survey of prostate segmentation methodologies  
 2141 in ultrasound, magnetic resonance and computed tomography images. *Comput*  
 2142 *Methods Programs Biomed* 108, 262–287.

2143 Giannini, V., Vignati, A., Mazzetti, S., De Luca, M., Bracco, C., Stasi, M., Russo, F.,  
 2144 Armando, E., Regge, D., 2013. A prostate CAD system based on multiparametric  
 2145 analysis of DCE T1-w, and DW automatically registered images, in: *Proc. SPIE*  
 2146 8670, *Medical Imaging 2013: Computer-Aided Diagnosis*, pp. 86703E–86703E–6.

2147 Gibbs, P., Tozer, D.J., Liney, G.P., Turnbull, L.W., 2001. Comparison of quantitative  
 2148 T2 mapping and diffusion-weighted imaging in the normal and pathologic prostate.  
 2149 *Magn Reson Med* 46, 1054–1058.

2150 Giger, M.L., Chan, H.P., Boone, J., 2008. Anniversary paper: History and status  
 2151 of CAD and quantitative image analysis: the role of Medical Physics and AAPM.  
 2152 *Med Phys* 35, 5799–5820.

2153 Giger, M.L., Doi, K., MacMahon, H., 1988. Image feature analysis and computer-  
 2154 aided diagnosis in digital radiography. 3. Automated detection of nodules in pe-  
 2155 ripheral lung fields. *Med Phys* 15, 158–166.

2156 Giovannucci, E., Liu, Y., Platz, E.A., Stampfer, M.J., Willett, W.C., 2007. Risk  
2157 factors for prostate cancer incidence and progression in the health professionals  
2158 follow-up study. *Int. J. Cancer* 121, 1571–1578.

2159 Giskeodegard, G.F., Bertilsson, H., Selnaes, K.M., Wright, A.J., Bathen, T.F., Viset,  
2160 T., Halgunset, J., Angelsen, A., Gribbestad, I.S., Tessem, M.B., 2013. Spermine  
2161 and citrate as metabolic biomarkers for assessing prostate cancer aggressiveness.  
2162 *PLoS ONE* 8, e62375.

2163 Gleason, D.F., 1977. *Urologic pathology: The prostate*. Lea and Febiger.. chapter  
2164 The Veteran’s Administration Cooperative Urologic Research Group: histologic  
2165 grading and clinical staging of prostatic carcinoma. p. 171198.

2166 Goodman, S.N., 1999. Toward evidence-based medical statistics. 1: The P value  
2167 fallacy. *Ann. Intern. Med.* 130, 995–1004.

2168 van der Graaf, M., Schipper, R.G., Oosterhof, G.O., Schalken, J.A., Verhofstad,  
2169 A.A., Heerschap, A., 2000. Proton MR spectroscopy of prostatic tissue focused on  
2170 the detection of spermine, a possible biomarker of malignant behavior in prostate  
2171 cancer. *MAGMA* 10, 153–159.

2172 Gribbestad, I., Gjesdal, K., Nilsen, G., Lundgren, S., Hjelstuen, M., Jackson, A.,  
2173 2005. An introduction to dynamic contrast-enhanced MRI in oncology, in: Jack-  
2174 son, A., Buckley, D., Parker, G. (Eds.), *Dynamic Contrast-Enhanced Magnetic*  
2175 *Resonance Imaging in Oncology*. Springer Berlin Heidelberg. Medical Radiology,  
2176 pp. 1–22.

2177 Haacke, E., Brown, R., Thompson, M., Venkatesan, R., 1999. *Magnetic resonance*  
2178 *imaging: Physical principles and sequence design*. Wiley.

2179 Haas, G.P., Delongchamps, N.B., Jones, R.F., Chandan, V., Serio, A.M., Vickers,  
2180 A.J., Jumbelic, M., Threatte, G., Korets, R., Lilja, H., de la Roza, G., 2007.  
2181 Needle biopsies on autopsy prostates: sensitivity of cancer detection based on true  
2182 prevalence. *J. Natl. Cancer Inst.* 99, 1484–1489.

2183 Hambrock, T., Somford, D.M., Huisman, H.J., van Oort, I.M., Witjes, J.A.,  
2184 Hulsbergen-van de Kaa, C.A., Scheenen, T., Barentsz, J.O., 2011. Relationship  
2185 between apparent diffusion coefficients at 3.0-T MR imaging and Gleason grade  
2186 in peripheral zone prostate cancer. *Radiology* 259, 453–461.

2187 Hambrock, T., Vos, P.C., Hulsbergen-van de Kaa, C.A., Barentsz, J.O., Huisman,  
2188 H.J., 2013. Prostate cancer: computer-aided diagnosis with multiparametric 3-T  
2189 MR imaging—effect on observer performance. *Radiology* 266, 521–530.

2190 Hara, N., Okuizumi, M., Koike, H., Kawaguchi, M., Bilim, V., 2005. Dynamic  
2191 contrast-enhanced magnetic resonance imaging (DCE-MRI) is a useful modality  
2192 for the precise detection and staging of early prostate cancer. *Prostate* 62, 140–147.

2193 Haralick, R., Shanmugam, K., Dinstein, I., 1973. Textural features for image classi-  
2194 fication. *Systems, Man and Cybernetics, IEEE Transactions on SMC-3*, 610–621.

2195 Hegde, J.V., Mulkern, R.V., Panych, L.P., Fennessy, F.M., Fedorov, A., Maier,  
2196 S.E., Tempany, C.M., 2013. Multiparametric MRI of prostate cancer: an update  
2197 on state-of-the-art techniques and their performance in detecting and localizing  
2198 prostate cancer. *J Magn Reson Imaging* 37, 1035–1054.

2199 Heidenreich, A., Abrahamsson, P.A., Artibani, W., Catto, J., Montorsi, F., Van Pop-  
2200 pel, H., Wirth, M., Mottet, N., 2013. Early detection of prostate cancer: European  
2201 Association of Urology recommendation. *Eur. Urol.* 64, 347–354.

2202 Hero, A., Ma, B., Michel, O., Gorman, J., 2002. Applications of entropic spanning  
2203 graphs. *Signal Processing Magazine, IEEE* 19, 85–95.

2204 Hoeks, C.M., Barentsz, J.O., Hambrock, T., Yakar, D., Somford, D.M., Heijmink,  
2205 S.W., Scheenen, T.W., Vos, P.C., Huisman, H., van Oort, I.M., Witjes, J.A.,  
2206 Heerschap, A., Futterer, J.J., 2011. Prostate cancer: multiparametric MR imaging  
2207 for detection, localization, and staging. *Radiology* 261, 46–66.

2208 Hoffman, R.M., Gilliland, F.D., Eley, J.W., Harlan, L.C., Stephenson, R.A., Stan-  
2209 ford, J.L., Albertson, P.C., Hamilton, A.S., Hunt, W.C., Potosky, A.L., 2001.  
2210 Racial and ethnic differences in advanced-stage prostate cancer: the Prostate Can-  
2211 cer Outcomes Study. *J. Natl. Cancer Inst.* 93, 388–395.

2212 Hricak, H., Doms, G.C., McNeal, J.E., Mark, A.S., Marotti, M., Avallone, A.,  
2213 Pelzer, M., Proctor, E.C., Tanagho, E.A., 1987. MR imaging of the prostate  
2214 gland: normal anatomy. *AJR Am J Roentgenol* 148, 51–58.

2215 Hricak, H., Williams, R.D., Spring, D.B., Moon, K.L., Hedgcock, M.W., Watson,  
2216 R.A., Crooks, L.E., 1983. Anatomy and pathology of the male pelvis by magnetic  
2217 resonance imaging. *AJR Am J Roentgenol* 141, 1101–1110.

- 2218 Huch Boni, R.A., Boner, J.A., Lutolf, U.M., Trinkler, F., Pestalozzi, D.M., Krestin,  
2219 G.P., 1995. Contrast-enhanced endorectal coil MRI in local staging of prostate  
2220 carcinoma. *J Comput Assist Tomogr* 19, 232–237.
- 2221 Hugosson, J., Carlsson, S., Aus, G., Bergdahl, S., Khatami, A., Lodding, P., Pihl,  
2222 C.G., Stranne, J., Holmberg, E., Lilja, H., 2010. Mortality results from the  
2223 Göteborg randomised population-based prostate-cancer screening trial. *Lancet*  
2224 *Oncol.* 11, 725–732.
- 2225 Huisman, H., Vos, P., Litjens, G., Hambrock, T., Barentsz, J., 2010. Computer aided  
2226 detection of prostate cancer using T2, DWI and DCE MRI: methods and clinical  
2227 applications, in: *Proceedings of the 2010 international conference on Prostate*  
2228 *cancer imaging: computer-aided diagnosis, prognosis, and intervention*, Springer-  
2229 Verlag, Berlin, Heidelberg. pp. 4–14.
- 2230 Huisman, T.A., 2003. Diffusion-weighted imaging: basic concepts and application in  
2231 cerebral stroke and head trauma. *Eur Radiol* 13, 2283–2297.
- 2232 Itou, Y., Nakanishi, K., Narumi, Y., Nishizawa, Y., Tsukuma, H., 2011. Clinical  
2233 utility of apparent diffusion coefficient (ADC) values in patients with prostate  
2234 cancer: can ADC values contribute to assess the aggressiveness of prostate cancer?  
2235 *J Magn Reson Imaging* 33, 167–172.
- 2236 Jager, G.J., Ruijter, E.T., van de Kaa, C.A., de la Rosette, J.J., Oosterhof, G.O.,  
2237 Thornbury, J.R., Ruijs, S.H., Barentsz, J.O., 1997. Dynamic TurboFLASH sub-  
2238 traction technique for contrast-enhanced MR imaging of the prostate: correlation  
2239 with histopathologic results. *Radiology* 203, 645–652.
- 2240 Jolliffe, I.T., 2002. *Principal Component Analysis*. Second ed., Springer.
- 2241 Jungke, M., Von Seelen, W., Bielke, G., Meindl, S., Grigat, M., Pfannenstiel, P.,  
2242 1987. A system for the diagnostic use of tissue characterizing parameters in NMR-  
2243 tomography, in: *Proc. of Information Processing in Medical Imaging*, pp. 471–481.
- 2244 Kaji, Y., Kurhanewicz, J., Hricak, H., Sokolov, D.L., Huang, L.R., Nelson, S.J.,  
2245 Vigneron, D.B., 1998. Localizing prostate cancer in the presence of postbiopsy  
2246 changes on MR images: role of proton MR spectroscopic imaging. *Radiology* 206,  
2247 785–790.
- 2248 Kato, Z., Pong, T., 2001. A Markov random field image segmentation model using  
2249 combined color and texture features, in: Skarbek, W. (Ed.), *Computer Analysis*

- 2250 of Images and Patterns. Springer Berlin Heidelberg. volume 2124 of *Lecture Notes*  
2251 *in Computer Science*, pp. 547–554.
- 2252 Kato, Z., Zerubia, J., 2012. Markov Random Fields in Image Segmentation. Collec-  
2253 tion Foundation and Trends in Signal Processing. Now Editor, World Scientific.
- 2254 Kelm, B.M., Menze, B.H., Zechmann, C.M., Baudendistel, K.T., Hamprecht, F.A.,  
2255 2007. Automated estimation of tumor probability in prostate magnetic resonance  
2256 spectroscopic imaging: pattern recognition vs quantification. *Magn Reson Med*  
2257 57, 150–159.
- 2258 Kety, S., 1951. The theory and applications of the exchange of inert gas at the lungs  
2259 and tissues. *Pharmacol. Rev.* 3, 1–41.
- 2260 Kim, J.K., Hong, S.S., Choi, Y.J., Park, S.H., Ahn, H., Kim, C.S., Cho, K.S.,  
2261 2005. Wash-in rate on the basis of dynamic contrast-enhanced MRI: usefulness for  
2262 prostate cancer detection and localization. *J Magn Reson Imaging* 22, 639–646.
- 2263 Kirkham, A.P., Emberton, M., Allen, C., 2006. How good is MRI at detecting and  
2264 characterising cancer within the prostate? *Eur. Urol.* 50, 1163–1174.
- 2265 Kirsch, R., 1971. Computer determination of the constituent structure of biological  
2266 images . *Computers and Biomedical Research* 4, 315 – 328.
- 2267 Koh, D.M., Collins, D.J., 2007. Diffusion-weighted MRI in the body: applications  
2268 and challenges in oncology. *AJR Am J Roentgenol* 188, 1622–1635.
- 2269 Korotkov, K., Garcia, R., 2012. Computerized analysis of pigmented skin lesions: a  
2270 review. *Artif Intell Med* 56, 69–90.
- 2271 Kurhanewicz, J., Vigneron, D.B., Hricak, H., Narayan, P., Carroll, P., Nelson, S.J.,  
2272 1996. Three-dimensional H-1 MR spectroscopic imaging of the in situ human  
2273 prostate with high (0.24-0.7-cm<sup>3</sup>) spatial resolution. *Radiology* 198, 795–805.
- 2274 Langer, D.L., van der Kwast, T.H., Evans, A.J., Trachtenberg, J., Wilson, B.C.,  
2275 Haider, M.A., 2009. Prostate cancer detection with multi-parametric MRI: logistic  
2276 regression analysis of quantitative T2, diffusion-weighted imaging, and dynamic  
2277 contrast-enhanced MRI. *J Magn Reson Imaging* 30, 327–334.
- 2278 Larsson, H.B., Fritz-Hansen, T., Rostrup, E., Sondergaard, L., Ring, P., Henriksen,  
2279 O., 1996. Myocardial perfusion modeling using MRI. *Magn Reson Med* 35, 716–  
2280 726.

- 2281 Laudadio, T., Mastronardi, N., Vanhamme, L., Hecke, P.V., Huffel, S.V., 2002.  
 2282 Improved Lanczos algorithms for blackbox {MRS} data quantitation. *Journal of*  
 2283 *Magnetic Resonance* 157, 292 – 297.
- 2284 Le Bihan, D., Breton, E., Lallemand, D., Aubin, M.L., Vignaud, J., Laval-Jeantet,  
 2285 M., 1988. Separation of diffusion and perfusion in intravoxel incoherent motion  
 2286 MR imaging. *Radiology* 168, 497–505.
- 2287 Le Bihan, D., Breton, E., Lallemand, D., Grenier, P., Cabanis, E., Laval-Jeantet,  
 2288 M., 1986. MR imaging of intravoxel incoherent motions: application to diffusion  
 2289 and perfusion in neurologic disorders. *Radiology* 161, 401–407.
- 2290 Leissner, K.H., Tisell, L.E., 1979. The weight of the human prostate. *Scand. J. Urol.*  
 2291 *Nephrol.* 13, 137–142.
- 2292 Lemaître, G., 2011. Absolute quantification at 3 T. Master’s thesis. Université de  
 2293 Bourgogne, Heriot-Watt University, Universitat de Girona.
- 2294 Li, F., Aoyama, M., Shiraishi, J., Abe, H., Li, Q., Suzuki, K., Engelmann, R., Sone,  
 2295 S., Macmahon, H., Doi, K., 2004. Radiologists’ performance for differentiating be-  
 2296 nign from malignant lung nodules on high-resolution CT using computer-estimated  
 2297 likelihood of malignancy. *AJR Am J Roentgenol* 183, 1209–1215.
- 2298 Li, H., Giger, M.L., Olopade, O.I., Margolis, A., Lan, L., Chinander, M.R., 2005.  
 2299 Computerized texture analysis of mammographic parenchymal patterns of digi-  
 2300 tized mammograms. *Acad Radiol* 12, 863–873.
- 2301 Li, Q., Sone, S., Doi, K., 2003. Selective enhancement filters for nodules, vessels, and  
 2302 airway walls in two- and three-dimensional CT scans. *Med Phys* 30, 2040–2051.
- 2303 Li, S.Z., 1996. Robustizing robust M-estimation using deterministic annealing. *Pat-*  
 2304 *tern Recognition* 29, 159–166.
- 2305 Lieber, C.A., Mahadevan-Jansen, A., 2003. Automated method for subtraction of  
 2306 fluorescence from biological Raman spectra. *Appl Spectrosc* 57, 1363–1367.
- 2307 Liney, G.P., Knowles, A.J., Manton, D.J., Turnbull, L.W., Blackband, S.J., Hors-  
 2308 man, A., 1996a. Comparison of conventional single echo and multi-echo sequences  
 2309 with a fast spin-echo sequence for quantitative T2 mapping: application to the  
 2310 prostate. *J Magn Reson Imaging* 6, 603–607.



- 2311 Liney, G.P., Lowry, M., Turnbull, L.W., Manton, D.J., Knowles, A.J., Blackband,  
2312 S.J., Horsman, A., 1996b. Proton MR T2 maps correlate with the citrate concen-  
2313 tration in the prostate. *NMR Biomed* 9, 59–64.
- 2314 Liney, G.P., Turnbull, L.W., Lowry, M., Turnbull, L.S., Knowles, A.J., Horsman, A.,  
2315 1997. In vivo quantification of citrate concentration and water T2 relaxation time  
2316 of the pathologic prostate gland using  $^1\text{H}$  MRS and MRI. *Magn Reson Imaging*  
2317 15, 1177–1186.
- 2318 Litjens, G., Debats, O., van de Ven, W., Karssemeijer, N., Huisman, H., 2012a. A  
2319 pattern recognition approach to zonal segmentation of the prostate on MRI. *Med*  
2320 *Image Comput Comput Assist Interv* 15, 413–420.
- 2321 Litjens, G.J.S., Barentsz, J.O., Karssemeijer, N., Huisman, H.J., 2012b. Automated  
2322 computer-aided detection of prostate cancer in MR images: from a whole-organ to  
2323 a zone-based approach, in: *Proc. SPIE 8315, Medical Imaging 2012: Computer-*  
2324 *Aided Diagnosis*, pp. 83150G–83150G–6.
- 2325 Litjens, G.J.S., Vos, P.C., Barentsz, J.O., Karssemeijer, N., Huisman, H.J., 2011.  
2326 Automatic computer aided detection of abnormalities in multi-parametric prostate  
2327 MRI, in: *Proc. SPIE 7963, Medical Imaging 2011: Computer-Aided Diagnosis*, pp.  
2328 79630T–79630T–7.
- 2329 Liu, P., Wang, S., Turkbey, B., Grant, K. and Pinto, P.C.P., Wood, B.J., Summers,  
2330 R.M., 2013. A prostate cancer computer-aided diagnosis system using multimodal  
2331 magnetic resonance imaging and targeted biopsy labels, in: *Proc. SPIE 8670,*  
2332 *Medical Imaging 2013: Computer-Aided Diagnosis*, pp. 86701G–86701G–6.
- 2333 Liu, W., Turkbey, B., Senegas, J., Remmele, S., Xu, S., Kruecker, J., Bernardo,  
2334 M., Wood, B.J., Pinto, P.A., Choyke, P.L., 2011. Accelerated T2 mapping for  
2335 characterization of prostate cancer. *Magn Reson Med* 65, 1400–1406.
- 2336 Liu, X., Langer, D.L., Haider, M.A., Yang, Y., Wernick, M.N., Yetik, I.S., 2009.  
2337 Prostate cancer segmentation with simultaneous estimation of Markov random  
2338 field parameters and class. *IEEE Trans Med Imaging* 28, 906–915.
- 2339 Lopes, R., Ayache, A., Makni, N., Puech, P., Villers, A., Mordon, S., Betrouni, N.,  
2340 2011. Prostate cancer characterization on MR images using fractal features. *Med*  
2341 *Phys* 38, 83–95.

- 2342 Lu-Yao, G.L., Albertsen, P.C., Moore, D.F., Shih, W., Lin, Y., DiPaola, R.S., Barry,  
2343 M.J., Zietman, A., O’Leary, M., Walker-Corkery, E., Yao, S.L., 2009. Outcomes of  
2344 localized prostate cancer following conservative management. *JAMA* 302, 1202–  
2345 1209.
- 2346 Lv, D., Guo, X., Wang, X., Zhang, J., Fang, J., 2009. Computerized characterization  
2347 of prostate cancer by fractal analysis in MR images. *J Magn Reson Imaging* 30,  
2348 161–168.
- 2349 Ma, R.W., Chapman, K., 2009. A systematic review of the effect of diet in prostate  
2350 cancer prevention and treatment. *J Hum Nutr Diet* 22, 187–199.
- 2351 Madabhushi, A., Udupa, J., Souza, A., 2006. Generalized scale: Theory, algorithms,  
2352 and application to image inhomogeneity correction . *Computer Vision and Image*  
2353 *Understanding* 101, 100 – 121.
- 2354 Madabhushi, A., Udupa, J.K., 2006. New methods of MR image intensity standard-  
2355 ization via generalized scale. *Med Phys* 33, 3426–3434.
- 2356 Maintz, J.B., Viergever, M.A., 1998. A survey of medical image registration. *Med*  
2357 *Image Anal* 2, 1–36.
- 2358 Mallat, S., 2008. A wavelet tour of signal processing, Third Edition: The sparse way.  
2359 3rd ed., Academic Press.
- 2360 Manjon, J.V., Carbonell-Caballero, J., Lull, J.J., Garcia-Marti, G., Marti-Bonmati,  
2361 L., Robles, M., 2008. MRI denoising using non-local means. *Med Image Anal* 12,  
2362 514–523.
- 2363 Matulewicz, L., Jansen, J.F., Bokacheva, L., Vargas, H.A., Akin, O., Fine, S.W.,  
2364 Shukla-Dave, A., Eastham, J.A., Hricak, H., Koutcher, J.A., Zakian, K.L., 2013.  
2365 Anatomic segmentation improves prostate cancer detection with artificial neural  
2366 networks analysis of 1H magnetic resonance spectroscopic imaging. *Journal of*  
2367 *Magnetic Resonance Imaging* , n/a–n/a.
- 2368 Mazzetti, S., De Luca, M., Bracco, C., Vignati, A., Giannini, V., Stasi, M., Russo,  
2369 F., Armando, E., Agliozzo, S., Regge, D., 2011. A CAD system based on multi-  
2370 parametric analysis for cancer prostate detection on DCE-MRI, in: *Proc. SPIE*  
2371 7963, *Medical Imaging 2011: Computer-Aided Diagnosis*, pp. 79633Q–79633Q–7.
- 2372 McNeal, J.E., 1981. The zonal anatomy of the prostate. *Prostate* 2, 35–49.

- 2373 McNeal, J.E., Redwine, E.A., Freiha, F.S., Stamey, T.A., 1988. Zonal distribution  
2374 of prostatic adenocarcinoma. Correlation with histologic pattern and direction of  
2375 spread. *Am. J. Surg. Pathol.* 12, 897–906.
- 2376 Middleton, D., Esposito, R., 1968. Simultaneous optimum detection and estimation  
2377 of signals in noise. *Information Theory, IEEE Transactions on* 14, 434–444.
- 2378 Mitra, J., 2012. Multimodal image registration applied to magnetic resonance and  
2379 ultrasound prostatic images. Ph.D. thesis. Universitat de Girona and Université  
2380 de Bourgogne.
- 2381 Mitra, J., Kato, Z., Marti, R., Oliver, A., Llado, X., Sidibe, D., Ghose, S., Vilanova,  
2382 J.C., Comet, J., Meriaudeau, F., 2012. A spline-based non-linear diffeomorphism  
2383 for multimodal prostate registration. *Med Image Anal* 16, 1259–1279.
- 2384 Mitra, J., Marti, R., Oliver, A., Llado, X., Vilanova, J.C., Meriaudeau, F., 2011.  
2385 A comparison of thin-plate splines with automatic correspondences and B-splines  
2386 with uniform grids for multimodal prostate registration, in: *Society of Photo-  
2387 Optical Instrumentation Engineers (SPIE) Conference Series*.
- 2388 Mohan, J., Krishnaveni, V., Guo, Y., 2014. A survey on the magnetic resonance  
2389 image denoising methods. *Biomedical Signal Processing and Control* 9, 56 – 69.
- 2390 Moore, C.M., Ridout, A., Emberton, M., 2013. The role of MRI in active surveillance  
2391 of prostate cancer. *Curr Opin Urol* 23, 261–267.
- 2392 Morgan, R., Boxall, A., Bhatt, A., Bailey, M., Hindley, R., Langley, S., Whitaker,  
2393 H.C., Neal, D.E., Ismail, M., Whitaker, H., Annels, N., Michael, A., Pandha,  
2394 H., 2011. Engrailed-2 (EN2): a tumor specific urinary biomarker for the early  
2395 diagnosis of prostate cancer. *Clin. Cancer Res.* 17, 1090–1098.
- 2396 Nelder, J.A., Mead, R., 1965. A simplex method for function minimization. *The  
2397 Computer Journal* 7, 308–313.
- 2398 Niaf, E., Rouviere, O., Mege-Lechevallier, F., Bratan, F., Lartizien, C., 2012.  
2399 Computer-aided diagnosis of prostate cancer in the peripheral zone using mul-  
2400 tiparametric MRI. *Phys Med Biol* 57, 3833–3851.
- 2401 Niaf, E., Rouvire, O., Lartizien, C., 2011. Computer-aided diagnosis for prostate  
2402 cancer detection in the peripheral zone via multisequence MRI, in: *Proc. SPIE  
2403 7963, Medical Imaging 2011: Computer-Aided Diagnosis*.

- 2404 van Niekerk, C.G., van der Laak, J.A., Borger, M.E., Huisman, H.J., Witjes, J.A.,  
2405 Barentsz, J.O., Hulsbergen-van de Kaa, C.A., 2009. Computerized whole slide  
2406 quantification shows increased microvascular density in pT2 prostate cancer as  
2407 compared to normal prostate tissue. *Prostate* 69, 62–69.
- 2408 van Niekerk, C.G., Witjes, J.A., Barentsz, J.O., van der Laak, J.A., Hulsbergen-  
2409 van de Kaa, C.A., 2013. Microvascularity in transition zone prostate tumors re-  
2410 sembles normal prostatic tissue. *Prostate* 73, 467–475.
- 2411 Noguchi, M., Stamey, T.A., McNeal, J.E., Yemoto, C.M., 2001. Relationship between  
2412 systematic biopsies and histological features of 222 radical prostatectomy speci-  
2413 mens: lack of prediction of tumor significance for men with nonpalpable prostate  
2414 cancer. *J. Urol.* 166, 104–109.
- 2415 Nowak, R., 1999. Wavelet-based Rician noise removal for magnetic resonance imag-  
2416 ing. *Image Processing, IEEE Transactions on* 8, 1408–1419.
- 2417 Nyul, L.G., Udupa, J.K., 1999. On standardizing the MR image intensity scale.  
2418 *Magn Reson Med* 42, 1072–1081.
- 2419 Nyul, L.G., Udupa, J.K., Zhang, X., 2000. New variants of a method of MRI scale  
2420 standardization. *IEEE Trans Med Imaging* 19, 143–150.
- 2421 Ojala, T., Pietikäinen, M., Harwood, D., 1996. A comparative study of texture  
2422 measures with classification based on featured distributions. *Pattern Recognition*  
2423 29, 51–59.
- 2424 Osorio-Garcia, M., Croitor Sava, A., Sima, D.M., Nielsen, F., Himmelreich, U.,  
2425 Van Huffel, S., 2012. Magnetic Resonance Spectroscopy. InTech. chapter Quan-  
2426 tification improvements of 1H MRS Signals. pp. 1–27.
- 2427 Oster, G., Lamerato, L., Glass, A.G., Richert-Boe, K.E., Lopez, A., Chung, K.,  
2428 Richhariya, A., Dodge, T., Wolff, G.G., Balakumaran, A., Edelsberg, J., 2013.  
2429 Natural history of skeletal-related events in patients with breast, lung, or prostate  
2430 cancer and metastases to bone: a 15-year study in two large US health systems.  
2431 *Support Care Cancer* 21, 3279–3286.
- 2432 Ozer, S., Haider, M., Langer, D.L., Van der Kwast, T.H., Evans, A., Wernick, M.,  
2433 Trachtenberg, J., Yetik, I., 2009. Prostate cancer localization with multispectral  
2434 MRI based on Relevance Vector Machines, in: *Biomedical Imaging: From Nano*  
2435 *to Macro*, 2009. ISBI '09. IEEE International Symposium on, pp. 73–76.

- 2436 Ozer, S., Langer, D.L., Liu, X., Haider, M.A., van der Kwast, T.H., Evans, A.J.,  
2437 Yang, Y., Wernick, M.N., Yetik, I.S., 2010. Supervised and unsupervised methods  
2438 for prostate cancer segmentation with multispectral MRI. *Med Phys* 37, 1873–  
2439 1883.
- 2440 Padhani, A.R., 2002. Dynamic contrast-enhanced MRI in clinical oncology: current  
2441 status and future directions. *J Magn Reson Imaging* 16, 407–422.
- 2442 Padhani, A.R., 2011. Integrating multiparametric prostate MRI into clinical practice.  
2443 *Cancer Imaging* 11 Spec No A, 27–37.
- 2444 Parfait, S., 2010. Classification de spectres et recherche de biomarqueurs en spec-  
2445 troscopie par résonance magnétique nucléaire du proton dans les tumeurs prosta-  
2446 tiques. Ph.D. thesis. Université de Bourgogne.
- 2447 Parfait, S., Walker, P., Crhange, G., Tizon, X., Mitran, J., 2012. Classification of  
2448 prostate magnetic resonance spectra using Support Vector Machine . *Biomedical*  
2449 *Signal Processing and Control* 7, 499 – 508.
- 2450 Pearson, K., 1901. On lines and planes of closest fit to systems of points in space.  
2451 *Philosophical Magazine* 2, 559–572.
- 2452 Peng, H., Long, F., Ding, C., 2005. Feature selection based on mutual information  
2453 criteria of max-dependency, max-relevance, and min-redundancy. *Pattern Analysis*  
2454 *and Machine Intelligence, IEEE Transactions on* 27, 1226–1238.
- 2455 Peng, Y., Jiang, Y., Yang, C., Brown, J., Antic, T., Sethi, I., Schmid-Tannwald, C.,  
2456 Giger, M., Eggener, S., Oto, A., 2013. Quantitative analysis of multiparametric  
2457 prostate MR images: differentiation between prostate cancer and normal tissue  
2458 and correlation with Gleason score—a computer-aided diagnosis development study.  
2459 *Radiology* 267, 787–796.
- 2460 Petrick, N., Haider, M., Summers, R.M., Yeshwant, S.C., Brown, L., Iuliano, E.M.,  
2461 Louie, A., Choi, J.R., Pickhardt, P.J., 2008. CT colonography with computer-  
2462 aided detection as a second reader: observer performance study. *Radiology* 246,  
2463 148–156.
- 2464 Pijnappel, W., van den Boogaart, A., de Beer, R., van Ormondt, D., 1992. SVD-  
2465 based quantification of magnetic resonance signals . *Journal of Magnetic Resonance*  
2466 (1969) 97, 122 – 134.

- 2467 Pizurica, A., 2002. Image denoising using wavelets and spatial context modeling.  
2468 Ph.D. thesis. Universiteit Gent.
- 2469 Pizurica, A., Philips, W., Lemahieu, I., Acheroy, M., 2003. A versatile wavelet  
2470 domain noise filtration technique for medical imaging. *IEEE Trans Med Imaging*  
2471 22, 323–331.
- 2472 Pluim, J., Maintz, J., Viergever, M., 2003. Mutual-information-based registration of  
2473 medical images: a survey. *IEEE Transactions on Medical Imaging* 22, 986–1004.
- 2474 Prewitt, J., 1970. Picture processing and psychohistories. Academic Press. chapter  
2475 Object enhancement and extraction.
- 2476 Provencher, S.W., 1993. Estimation of metabolite concentrations from localized in  
2477 vivo proton NMR spectra. *Magn Reson Med* 30, 672–679.
- 2478 Puech, P., Betrouni, N., Makni, N., Dewalle, A.S., Villers, A., Lemaitre, L., 2009.  
2479 Computer-assisted diagnosis of prostate cancer using DCE-MRI data: design, im-  
2480 plementation and preliminary results. *Int J Comput Assist Radiol Surg* 4, 1–10.
- 2481 Quinlan, J., 1986. Induction of decision trees. *Machine Learning* 1, 81–106.
- 2482 Quinlan, J., 1993. C4.5: Programs for machine learning. Morgan Kaufmann Pub-  
2483 lishers Inc., San Francisco, CA, USA.
- 2484 Quinonero-Candela, J., Girard, A., Rasmussen, C., 2002. Prediction at an Uncer-  
2485 tain Input for Gaussian processes and relevance vector machines application to  
2486 Multiple-Step ahead time-series forecasting. Technical Report. DTU Informatics.
- 2487 Quint, L.E., Van Erp, J.S., Bland, P.H., Mandell, S.H., Del Buono, E.A., Grossman,  
2488 H.B., Glazer, G.M., Gikas, P.W., 1991. Carcinoma of the prostate: MR images  
2489 obtained with body coils do not accurately reflect tumor volume. *AJR Am J*  
2490 *Roentgenol* 156, 511–516.
- 2491 Rangayyan, R., Ayres, F., Desautels, J., 2007. A review of computer-aided diagnosis  
2492 of breast cancer: Toward the detection of subtle signs. *Journal of the Franklin*  
2493 *Institute* 344, 312 – 348.
- 2494 Rasmussen, C., Williams, C., 2005. Gaussian processes for machine learning. The  
2495 MIT Press.

2496 Ratiney, H., Sdika, M., Coenradie, Y., Cavassila, S., van Ormondt, D., Graveron-  
2497 Demilly, D., 2005. Time-domain semi-parametric estimation based on a metabolite  
2498 basis set. *NMR Biomed* 18, 1–13.

2499 Rish, I., 2001. An empirical study of the naive Bayes classifier, in: *IJCAI 2001*  
2500 *workshop on empirical methods in artificial intelligence*, pp. 41–46.

2501 Rodriguez, C., Freedland, S.J., Deka, A., Jacobs, E.J., McCullough, M.L., Patel,  
2502 A.V., Thun, M.J., Calle, E.E., 2007. Body mass index, weight change, and risk  
2503 of prostate cancer in the Cancer Prevention Study II Nutrition Cohort. *Cancer*  
2504 *Epidemiol. Biomarkers Prev.* 16, 63–69.

2505 Rosenkrantz, A.B., Sabach, A., Babb, J.S., Matza, B.W., Taneja, S.S., Deng, F.M.,  
2506 2013. Prostate cancer: comparison of dynamic contrast-enhanced MRI techniques  
2507 for localization of peripheral zone tumor. *AJR Am J Roentgenol* 201, W471–478.

2508 Roweis, S.T., Saul, L.K., 2000. Nonlinear dimensionality reduction by locally linear  
2509 embedding. *Science* 290, 2323–2326.

2510 Rueckert, D., Sonoda, L.I., Hayes, C., Hill, D.L., Leach, M.O., Hawkes, D.J., 1999.  
2511 Nonrigid registration using free-form deformations: application to breast MR im-  
2512 ages. *IEEE Trans Med Imaging* 18, 712–721.

2513 Rumelhart, D.E., Hinton, G.E., Williams, R.J., 1988. Learning internal represen-  
2514 tations by error propagation, in: Anderson, J.A., Rosenfeld, E. (Eds.), *Neuro-*  
2515 *computing: foundations of research*. MIT Press, Cambridge, MA, USA. chapter  
2516 *Learning Internal Representations by Error Propagation*, pp. 673–695.

2517 Saeys, Y., Inza, I., Larranaga, P., 2007. A review of feature selection techniques in  
2518 bioinformatics. *Bioinformatics* 23, 2507–2517.

2519 Scheidler, J., Hricak, H., Vigneron, D.B., Yu, K.K., Sokolov, D.L., Huang, L.R.,  
2520 Zaloudek, C.J., Nelson, S.J., Carroll, P.R., Kurhanewicz, J., 1999a. Prostate  
2521 cancer: localization with three-dimensional proton MR spectroscopic imaging–  
2522 clinicopathologic study. *Radiology* 213, 473–480.

2523 Scheidler, J., Petsch, R., Muller-Lisse, U., Heuck, A., Reiser, M., 1999b. Echo-planar  
2524 diffusion-weighted MR imaging of the prostate, in: *Proceedings of the 7th Annual*  
2525 *Meeting of ISMRM Philadelphia*, p. 1103.

- 2526 Schlemmer, H.P., Merkle, J., Grobholz, R., Jaeger, T., Michel, M.S., Werner, A.,  
2527 Rabe, J., van Kaick, G., 2004. Can pre-operative contrast-enhanced dynamic MR  
2528 imaging for prostate cancer predict microvessel density in prostatectomy speci-  
2529 mens? *Eur Radiol* 14, 309–317.
- 2530 Schroder, F.H., Carter, H.B., Wolters, T., van den Bergh, R.C., Gosselaar, C.,  
2531 Bangma, C.H., Roobol, M.J., 2008. Early detection of prostate cancer in 2007.  
2532 Part 1: PSA and PSA kinetics. *Eur. Urol.* 53, 468–477.
- 2533 Schröder, F.H., Hugosson, J., Roobol, M.J., Tammela, T.L., Ciatto, S., Nelen, V.,  
2534 Kwiatkowski, M., Lujan, M., Lilja, H., Zappa, M., Denis, L.J., Recker, F., Pez,  
2535 A., Määttänen, L., Bangma, C.H., Aus, G., Carlsson, S., Villers, A., Rebillard,  
2536 X., van der Kwast, T., Kujala, P.M., Blijenberg, B.G., Stenman, U.H., Huber, A.,  
2537 Taari, K., Hakama, M., Moss, S.M., de Koning, H.J., Auvinen, A., 2012. Prostate-  
2538 cancer mortality at 11 years of follow-up. *New England Journal of Medicine* 366,  
2539 981–990.
- 2540 Shapiro, L.G., Stockman, G.C., 2001. *Computer vision*. Prentice Hall, Upper Saddle  
2541 River, NJ.
- 2542 Shi, J., Malik, J., 2000. Normalized cuts and image segmentation. *Pattern Analysis*  
2543 *and Machine Intelligence, IEEE Transactions on* 22, 888–905.
- 2544 Shimofusa, R., Fujimoto, H., Akamata, H., Motoori, K., Yamamoto, S., Ueda, T.,  
2545 Ito, H., 2005. Diffusion-weighted imaging of prostate cancer. *J Comput Assist*  
2546 *Tomogr* 29, 149–153.
- 2547 Siegel, R., Naishadham, D., Jemal, A., 2013. Cancer statistics, 2013. *CA Cancer J*  
2548 *Clin* 63, 11–30.
- 2549 Sled, J.G., Zijdenbos, A.P., Evans, A.C., 1998. A nonparametric method for auto-  
2550 matic correction of intensity nonuniformity in MRI data. *IEEE Trans Med Imaging*  
2551 17, 87–97.
- 2552 Sobel, I., 1970. *Camera models and machine perception*. Technical Report. DTIC  
2553 Document.
- 2554 Somford, D.M., Futterer, J.J., Hambrock, T., Barentsz, J.O., 2008. Diffusion and  
2555 perfusion MR imaging of the prostate. *Magn Reson Imaging Clin N Am* 16, 685–  
2556 695.



2557 Specht, D.F., 1988. Probabilistic neural networks for classification, mapping, or  
2558 associative memory, in: Neural Networks, 1988., IEEE International Conference  
2559 on, pp. 525–532 vol.1.

2560 St Lawrence, K.S., Lee, T.Y., 1998. An adiabatic approximation to the tissue homo-  
2561 geneity model for water exchange in the brain: I. Theoretical derivation. *J. Cereb.*  
2562 *Blood Flow Metab.* 18, 1365–1377.

2563 Stamey, T.A., Donaldson, A.N., Yemoto, C.E., McNeal, J.E., Sozen, S., Gill,  
2564 H., 1998. Histological and clinical findings in 896 consecutive prostates treated  
2565 only with radical retropubic prostatectomy: epidemiologic significance of annual  
2566 changes. *J. Urol.* 160, 2412–2417.

2567 Staring, M., van der Heide, U.A., Klein, S., Viergever, M.A., Pluim, J.P., 2009.  
2568 Registration of cervical MRI using multifeature mutual information. *IEEE Trans*  
2569 *Med Imaging* 28, 1412–1421.

2570 Steinberg, G.D., Carter, B.S., Beaty, T.H., Childs, B., Walsh, P.C., 1990. Family  
2571 history and the risk of prostate cancer. *Prostate* 17, 337–347.

2572 Strum, S., Pogliano, D., 2005. What every doctor who treats male patients should  
2573 know. *PCRI Insights* vol. 8, no. 2.

2574 Styner, M., Brechbuhler, C., Szckely, G., Gerig, G., 2000. Parametric estimate of  
2575 intensity inhomogeneities applied to MRI. *Medical Imaging, IEEE Transactions*  
2576 *on* 19, 153–165.

2577 Styner, M., Gerig, G., 1997. Evaluation of 2D/3D bias correction with 1+1ES-  
2578 optimization. Technical Report. ETH Zürich.

2579 Sung, Y.S., Kwon, H.J., Park, B.W., Cho, G., Lee, C.K., Cho, K.S., Kim, J.K.,  
2580 2011. Prostate cancer detection on dynamic contrast-enhanced MRI: computer-  
2581 aided diagnosis versus single perfusion parameter maps. *AJR Am J Roentgenol*  
2582 197, 1122–1129.

2583 Suzuki, K., 2012. A review of computer-aided diagnosis in thoracic and colonic  
2584 imaging. *Quant Imaging Med Surg* 2, 163–176.

2585 Swanson, M.G., Vigneron, D.B., Tran, T.K., Sailasuta, N., Hurd, R.E., Kurhanewicz,  
2586 J., 2001. Single-voxel oversampled J-resolved spectroscopy of in vivo human  
2587 prostate tissue. *Magn Reson Med* 45, 973–980.

2588 Taira, A.V., Merrick, G.S., Galbreath, R.W., Andreini, H., Taubenslag, W., Curtis,  
2589 R., Butler, W.M., Adamovich, E., Wallner, K.E., 2010. Performance of transper-  
2590 ineal template-guided mapping biopsy in detecting prostate cancer in the initial  
2591 and repeat biopsy setting. *Prostate Cancer Prostatic Dis.* 13, 71–77.

2592 Tipping, M., 2001. Sparse Bayesian learning and the relevance vector machine.  
2593 *Journal of Machine Learning Research* 1, 211–244.

2594 Tiwari, P., Kurhanewicz, J., Madabhushi, A., 2013. Multi-kernel graph embedding  
2595 for detection, Gleason grading of prostate cancer via MRI/MRS. *Med Image Anal*  
2596 17, 219–235.

2597 Tiwari, P., Kurhanewicz, J., Rosen, M., Madabhushi, A., 2010. Semi supervised  
2598 multi kernel (SeSMiK) graph embedding: identifying aggressive prostate cancer  
2599 via magnetic resonance imaging and spectroscopy. *Med Image Comput Comput*  
2600 *Assist Interv* 13, 666–673.

2601 Tiwari, P., Madabhushi, A., Rosen, M., 2007. A hierarchical unsupervised spec-  
2602 tral clustering scheme for detection of prostate cancer from magnetic resonance  
2603 spectroscopy (MRS). *Med Image Comput Comput Assist Interv* 10, 278–286.

2604 Tiwari, P., Rosen, M., Madabhushi, A., 2008. Consensus-locally linear embedding  
2605 (C-LLE): application to prostate cancer detection on magnetic resonance spec-  
2606 troscopy. *Med Image Comput Comput Assist Interv* 11, 330–338.

2607 Tiwari, P., Rosen, M., Madabhushi, A., 2009a. A hierarchical spectral clustering and  
2608 nonlinear dimensionality reduction scheme for detection of prostate cancer from  
2609 magnetic resonance spectroscopy (MRS). *Med Phys* 36, 3927–3939.

2610 Tiwari, P., Rosen, M., Reed, G., Kurhanewicz, J., Madabhushi, A., 2009b. Spectral  
2611 embedding based probabilistic boosting tree (ScEPTre): classifying high dimen-  
2612 sional heterogeneous biomedical data. *Med Image Comput Comput Assist Interv*  
2613 12, 844–851.

2614 Tiwari, P., Viswanath, S., Kurhanewicz, J., Sridhar, A., Madabhushi, A., 2012.  
2615 Multimodal wavelet embedding representation for data combination (MaWERiC):  
2616 integrating magnetic resonance imaging and spectroscopy for prostate cancer de-  
2617 tection. *NMR Biomed* 25, 607–619.

2618 Tofts, P., 2010. T1-weighted DCE imaging concepts: modelling, acquisition and  
2619 analysis, in: *Magneton Flash*. Siemens.

2620 Tofts, P.S., 1997. Modeling tracer kinetics in dynamic Gd-DTPA MR imaging. J  
2621 Magn Reson Imaging 7, 91–101.

2622 Toth, R., Chappelow, J., Rosen, M., Pungavkar, S., Kalyanpur, A., Madabhushi, A.,  
2623 2008. Multi-attribute non-initializing texture reconstruction based active shape  
2624 model (MANTRA). Med Image Comput Comput Assist Interv 11, 653–661.

2625 Toth, R., Doyle, S., Pungavkar, S., Kalyanpur, A., Madabhushi, A., 2009. A boosted  
2626 ensemble scheme for accurate landmark detection for active shape models, in: SPIE  
2627 Medical Imaging, Orlando, FL.

2628 Tu, Z., 2005. Probabilistic boosting-tree: learning discriminative models for classifi-  
2629 cation, recognition, and clustering, in: Computer Vision, 2005. ICCV 2005. Tenth  
2630 IEEE International Conference on, pp. 1589–1596 Vol. 2.

2631 Turkbey, B., Choyke, P.L., 2012. Multiparametric MRI and prostate cancer diagnosis  
2632 and risk stratification. Curr Opin Urol 22, 310–315.

2633 Vanhamme, L., van den Boogaart, A., Van Huffel, S., 1997. Improved method for  
2634 accurate and efficient quantification of MRS data with use of prior knowledge. J.  
2635 Magn. Reson. 129, 35–45.

2636 Vapnik, V., Lerner, A., 1963. Pattern Recognition using Generalized Portrait  
2637 Method. Automation and Remote Control 24.

2638 Verma, S., Turkbey, B., Muradyan, N., Rajesh, A., Cornud, F., Haider, M.A.,  
2639 Choyke, P.L., Harisinghani, M., 2012. Overview of dynamic contrast-enhanced  
2640 MRI in prostate cancer diagnosis and management. AJR Am J Roentgenol 198,  
2641 1277–1288.

2642 Vilanova, J.C., Comet, J., Barceló-Vidal, C., Barceló, J., López-Bonet, E., Maroto,  
2643 A., Arzoz, M., Moreno, À., Areal, J., 2009. Peripheral zone prostate cancer in  
2644 patients with elevated PSA levels and low free-to-total PSA ratio: detection with  
2645 MR imaging and MR spectroscopy. Radiology 253, 135–143.

2646 Villers, A., Steg, A., Boccon-Gibod, L., 1991. Anatomy of the prostate: review of  
2647 the different models. Eur. Urol. 20, 261–268.

2648 Viola, P., Wells, III, W.M., 1997. Alignment by maximization of mutual information.  
2649 Int. J. Comput. Vision 24, 137–154.

2650 Viswanath, S., Bloch, B.N., Chappelow, J., Patel, P., Rofsky, N., Lenkinski, R.,  
2651 Genega, E., Madabhushi, A., 2011. Enhanced multi-protocol analysis via intel-  
2652 ligent supervised embedding (EMPrAvISE): detecting prostate cancer on multi-  
2653 parametric MRI, in: Proc. SPIE 7963, Medical Imaging 2011: Computer-Aided  
2654 Diagnosis.

2655 Viswanath, S., Bloch, B.N., Genega, E., Rofsky, N., Lenkinski, R., Chappelow, J.,  
2656 Toth, R., Madabhushi, A., 2008a. A comprehensive segmentation, registration,  
2657 and cancer detection scheme on 3 Tesla in vivo prostate DCE-MRI. Med Image  
2658 Comput Comput Assist Interv 11, 662–669.

2659 Viswanath, S., Bloch, B.N., Rosen, M., Chappelow, J., Toth, R., Rofsky, N., Lenk-  
2660 inski, R., Genega, E., Kalyanpur, A., Madabhushi, A., 2009. Integrating struc-  
2661 tural and functional imaging for computer assisted detection of prostate cancer on  
2662 multi-protocol in vivo 3 Tesla MRI, in: Society of Photo-Optical Instrumentation  
2663 Engineers (SPIE) Conference Series.

2664 Viswanath, S., Tiwari, P., Rosen, M., Madabhushi, A., 2008b. A meta-classifier for  
2665 detecting prostate cancer by quantitative integration of *In Vivo* magnetic reso-  
2666 nance spectroscopy and magnetic resonance imaging, in: Medical Imaging 2008:  
2667 Computer-Aided Diagnosis, SPIE.

2668 Viswanath, S.E., Bloch, N.B., Chappelow, J.C., Toth, R., Rofsky, N.M., Genega,  
2669 E.M., Lenkinski, R.E., Madabhushi, A., 2012. Central gland and peripheral zone  
2670 prostate tumors have significantly different quantitative imaging signatures on 3  
2671 Tesla endorectal, in vivo T2-weighted MR imagery. J Magn Reson Imaging 36,  
2672 213–224.

2673 Vos, P.C., Barentsz, J.O., Karssemeijer, N., Huisman, H.J., 2012. Automatic  
2674 computer-aided detection of prostate cancer based on multiparametric magnetic  
2675 resonance image analysis. Phys Med Biol 57, 1527–1542.

2676 Vos, P.C., Hambrock, T., Barentsz, J.O., Huisman, H.J., 2008a. Combining T2-  
2677 weighted with dynamic MR images for computerized classification of prostate le-  
2678 sions, in: Medical Imaging 2008: Computer-Aided Diagnosis, SPIE.

2679 Vos, P.C., Hambrock, T., Barentsz, J.O., Huisman, H.J., 2010. Computer-assisted  
2680 analysis of peripheral zone prostate lesions using T2-weighted and dynamic con-  
2681 trast enhanced T1-weighted MRI. Phys Med Biol 55, 1719–1734.

2682 Vos, P.C., Hambrock, T., Hulsbergen-van de Kaa, C.A., Futterer, J.J., Barentsz,  
2683 J.O., Huisman, H.J., 2008b. Computerized analysis of prostate lesions in the  
2684 peripheral zone using dynamic contrast enhanced MRI. *Med Phys* 35, 888–899.

2685 Vovk, U., Pernus, F., Likar, B., 2007. A review of methods for correction of intensity  
2686 inhomogeneity in MRI. *Medical Imaging, IEEE Transactions on* 26, 405–421.

2687 Walker, P., Crehange, G., Parfait, S., Cochet, A., Maignon, P., Cormier, L.,  
2688 Brunotte, F., 2010. Absolute quantification in 1H MRSI of the prostate at 3T, in:  
2689 ISMRM Annual Meeting 2010.

2690 Wang, L., Mazaheri, Y., Zhang, J., Ishill, N.M., Kuroiwa, K., Hricak, H., 2008.  
2691 Assessment of biologic aggressiveness of prostate cancer: correlation of MR signal  
2692 intensity with Gleason grade after radical prostatectomy. *Radiology* 246, 168–176.

2693 Warfield, S.K., Zou, K.H., Wells, W.M., 2004. Simultaneous truth and performance  
2694 level estimation (STAPLE): an algorithm for the validation of image segmentation.  
2695 *IEEE Trans Med Imaging* 23, 903–921.

2696 Wiart, M., Curiel, L., Gelet, A., Lyonnet, D., Chapelon, J.Y., Rouviere, O., 2007.  
2697 Influence of perfusion on high-intensity focused ultrasound prostate ablation: a  
2698 first-pass MRI study. *Magn Reson Med* 58, 119–127.

2699 Ye, L., Kynaston, H.G., Jiang, W.G., 2007. Bone metastasis in prostate cancer:  
2700 molecular and cellular mechanisms (Review). *Int. J. Mol. Med.* 20, 103–111.

2701 Zelhof, B., Lowry, M., Rodrigues, G., Kraus, S., Turnbull, L., 2009. Description  
2702 of magnetic resonance imaging-derived enhancement variables in pathologically  
2703 confirmed prostate cancer and normal peripheral zone regions. *BJU Int.* 104, 621–  
2704 627.

2705 Zhao, G., Ahonen, T., Matas, J., Pietikainen, M., 2012. Rotation-Invariant Image  
2706 and Video Description With Local Binary Pattern Features. *Image Processing,*  
2707 *IEEE Transactions on* 21, 1465–1477.

2708 Zhu, H., Ouwerkerk, R., Barker, P.B., 2010. Dual-band water and lipid suppression  
2709 for MR spectroscopic imaging at 3 Tesla. *Magn Reson Med* 63, 1486–1492.

2710 Zitová, B., Flusser, J., 2003. Image registration methods: a survey. *Image and*  
2711 *Vision Computing* 21, 977 – 1000.